NTNU – Trondheim
Norwegian University of
Science and Technology

Structural Reliability Analysis of the Hardanger Bridge using an enhanced Monte Carlo Method

Georg Alexander Bugge

Civil and Environmental Engineering
Submission date: June 2014
Supervisor: Ole Andre Øiseth, KT

Norwegian University of Science and Technology
Department of Structural Engineering

Institutt for konstruksjonsteknikk

FAKULTET FOR INGENIØRVITENSKAP OG TEKNOLOGI
NTNU – Norges teknisk-naturvitenskapelige universitet

MASTEROPPGAVE 2014

for

Georg Alexander Bugge

Vurdering av flutterstabilitetsgrensen til Hardangerbrua ved hjelp av en probabilistisk metode

Assessment of the flutter stability limit of the Hardanger Bridge using a probabilistic approach

Aeroelastisk stabilitet er ett av de mest sentrale designkriteriene for slanke brukonstruksjoner. Kravene som stilles til brukonstruksjoner i Norge er gitt i Statens vegvesens håndbok 185. Brukonstruksjoner i vindklasse III skal kontrolleres i ulykkesgrensetilstanden for et vindfelt med returperiode på 500 år. Det kreves videre at den kritiske hastigheten skal være 1.6 ganger større enn ti minutters middelvind med en forventet returperiode på 500 år. Disse kravene skal sørge for at sannsynligheten for sammenbrudd blir tilstrekkelig liten.

Denne oppgaven dreier seg om beregning av sannsynligheten for flutterinstabilitet for Hardangerbrua.

Oppgaven bør inneholde følgende temaer:

- Grunnleggende teori for beregning av sviktsannsynlighet
- Grundig diskusjon av alle usikkerheter knyttet til beregninger av kritisk hastighet
- Hvordan Monte Carlo simuleringer kan benyttes til å beregne sviktsannsynlighet
- Modellering av aerodynamisk deriverte som stokastiske variabler
- Estimering av sviktsannsynlighet

Det legges vekt på at studenten må gjøre fornuftige forenklinger for å komme i mål med oppgaven

Besvarelsen organiseres i henhold til gjeldende retningslinjer.

Veileder(e): Ole Andre Øiseth, Anders Rönnquist

Besvarelsen skal leveres til Institutt for konstruksjonsteknikk innen 10. juni 2014.

NTNU, 28. januar, 2014

Ole Andre Øiseth
faglærer

Preface

This master thesis concludes a civil engineering Master's degree study at the Norwegian University of Science and Technology (NTNU). It has been carried out during the spring semester of 2014, at the Department of Structural Engineering. The supervisors have been Ole Øiseth and Anders Rønnquist.

The study presents a flutter reliability analysis of the Hardanger Bridge. The multi-mode flutter limit has been determined using a probabilistic approach, and then the limit has been compared to the extreme mean wind value expected to occur at construction site. Due to the low probabilities involved in the reliability analysis, an enhanced Monte Carlo method developed at NTNU has been employed.

Since I first saw a video of the Tacoma Narrow Bridge failure, I have been fascinated by the dynamical aspects of structural engineering. It has been exciting to gain further insight into this field, by considering the aeroelastic effects of cable-supported bridges subjected to wind loads, and intriguing to realise that there is still much to learn. Even though there have been challenges to overcome during the study, the theoretical insights as well as the life lessons of organising a big project, are something I will take with me.

I would like to thank my main supervisor Ole Øiseth for valuable discussions and guidance during the study. His knowledge of the field and ability to lead me in the right direction, have been inspirational. Also, it would not have been possible to complete the project without access to the numerical routines he prepared. I would also like to thank Jan Håvard Nordtug for providing much needed technical assistance during the study, as well as fruitful discussions during coffee breaks. Lastly, big thanks are given to my parents, who proofread the thesis, and provided motivational support during a hectic period.

Georg A. Bugge
Trondheim, June 17, 2014

Summary

In the present study, a reliability analysis of the Hardanger Bridge was performed, by assessing the probability that multimodal flutter will occur. The self-exiting forces which reduce the effective damping and stiffness of the bridge, are formulated in terms of flutter derivatives. Measurements of flutter derivatives are available through section testing, and contrary to previous studies, also measurements for horizontal derivatives were used in the present work. The derivatives are modelled as stochastic variables. Two different modelling choices have been suggested. The thesis shows that only one of these provides reliable estimates.

Using random realisations of the stochastic distribution of flutter derivatives as input, the multimodal flutter equation was solved for a large number of simulations, providing distributions of critical speed to use in the reliability analysis. Since horizontal flutter derivatives were available, it was investigated whether horizontal modes impact the flutter limit. Thus, probabilistic distributions have been prepared for four different mode combinations, two of them including a number of horizontal modes. The study provides no evidence to suggest that horizontal effects are significant.

Due to the low probabilities involved in the flutter reliability analysis, the computational effort using traditional methods is very substantive. Therefore, an enhanced Monte Carlo method developed at NTNU was employed. Here, the original limit state function, $M = V_{Cr} - V_S$, was parameterized. Thereafter, the correct failure probability was estimated by means of extrapolation from the parameterized limit states. The use of the enhanced method to perform a flutter reliability analysis is, to the knowledge of the author, not described in literature previously. Based on the current simulations, the reliability index β was found in the range from 5.8-6.3, giving a failure probability per year as low as $1 \cdot 10^{-10} - 5 \cdot 10^{-9}$. However, there is an inherent uncertainty in these values, both due to uncertainty in the applied calculations, as well as the more general uncertainty in the field of flutter analysis. The calculations suggest that N_{sim} could be increased to achieve better accuracy.

In all three phases of the project, namely the modelling of flutter derivatives, solving of the eigenvalue problem defining multimode flutter, as well as the employment of the enhanced Monte Carlo method, MATLAB was used as the prime tool. Many of the MATLAB scripts being used in the study were prepared by Ole Øiseth at NTNU.

Sammendrag

I denne studien er det blitt utført en pålitelighetsanalyse av Hardangerbroen, ved å vurdere sannsynligheten for at multimodal instabilitet oppstår. De egeninduserte kreftene som reduserer broens effektive demping og stivhet, er formulert ved hjelp av aerodynamiske derivater. Målinger av aerodynamiske derivater er tilgjengelige gjennom testing av en seksjonsmodell, og i motsetning til i tidligere studier er også målinger av horisontale derivater blitt brukt i det foreliggende arbeid. Derivatene er modellert som stokastiske variabler. To forskjellige modelleringsvalg er blitt foreslått. Avhandlingen viser at bare ett av disse valgene gir pålitelige estimater.

Ved å generere tilfeldige realiseringer fra den stokastiske distribusjonen flutter-derivatene er modellert ved hjelp av, ble det multimodale egenverdiproblemet som definerer instabilitet løst for et stort antall simuleringer. Siden horisontale aerodynamiske derivater var tilgjengelig, ble det undersøkt hvorvidt horisontale moder påvirker den kritiske hastigheten. Sannsynlighetsfordelinger har blitt beregnet for fire forskjellige modekombinasjoner, hvorav to inkluderer horisontale moder. Studien inneholder ikke noe som tyder på signifikante horisontale effekter.

På grunn av de lave sannsynligheter involvert i pålitelighetsanalysen, er beregningsomfanget ved bruk av tradisjonelle numeriske metoder svært omfattende. Derfor ble en forbedret Monte Carlo-metode, utviklet ved NTNU, benyttet. Her ble den opprinnelige grensetilstandsfunksjonen $M = V_{Cr} - V_S$ parametrisert, hvorpå den korrekte sviktsannsynligheten ble beregnet ved hjelp av ekstrapolering fra de parameteriserte grensetilstandene. Bruk av den forbedrede fremgangsmåten for å utføre en pålitelighetsanalyse for kritisk hastighet er, såvidt forfatteren vet, ikke tidligere beskrevet i litteraturen. Basert på de nevnte simuleringer, ble pålitelighetsindeksen β beregnet til å ligge i området 5,8 til 6,3. Det gir en sviktsannsynlighet per år på $1 \cdot 10^{-10} - 5 \cdot 10^{-9}$. Det er imidlertid vesentlig usikkerhet knyttet til disse verdiene, både på grunn av usikkerhet i de anvendte beregninger, i tillegg til den mer generelle usikkerheten som er knyttet til aeroelastiske betraktninger. Beregningene antyder at N_{sim} bør økes ytterligere for å oppnå bedre nøyaktighet.

I alle tre faser av prosjektet, nemlig modellering av aerodynamiske derivater, løsning av egenverdiproblemet som definerer kritisk hastighet, så vel som anvendelse av den forbedrede Monte Carlo-metoden, ble MATLAB benyttet som viktigste verktøy. Mange av MATLAB-skriptene som brukes i studien, ble utarbeidet av Ole Øiseth ved NTNU.

Table of Contents

List of Tables

List of Figures

Chapter 1

Introduction

1.1 Background

The ability of a suspension bridge to vibrate has been known for a long time in the structural engineering literature. In 1836, the Brighton Chain Pier collapsed, with distinct torsional fluctuations in the period before it gave way. As a reference case, however, this incident fades compared to the collapse of the Tacoma Narrows Bridge. This infamous incident occurred only a few months after construction was completed, in a wind storm of very modest strength. The violent torsional fluctuations were a result of a mean wind velocity of only 19 m/s. When constructed, the bridge was counted as an example of modern bridge design, with a modest use of materials to construct the third longest bridge span at the time. After the collapse, the field of bridge engineering was forced to reconsider the development, and the investigations to the reasons of occurrence became a starting point of today's knowledge of aerodynamic bridge behaviour.

The fluctuations of the Tacoma Narrows Bridge could be described as a distinct, single-mode torsional motion, today known as torsional flutter. Today, it is often recognised that the critical mean wind velocity is limited by multimode flutter, in which several modes contribute to the fluctuations.

The Tacoma Narrows Bridge had a main span of 853 m. Today, it is common that suspension bridges employs main spans of 1200 m, while the record holder, the Akashi Kaikyo Bridge, currently has a main span of 1990 m. In Norway, the Hardanger Bridge, which was completed in 2013 and has a main span of 1310 m, takes the lead. Due to the sparse amount of traffic at the construction site, the bridge has a very slender design, making the aero-elastic stability limit an important concern.

1.2 Objective of work

While the mean flutter limit of the Hardanger Bridge has been assessed in previous studies, this study takes a step further, and investigates the probabilistic nature of the project, finally

providing a reliability analysis of the Hardanger Bridge. Here, the stochastic distribution of the critical flutter speed has been compared with the probabilistic distribution of the extreme 10 min mean wind value that is observed at the construction site during a year.

The analysis can be separated in three main parts. Firstly, the uncertainty of flutter derivatives is modelled. Secondly, a probabilistic analysis of the critical flutter speed is provided. Thirdly, the results are compared with the stochastic distribution of the yearly extreme 10-min mean wind value at the construction site.

In the analysis, two modelling alternatives for the flutter derivatives are investigated. Also, the variation in reliability due to different choices of mode combinations is reviewed. Since experimentally determined horizontal flutter derivatives has been available for the analysis, it is investigated whether horizontal mode contributions can be said to have an impact on the reliability of the bridge.

The thesis is organised in 8 chapters, the content of which will be briefly described her.

1.2.1 Organisation of the thesis

In chapter 2, the necessary theoretical background to define the multimode flutter limit is defined. The approach of Scanlan and Tomko [7] is used, describing self-induced forces, in which experimentally determined flutter derivatives plays a vital part.

In chapter 3, the most important statistical tools applied in the study are described. Also, the concept of reliability analysis is described on a basic level. Finally, the enhanced Monte Carlo method, which is used to estimate failure probabilities in this study, is presented.

In chapter 4, a review of some important limitations to the theory of flutter limit calculations, are provided. The chapter relies heavily on important findings in literature.

In chapter 5, all necessary preliminaries to perform the probabilistic analysis of the study are described. The heart of the chapter is the modelling of flutter derivatives, for which two modelling choices have been suggested. Also, a description of the flutter calculation routine is provided, and the stochastic distribution of the extreme mean wind value expected to occur during a year, is provided.

In chapter 6, the results from the analysis are presented. The critical speed distributions for the different modelling choices and mode combinations are described, and the results from the reliability analysis are presented.

In chapter 7, a discussion of the main findings from the analysis is given. The modelling choices are compared, and the validity of the results is discussed. Finally, a comparison of the most reliable findings is given.

Lastly, in chapter 8 an overview of the available conclusions is provided, and a brief list of suggestions for further investigations are given.

In the last section of this chapter, a description of the Hardanger Bridge is given.

1.3 The Hardanger Bridge

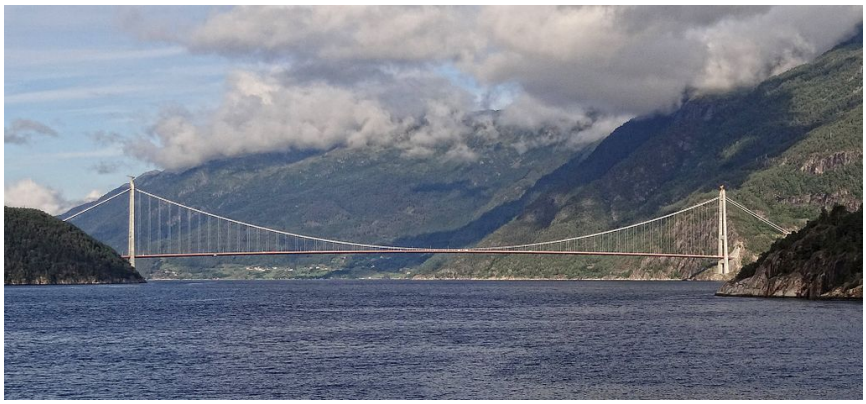

Figure 1.1: The Hardanger Bridge seen from east.

The Hardanger Bridge, which was completed in 2013, is the longest suspension bridge in Norway, with a main span of 1310 m. It is currently among the 10 longest suspension bridges in the world. The construction was started in the autumn 2009 with the erection of the towers, while the spinning of cables was started in 2011. Since the opening, the average traffic on the bridge has been approx. 1880 cars/day. Compared to other long suspension bridges, this is modest, and explains why the bridge was built with only two car lanes and one walking/biking lane. Because of its slender cross section, wind-induced vibrations of the bridge are a concern which has received much attention. The bridge was designed in accordance with Handbook 185 of The Norwegian Public Road Administration (SVV), which, among other requirements, demands that the aerodynamic behaviour of the bridge should be limited with:

$$V_{Cr} \geq 1.6 V_S \tag{1.1}$$

V_S is the 10-min mean wind velocity which is expected to have a return period of 500 years, valid for the construction site. This design wind speed is found in sec. 5.6 to be $V_S = 43\mathrm{m/s}$, which means that the critical speed limit should be at least 69 m/s.

The bridge crosses the Hardanger fjord between Vallavik and Bu, and is a part of Rv. 13 and Rv. 7. It replaced the ferry crossing of the same fjord, which was a well-known bottleneck on one of the main roads between Oslo and Bergen, the two largest cities in Norway 1.2.

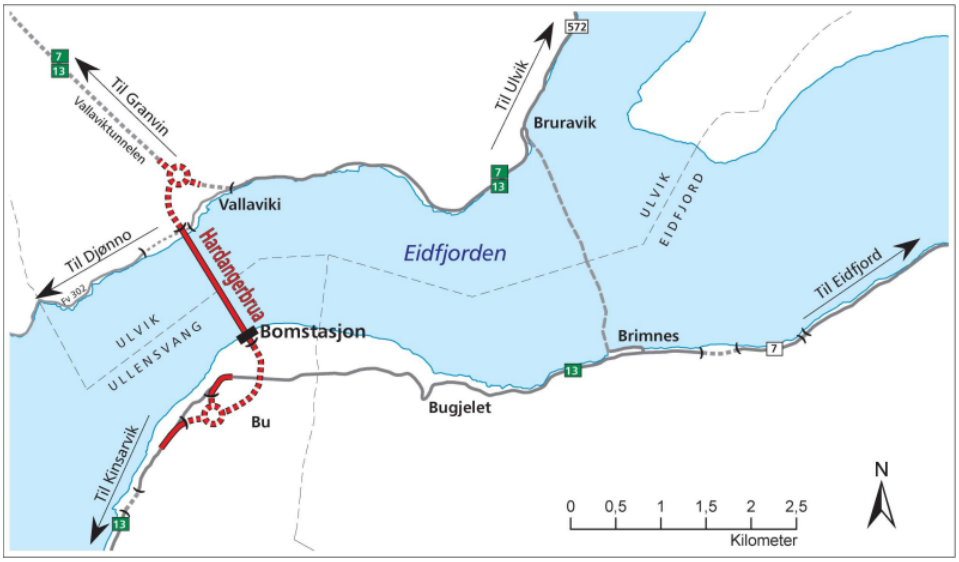

Figure 1.2: Overview of the Hardanger Bridge project. [1]

The Hardanger Bridge has a total length of 1380 m, only 70 m longer than its main span. The sailing height is 55 m, while the bridge pylons reach 200 m above sea level. None of these specifications are extreme compared to other long suspension bridges; however, the unusually narrow bridge girder makes the bridge an interesting project. The width is 18.3 m, and the distance between the two cables is only 14.3 m. When comparing with some other long bridges, it is found that the Hardanger Bridge is one of the most slender [8]. A front elevation of the bridge is shown in fig. 1.3. At midpoint, the driving lane is elevated 63.5 m above sea level, while the elevation is 52 m by the pylons.

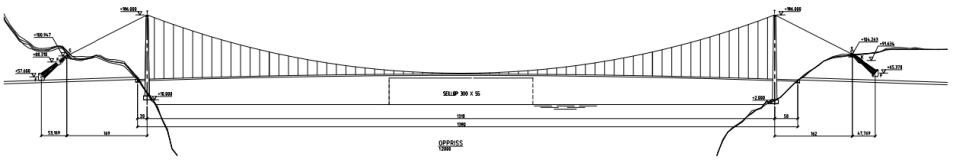

Figure 1.3: Front elevation of the Hardanger Bridge. [1]

The girder of the bridge is made of a stream-lined, closed steel box, and the geometry of the cross section is depicted in fig. 1.4. To optimize the aerodynamic behaviour of the bridge, guide vanes were included to reduce vortex shedding effects. To increase stiffness, there are transverse bulkheads every four meters. The sections were produced in 15 m lengths. Four lengths were welded together to one 60 m section, and these sections were transported to the construction site by boat.

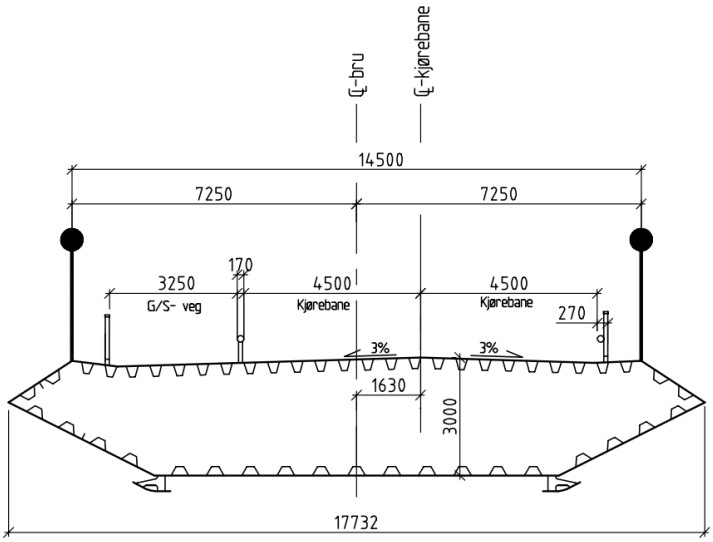

Figure 1.4: Cross section of the girder. All dimensions in millimeters. [1]

Chapter 2

Wind dynamics

2.1 Introduction

The total wind load on a bridge deck may be separated in four parts,

$$q_{tot} = \overline{q} + q_{buff} + q_v + q_{se} \tag{2.1}$$

- $\overline{q}$ is the time-averaged mean wind load, which give rise to static load effects,
- q_{buff} is fluctuating wind loads due to air turbulence. This phenomenon is also known as buffeting.
- q_v is the load due to vortex shedding effects into the wake of the body.
- q_{se} stem from interaction between the wind flow and the oscillating bridge deck, so-called motion-induced wind loads.

For cable-supported bridges, q_{se} becomes the dominant term in (2.1) when the wind velocity increases, and certain high wind velocities can cause motion-induced instability. Instability occurs when the energy input from the motion-induced wind load is equal to the energy dissipated by structural damping, and is associated with a critical wind velocity. When the net energy is zero, free motion with large deflections is the possible result. It is usual to distinguish between four different types of motion-induced instabilities.

- Static divergence
- Galloping
- Torsional flutter
- Coupled flutter

Static divergence occurs when the total stiffness becomes negative. This is a static instability effect usually seen on torsional motion.

Galloping is related to the damping term of vertical motion, and is not likely to occur for streamlined bridge sections. More often, it is seen on ice covered power lines. For bridge structures, flutter motion is more likely to occur.

Torsional flutter involves the motion of one single, torsional mode. Notably, the collapse of Tacoma Narrow Bridge was a result of torsional flutter at a relatively low wind speed. When the body of the bridge section is bluff, this is more likely to occur, whereas for streamlined sections, it is more rarely seen.

Coupled flutter remains the issue of greatest concern to the structural engineer. Still, at least one torsional mode is needed in order for instability to occur; however, also other modes contribute to instability. *Bimodal* flutter occurs if the in-wind eigenfrequency of one torsional mode and one vertical mode reaches the same value, possibly introducing violent fluctuations of the bridge girder. This motion often is the basis for multi mode flutter; however, if more than two modes are contributing to flutter, critical speed can be reached without two in-wind eigenfrequencies reaching the same value. Because multimode flutter generally is seen to be the limiting phenomenon for bridges, and because the solving procedure easily calculates critical speed for the three other types of instabilities, multimode flutter analysis is the present state of art when assessing problems involving self-exited forces. To develop a mathematical formulation of the multimode flutter problem, it is necessary to define the loads that contribute to self-exiting motion.

2.2 Self-exited forces

The general wind field varies with time and space, and is made up of a stationary, horizontal component, as well as turbulence components in all three directions. In general, the instantaneous wind velocity vector is described by

$$\begin{aligned} U(x,y,z,t) &= V(x,y,z) + u(x,y,z,t) \\ v(x,y,z,t) & \\ w(x,y,z,t), & \end{aligned} \tag{2.2}$$

where u and v are the horizontal turbulence components, V the stationary, mean wind component, and w is the vertical turbulence component. Because a bridge can be considered as a horizontal, line-like structure, the relevant expressions for the wind field may be simplified, because neither y nor z vary along the main axis of the bridge. The wind components contributing to motion thus consists of $U(x,t) = V + u(x,t)$ and $w(x,t)$, where x is, as of now, the coordinate along the main axis. It is assumed that the most critical situation occurs when the mean wind component attacks the bridge in a direction normal to the main axis. Therefore, v vanishes, as it attacks along the main span of the bridge, in which direction no significant movement is expected.

Davenport gave a full account of the response of line-like structures subjected to wind

loads. A fundamental assumption is that these forces are determined by Bernoulli's equation, which imposes a relation between instantaneous wind pressure and wind speed.

$$p_U(t) = \frac{1}{2}\rho[U(t)]^2 \tag{2.3}$$

where p_U is the wind pressure, ρ the density of air, and $U(t)$ a wind component that attacks the bridge deck when it is in its balancing position. The wind pressure is transferred to drag, lift and moment forces on the bridge section, given by

$$\begin{bmatrix} q_D(x,t) \\ q_L(x,t) \\ q_M(x,t) \end{bmatrix} = \frac{1}{2}\rho V_{rel}(x,t)^2 \begin{bmatrix} DC_D(\alpha) \\ BC_L(\alpha) \\ B^2C_M(\alpha) \end{bmatrix} \tag{2.4}$$

V_{rel} is introduced as the speed of the *total* wind component, relative to the motion of the bridge section. q_D attacks along the direction of V_{rel}, q_L in the normal direction, while q_M is a moment force. C_D, C_L, C_M are static load coefficients that depend on the angle of incidence, as well as the shape and surface of the body subjected to wind pressure. All forces are assumed to attack the mass center of the bridge. While the formulas in (2.4) have a very simple form, the expressions are not convenient to determine displacement components in the structural axes, ie. $r_y(x,t)$, $r_z(x,t)$ and $r_\theta(x,t)$. Therefore, it is practical to transform these forces into q_y, q_z and q_θ, which are assumed to attack in the respective directions. The terms, directions and displacement components which have been introduced here are explained in fig. 2.1.

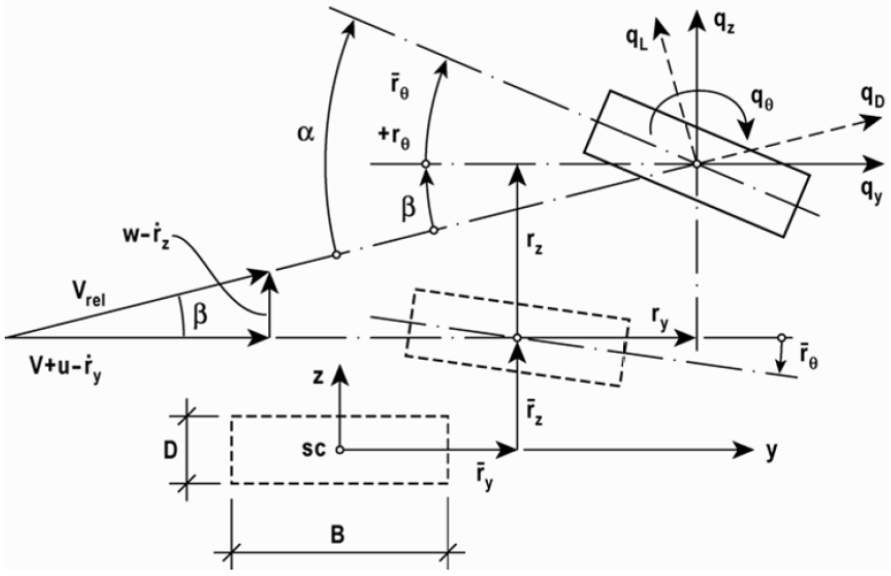

Figure 2.1: Bridge deck subjected to wind forces [2].

Performing the transformation, it can be shown that (2.4) changes into

$$\begin{bmatrix} q_y(x,t) \\ q_z(x,t) \\ q_\theta(x,t) \end{bmatrix} = \rho V \left(\frac{V}{2} + u - \dot{r}_y \right) \cdot \left(\begin{bmatrix} D\overline{C}_D \\ B\overline{C}_L \\ B^2\overline{C}_M \end{bmatrix} + \left(r_\theta + \frac{w - \dot{r}_z}{V} \right) \begin{bmatrix} DC'_D \\ BC'_L \\ B^2C'_M \end{bmatrix} + \frac{w - \dot{r}_z}{V} \begin{bmatrix} -B\overline{C}_L \\ D\overline{C}_D \\ 0 \end{bmatrix} \right) \tag{2.5}$$

To get to these expressions some simplifications have been made. Firstly, $C_n, n \in \{D, L, M\}$ are seen to be nonlinear flow incidence dependent load coefficients, however, here they are linearized with

$$C_n(\alpha) = C_n(\overline{\alpha}) + \alpha_f C'_n(\overline{\alpha}) = \overline{C}_n + \alpha_f C'_n, \tag{2.6}$$

$\overline{\alpha}$ and α_f being the mean value and the fluctuating part of the angle of incidence, respectively. See fig. 2.1.

Secondly, it is assumed that the turbulence components u, w are small compared to V, and furthermore that structural displacements are also small. Then, β is small, meaning that $\cos(\beta) \approx 1$ and $\sin(\beta) \approx \tan(\beta) \approx (w - \dot{r}_z)/V$, and higher order terms of u, w and $\dot{r}_i, i \in \{x, y\}$ are negligible.

The load formulation in (2.5) includes both static and dynamic parts, which can be ascribed to velocity fluctuations in the wind flow, as well as dynamic, motion-induced contributions. Comparing with (2.1), it is seen that both $\overline{q}$, q_{buff} and q_{se} are accounted for in this formulation. If (2.5) were written out, $\overline{q}$ would be the part depending solely on V, q_{buff} the part depending on V, u, w, while q_{se} consists of the V, r_i and $\dot{r}_i$ dependent terms. Flutter is determined by the latter part. It is a basic assumption that these forces can be considered independent of each other. In (2.7), the terms of self-exited forces are gathered.

$$\begin{aligned} q_{y,se}(t) &= \frac{1}{2}\rho V^2 B \left(-2\,(D/B)\,\overline{C}_D \frac{\dot{r}_y}{V} - \left((D/B)\,C'_D - \overline{C}_L \right) \frac{\dot{r}_z}{V} + (D/B)\,C'_D r_\theta \right) \\ q_{z,se}(t) &= \frac{1}{2}\rho V^2 B \Big(-2\overline{C}_L \frac{\dot{r}_y}{V} - (C'_L + (D/B)\overline{C}_D) \frac{\dot{r}_z}{V} + C'_L r_\theta \Big) \\ q_{\theta,se}(t) &= \frac{1}{2}\rho V^2 B^2 \Big(-2\overline{C}_M \frac{\dot{r}_y}{V} - C'_M \frac{\dot{r}_z}{V} + C'_M r_\theta \Big) \end{aligned} \tag{2.7}$$

While the formulation contributes significantly to the understanding of self-exited forces, (2.7) has some limitations that make it unsuitable for practical cases. The theory is valid only when the in-wind oscillation period of the structure is high, compared to the time it takes for the air flow to travel the distance across the section. Because it only applies when the bridge fluctuates slowly, Davenport's theory is called quasi-static. Also, it is seen that (2.7) does not provide any damping terms connected to torsional motion ($\dot{r}_\theta$ is not present), as would be expected from experiments. [8]

Scanlan and Tomko [7] introduced another approach, using so-called aerodynamic derivatives to express the self-exited forces. With this approach, aerodynamic damping and stiffness terms are provided for each degree of freedom.

$$
\begin{aligned}
q_{y,se} &= \frac{\rho V^2 B}{2}\left(KP_1^*\frac{\dot{r_y}}{V} + KP_2^*\frac{B\dot{r_\theta}}{V} + K^2P_3^*r_\theta + K^2P_4^*\frac{r_y}{B} + KP_5^*\frac{\dot{r_z}}{V} + K^2P_6^*\frac{r_z}{B}\right)\\
q_{z,se} &= \frac{\rho V^2 B}{2}\left(KH_1^*\frac{\dot{r_z}}{V} + KH_2^*\frac{B\dot{r_\theta}}{V} + K^2H_3^*r_\theta + K^2H_4^*\frac{r_z}{B} + KH_5^*\frac{\dot{r_y}}{V} + K^2H_6^*\frac{r_y}{B}\right)\\
q_{\theta,se} &= \frac{\rho V^2 B^2}{2}\left(KA_1^*\frac{\dot{r_z}}{V} + KA_2^*\frac{B\dot{r_\theta}}{V} + K^2A_3^*r_\theta + K^2A_4^*\frac{r_z}{B} + KA_5^*\frac{\dot{r_y}}{V} + K^2A_6^*\frac{r_y}{B}\right)
\end{aligned}
\tag{2.8}
$$

Here, P_i^*, H_i^*, A_i^*, $i \in \{1, 2, \ldots, 6\}$ are the aerodynamic derivatives. These derivatives are functions of the reduced frequency K, which combines two parameters that are very closely related to the fluctuations of the bridge.

$$K = \frac{B\omega}{V}, \tag{2.9}$$

where ω is the frequency of motion. K combines P_i^*, H_i^*, A_i^* have to be experimentally determined, and for practical reasons, they are often modelled as a function of the reduced *velocity*, $V_{red} = 1/K$.

Comparing (2.7) and (2.8), it seems as if terms such as KP_1^* and $K^2A_4^*$ are just a rewrite of the load coefficient expressions in (2.7). However, while the load coefficients are derived assuming static (non-vibrating) conditions, the expressions in the latter equation should be referred to as *motional* derivatives. Equality can be assumed only when K approaches zero. Among other things, this affects the way the values are experimentally determined. The static load coefficients can be found by means of a fixed model of the bridge, while a dynamic model is needed to find the aerodynamical flutter derivatives.

Reorganising, we find that (2.8) can be expressed as

$$\mathbf{q}_{se} = \mathbf{C}_{ae} \cdot \dot{\mathbf{r}} + \mathbf{K}_{ae} \cdot \mathbf{r} \tag{2.10}$$

with $\mathbf{q}_{se} = \begin{bmatrix} q_{y,se} & q_{z,se} & q_{\theta,se} \end{bmatrix}^{\mathrm{T}}$, and

$$
\mathbf{C}_{ae} = \frac{\rho B^2}{2}\omega \begin{bmatrix} P_1^* & P_5^* & BP_2^* \\ H_5^* & H_1^* & BH_2^* \\ BA_5^* & BA_1^* & B^2A_2^* \end{bmatrix}, \mathbf{K}_{ae} = \frac{\rho B^2}{2}\omega^2 \begin{bmatrix} P_4^* & P_6^* & BP_3^* \\ H_6^* & H_4^* & BH_3^* \\ BA_6^* & BA_4^* & B^2A_3^* \end{bmatrix}
\tag{2.11}
$$

$\omega = \omega(V)$ is the in-wind, mean wind velocity dependent eigen-frequency of motion.

2.3 The multimode flutter problem

A modal approach is used to define the multimode flutter problem. The fluctuating part of the structural displacement, $\mathbf{r}(x, t)$ is defined as the sum of products between natural eigenmodes $\boldsymbol{\phi}_i(x)$ and generalized degrees of freedom $\eta_i(t)$. In matrix form,

$$\mathbf{r}(x,t) = \mathbf{\Phi}(x)\boldsymbol{\eta}(t), \tag{2.12}$$

where

$$\begin{aligned}
\mathbf{\Phi}(x) &= \begin{bmatrix}\boldsymbol{\phi}_1(x) & \cdots & \boldsymbol{\phi}_i(x) & \cdots & \boldsymbol{\phi}_{N_{mod}}(x)\end{bmatrix} \\
\boldsymbol{\eta}(t) &= \begin{bmatrix}\eta_1(t) & \cdots & \eta_i(t) & \cdots & \eta_{N_{mod}}(t)\end{bmatrix}^T \\
\boldsymbol{\phi}_i(x) &= \begin{bmatrix}\phi_y(x) & \phi_z(x) & \phi_\theta(x)\end{bmatrix}_i^T
\end{aligned} \tag{2.13}$$

If all eigenmodes are included, (2.12) is exact, for practical purposes N_{mod} eigenmodes are chosen so that adequate accuracy is achieved. Dynamic equilibrium conditions are defined in modal space by the familiar differential equation,

$$\tilde{\mathbf{M}}_\mathbf{0}\ddot{\boldsymbol{\eta}}(t) + \tilde{\mathbf{C}}_\mathbf{0}\dot{\boldsymbol{\eta}}(t) + \tilde{\mathbf{K}}_\mathbf{0}\boldsymbol{\eta}(t) = \mathbf{Q}_\mathbf{se} \tag{2.14}$$

$\tilde{\mathbf{M}}_\mathbf{0}$, $\tilde{\mathbf{C}}_\mathbf{0}$ and $\tilde{\mathbf{K}}_\mathbf{0}$ are the modal mass, damping and stiffness matrix respectively, where subindex 0 indicates that the structural properties are obtained for still-air conditions. Due to the properties of a modal analysis, the off-diagonal terms of $\tilde{\mathbf{M}}_\mathbf{0}$ are cancelled out, while the diagonal terms are given by

$$\tilde{M}_{0,i} = \int_L \boldsymbol{\phi}_i^T(x)\mathbf{M}_\mathbf{0}\boldsymbol{\phi}_i(x)\,\mathrm{d}x \tag{2.15}$$

with $\boldsymbol{\phi_i}$ from (2.13) and $\mathbf{M_0}$ given as

$$\mathbf{M}_\mathbf{0} = \begin{bmatrix} m_y(x) & 0 & 0 \\ 0 & m_z(x) & 0 \\ 0 & 0 & m_\theta(x) \end{bmatrix} \tag{2.16}$$

$m_y(x)$ and $m_z(x)$ are the distributed mass along the main span of the bridge (normally, $m_y(x) = m_z(x)$), while $m_\theta(x)$ is the mass moment of inertia of the cross-section. Associated with each eigenvector $\boldsymbol{\phi}_i(x)$ are the eigenfrequency $\omega_{0,i}$ and the modal damping coefficient $\zeta_{0,i}$. Combining (2.15), (2.16) and these parameters provide

$$\begin{aligned}
\tilde{\mathbf{M}}_\mathbf{0} &= \mathrm{diag}(\tilde{M}_{0,i}) \\
\tilde{\mathbf{C}}_\mathbf{0} &= \mathrm{diag}(2\zeta_{0,i}\omega_{0,i}\tilde{M}_{0,i}) \qquad i \in \{1,\ldots,N_{mod}\} \\
\tilde{\mathbf{K}}_\mathbf{0} &= \mathrm{diag}(\omega_{0,i}^2\tilde{M}_{0,i})
\end{aligned} \tag{2.17}$$

Also, $\mathbf{Q_{se}}$ are the accumulated, self-exited forces on the bridge, given by

$$\mathbf{Q}_\mathbf{se} = \tilde{\mathbf{C}}_{ae}(V,\omega)\dot{\boldsymbol{\eta}} + \tilde{\mathbf{K}}_{ae}(V,\omega)\boldsymbol{\eta} \tag{2.18}$$

$$\tilde{\mathbf{C}}_{ae} = \begin{bmatrix} \ddots & & \iddots \\ & \tilde{C}_{ae,ij} & \\ \iddots & & \ddots \end{bmatrix}, \qquad \tilde{\mathbf{K}}_{ae} = \begin{bmatrix} \ddots & & \iddots \\ & \tilde{K}_{ae,ij} & \\ \iddots & & \ddots \end{bmatrix} \tag{2.19}$$

where

$$\begin{bmatrix} \tilde{C}_{ae,ij} \\ \tilde{K}_{ae,ij} \end{bmatrix} = \int_{L_{exp}} \begin{bmatrix} \boldsymbol{\phi}_i^T(x)\mathbf{C}_{ae}\boldsymbol{\phi}_j(x) \\ \boldsymbol{\phi}_i^T(x)\mathbf{K}_{ae}\boldsymbol{\phi}_j(x) \end{bmatrix} \mathrm{d}x, \tag{2.20}$$

L_{exp} being the length of the wind-exposed part of the bridge. Often, $L_{exp} \approx L$, and equality is assumed. $\mathbf{C}_{ae}$ and $\mathbf{K}_{ae}$ are defined in (2.11). Combining (2.14) and (2.18), and introducing the characteristic solution vector

$$\boldsymbol{\eta} = \hat{\boldsymbol{\eta}} \mathrm{e}^{\lambda_n t}, \tag{2.21}$$

the quadratic, complex eigenvalue problem which defines the structural displacements of the bridge, is provided as

$$\left(\lambda_n^2 \tilde{\mathbf{M}}_{\mathbf{0}} + \lambda_n \left(\tilde{\mathbf{C}}_{\mathbf{0}} - \tilde{\mathbf{C}}_{ae}\left(V,\omega\right)\right) + \left(\tilde{\mathbf{K}}_{\mathbf{0}} - \tilde{\mathbf{K}}_{ae}\left(V,\omega\right)\right)\right) \hat{\boldsymbol{\eta}} = 0, n \in \{1,2,\ldots,2N_{mod}\} \tag{2.22}$$

(2.22) can be transformed into a standard, complex, nonlinear eigen-value problem, to which well-known iteration techniques apply. This produces $2N_{mod}$ complex eigenvalues λ_n, with associated eigenvectors $\hat{\boldsymbol{\eta}}$. The solutions come as complex conjugated pairs, which means that if $\lambda_{2n-1} = a_n + ib_n$ solves (2.22), then $\lambda_{2n} = a_n - ib_n$ is also a solution. These two solutions leads to the same eigenvector, which means that half of the solutions are redundant. To see what physical meaning these solutions have, a comparison with a 1DOF system is explanatory. Then, (2.22) reduces to solving

$$m\lambda^2 + c_{tot}\lambda_n + k_{tot} = 0, \tag{2.23}$$

$$\Rightarrow \qquad \lambda^2 + 2\zeta_{tot}\omega\lambda + \omega^2 = 0 \tag{2.24}$$

where $c_{tot}, k_{tot}, \zeta_{tot}$ and ω are in-wind terms taking both structural and aerodynamical damping and stiffness into account. The transition (2.23)-(2.24) is made using $c_{tot} = 2\zeta_{tot}\omega m$ and $k_{tot} = \omega^2 m$. (2.24) is a simple quadratic equation, which has the solutions

$$\lambda = -\zeta_{tot}\omega \pm \omega\sqrt{1-\zeta_{tot}^2} \tag{2.25}$$

This expression extends to the multimode equation as well. Thus, by comparing terms, it is seen that $a_n = -\zeta_{tot,n}\omega_n$, $b_n = \omega_{dn} = \omega_n\sqrt{1-\zeta_{tot,n}^2}$, where ω_{dn} is the in-wind, damped frequency of motion. Finally, it is found that

$$\omega_n = \sqrt{a_n^2 + b_n^2}, \qquad \zeta_{tot,n} = -\frac{a_n}{\sqrt{a_n^2 + b_n^2}} \tag{2.26}$$

All values are specific for mode nr. n. These results are in accordance with theory regarding the traditional equation of motion ((2.22) without $\tilde{\mathbf{K}}_{ae}$ and $\tilde{\mathbf{C}}_{ae}$), see e.g. [9].

For low wind velocities, a_n is negative for all n, resulting in decaying motion. However, higher wind speed will increase the effects of $\tilde{\mathbf{C}}_{ae}$, ultimately (possibly) resulting in a situation with zero net damping. Mathematically, this is seen when $a_n \geq 0$ for some n. Thus, to find the flutter wind speed limit, the common solution procedure searches for a combination of V and ω_n where $a_n = 0$. [10] gives a thorough review of the most common iterative technique, which were suggested by Agar [11]. A description is also given in sec. 5.5.

2.4 Properties of flutter derivatives

As mentioned in sec. 2.1, flutter can occur in various forms. The infamous Tacoma Bridge collapsed primarily as a result of pure torsional flutter, at a very low wind speed [12]. Even before that, it was realised that bimodal flutter, where one torsional mode couples with a vertical mode, could occur for streamlined aerofoils [13].

The determination of aerodynamic derivatives is important to find the critical flutter speed. As it is the coupling of vertical and torsional motion which has been seen to have the most influence on critical flutter speed, the aerodynamical derivatives defining this coupling, $H_i^*, A_i^*, i \in \{1,2,3,4\}$, were the first to be identified. Theodorsen, working in the field of aeronautics, provided theoretical expressions for the self-exited forces for a flat plate, showing that they could be considered linear in the structural displacements and their two first time derivatives [13]. Later, Scanlan showed that this way of modelling self-induced forces was valid also for bridge decks [7]. However, as the importance of second time derivatives turned out to be negligible in wind engineering, they were omitted in his expressions, resulting in a formulation equivalent to the ones being shown in (2.8). Parenthetically, including second derivatives would give an aerodynamic mass matrix, $\tilde{\mathbf{M}}_{ae}$, to be included in (2.18).

It was also demonstrated that the aerodynamic derivatives could be determined using wind tunnel testing. Until recently, it is only the eight derivatives mentioned in the previous paragraph which have been determined experimentally, partly because horizontal motion were not considered to affect the critical flutter speed, and partly because section models were constructed to allow for motion only in vertical and angular direction. When performing a 3D flutter analysis, expressions also for the ten remaining derivatives are needed. It is common to model these using the quasi-static load coefficients from (2.7), giving the following expressions:

$$
\begin{aligned}
&P_1^* = -2\overline{C}_D \frac{D}{B}\left(\frac{1}{K}\right), \qquad P_5^* = (\overline{C}_L - \frac{D}{B}C'_D)\left(\frac{1}{K}\right), \qquad P_3^* = C'_D \frac{D}{B}\left(\frac{1}{K}\right)^2, \\
&H_5^* = -2\overline{C}_L\left(\frac{1}{K}\right), \qquad A_5^* = -2\overline{C}_M\left(\frac{1}{K}\right), \qquad P_2^* = P_4^* = P_6^* = H_6^* = H_6^* = 0
\end{aligned}
\tag{2.27}
$$

The flutter analysis of the Akashi Kaikyo Bridge, for which significant horizontal cou-

pling was observed, was performed using these quasi-static values [14]. Also, the Hardanger Bridge has previously been assessed this way.

Even though quasi-static coefficients have been used in recent studies, all 18 derivatives have been experimentally determined with section model setups for different bridges, allowing for motion in three directions, see eg. [15],[6].

2.5 Bimodal flutter

In sec. 2.3, the eigenvalue problem for multimode flutter was defined. Even though this equation can be solved for a high number of modes, in practice it is often seen that the flutter speed converges after a few selected modes are included. Specifically, the multi mode flutter solution is often seen to be dominated by the two modes that would give bimodal flutter. A vertical and a torsional mode dominate the motion at flutter speed, while additional modes give limited contributions. However, while bimodal flutter is defined to occur at the point where in-wind frequencies reaches the same value, giving large fluctuations for both modes, multi mode flutter motion is usually dominated by only one of these modes. Still, it is instructive to describe the properties of a bimodal solution more closely.

Bimodal coupling occurs when a torsional mode and a vertical mode couple with each other at the same frequency. In still-air, the eigenfrequencies of the two modes are normally separated. For coupling to occur, the in-wind frequencies have to converge towards each other, ultimately reaching the same value. The mean wind velocity where this occurs is thus the critical speed.

Modal coupling is more likely to occur with modes that have their largest deflections at the same part of the structure. Above all, this means that a vertical, symmetrical mode is not likely to couple with an asymmetrical torsional mode, and vice versa. The modes providing the lowest flutter limit often turns out to be the first symmetrical vertical mode coupling with the first symmetrical torsional mode. However, both for the Hardanger Bridge and the Hålogaland Bridge, it was necessary to include three modes to determine flutter speed with accuracy [8],[16]. Also, it was seen that the 2nd symmetrical vertical mode was more likely to couple compared with the 1st symm. vertical. Shape-wise similarity and difference between frequencies are seen to be very important indications as to whether or not modes couple.

Shape-wise similarity can be measured with the mode shape similarity coefficient,

$$\psi_{z\theta} = \frac{\int_0^L \phi_z(x)\phi_\theta(x)\,dx}{\int_0^L \phi_z^2(x)\,dx} \frac{\int_0^L \phi_z(x)\phi_\theta(x)\,dx}{\int_0^L \phi_\theta^2(x)\,dx} \tag{2.28}$$

If the mode forms are exactly equal to each other, $\psi_{z\theta} = 1$, while dissimilar modes result in $\psi_{z\theta}$ approaching zero. The bimodal flutter limit is seen to decrease with increasing shape similarity.

Modal coupling is more likely to occur when the difference between the still-air, natural frequencies of the two modes are small [17]. This can be measured by the frequency ratio $\gamma_\omega = \frac{\omega_y}{\omega_\theta}$, which normally is found to be limited by $\gamma_\omega \geq 1$. For a flat plate, it is

found that V_{cr} reaches a minimum for $\gamma_\omega \approx 1.1$ [18]. Increased wind speed reduces the torsional eigenfrequency, while the vertical frequency increases, thus reducing the in-wind ratio towards unity. Bridge designers often search a configuration where the frequencies of these modes are well separated. This can be achieved by using cross sections that increase torsional stiffness, the closed-box section of the Hardanger Bridge, seen in fig. 1.4, being an example.

While it is often seen that two of the considered modes in a multi mode analysis give the most significant contributions, it is important to assess whether including more modes in the analysis might reduce critical speed.

In [8], using a rectangular cross section as a case study, Øiseth investigated when a bimodal analysis could be considered to give accurate results, and when further inquiries should be performed. Among the findings were that

- If two pairs of shape-wise similar modes, the pairs being shape-wise dissimilar, were included in a multimode flutter analysis, there were no significant multimodal effects present. The flutter limit was determined by the pair providing the lowest limit alone.

- If two torsional modes were included in multimode analysis with one vertical mode, the separation of the two torsional frequencies strongly influenced the reduction of the flutter limit. With a large frequency ratio between the two torsional eigenfrequencies, very little reduction was observed, while significant contributions were seen with equal frequencies. Also, shape-wise similarity influenced the flutter limit.

- If two vertical modes and one torsional mode were included, the contributions from the second vertical mode could be significant even with the two vertical frequencies being well separated.

The results suggest that shape-wise similarity should be the prime focus when including modes, and high numbered vertical modes should also be focused upon.

As the comprehension of the modal coupling phenomena increased, the possible inclusion of lateral modes was looked into. Although the traditional view maintained that lateral modes do not couple significantly with vertical/torsional motion, extended research suggests that this stance must be modified. Dyrbye & Hansen states that lateral mode contribution may have significant effect for long span bridges, more explicitly bridges with main span in the range of more than 1-2 km [18]. Analysis performed on the Akashi-Kaikyo Bridge, currently the longest suspension bridge in the world, with a main span of 1990m, also showed that lateral modes affected the flutter limit. Here, it was determined that three vertical modes and two horizontal modes together with one torsional mode (all symmetric) were needed to achieve accuracy.

Chapter 3

Statistics and structural reliability

In this chapter, an introduction to the field of reliability analysis is provided. After a brief survey of the theory behind, some common solution strategies to problems involving failure probability are suggested. Most notably, the concept of Monte Carlo simulations are introduced, and the theory behind an extension to the method, hereby denoted the *enhanced* Monte Carlo method, are presented. The field of reliability analysis is in its nature probabilistic, and thus, some statistical knowledge becomes important. In the first part of the chapter, an overview of the statistical tools that are used throughout this thesis, are presented.

3.1 Probability distributions

Statistics is concerned with making inferences about sample spaces of random variables. Thus, the field is relevant to almost all engineering problems, because uncertainty is a component in the sizes that are studied. For example, the maximal snow load on a roof during a year is not known in advance. However, it is possible to provide a probability that the load are of a certain size. A function that returns the probability for *all* the possible outcomes of such questions is called a probability distribution function (PDF); here we choose to denote it $f_X(x)$.

f_X and the probability of events are obviously closely related. For sample spaces that can take on an infinite number of values, as the example of snow load, the probability distribution provides meaning only when considering intervals of the sample space. When Δx is infinitesimal, $f_X(x)$ should be understood as the probability of X taking on a value between x and $x + \Delta x$. In (3.1), the continuous distribution function is defined.

$$\begin{aligned} \int_{-\infty}^{\infty} f_X(x)\,\mathrm{d}x &= 1 \\ f_X(x) &\geq 0, x \in R \\ P(a < X < b) &= \int_a^b f_X(x)\,\mathrm{d}x \end{aligned} \tag{3.1}$$

We can now define the cumulative distribution function (CDF), which provides the probability of X being lower than a certain value.

$$F(x) = P(X \leq x) = \int_{-\infty}^{x} f_X(t)\,\mathrm{d}t, \tag{3.2}$$

where t is used as a dummy variable.

It is common to use parameters to describe the distribution functions that are used. All properties of a random variable are determined by its type of distribution and some necessary parameters. The mean μ_X and the variance σ_X^2 are very commonly used, defined by

$$\mu_X = \quad \mathrm{E}(X) \quad = \int_{-\infty}^{\infty} x \cdot f_X(x)\,\mathrm{d}x \tag{3.3}$$

$${\sigma_X}^2 = \mathrm{E}[(X - \mu_X)^2] = \int_{-\infty}^{\infty} (x - \mu_X)^2 \cdot f_X(x)\,\mathrm{d}x \tag{3.4}$$

The mean is the average value of the sample, while the variance is a measure of scatter, high variance means large scattering. If a series of observations is drawn from a sample with unknown properties, μ_X and σ_X can be estimated with

$$\hat{\mu}_X = \frac{1}{n}\sum_{i=1}^{n} x_i \tag{3.5}$$

$$\hat{\sigma}_X^2 = \frac{1}{n-1}\sum_{i=1}^{n} (x_i - m_X)^2, \tag{3.6}$$

respectively. Necessarily, there is uncertainty connected to these values.

3.1.1 Multi variable distributions

It is easy to extend the definition of probability distribution functions to a multi-variable domain. For a pair of variables X_1, X_2,

$$f_{X_1X_2}(x_1, x_2) = P(x_1 < X_1 < x_1 + \Delta x_1 \cap x_2 < X_2 < x_2 + \Delta x_2), \tag{3.7}$$

which is analogous to (3.1), (3.2).

For two random variables, the covariance provides a measure of their mutual linear dependence.

$$\mathrm{Cov}(X_1, X_2) = \sigma_{X_1 X_2} = \mathrm{E}[(X_1 - \mu_{X_1})(X_2 - \mu_{X_2})] \tag{3.8}$$

$$\tag{3.9}$$

(3.9) can be evaluated analytically in accordance with the last equality of (3.4). When no analytical expression is present, (3.10) provides an estimation.

$$\hat{\sigma}_{XY} = \frac{1}{n-1} \sum_{i=1}^{n} \left((x_{1i} - m_{X_1}) \, (x_{2i} - m_{X_2}) \right) \tag{3.10}$$

The covariance should be seen as a multivariate counterpart to σ_X^2, which is sensible also because (3.9) gives $\sigma_{XX} = \sigma_X^2$.

A normalised version of the covariance is defined by the correlation coefficient,

$$\rho_{X_1 X_2} = \frac{\sigma_{X_1 X_2}}{\sigma_{X_1} \sigma_{X_2}}, \tag{3.11}$$

which is limited by $-1 \leq \rho_{X_1 X_2} \leq 1$. Fig. 3.1 shows typical correlation coefficient values for three different population samples.

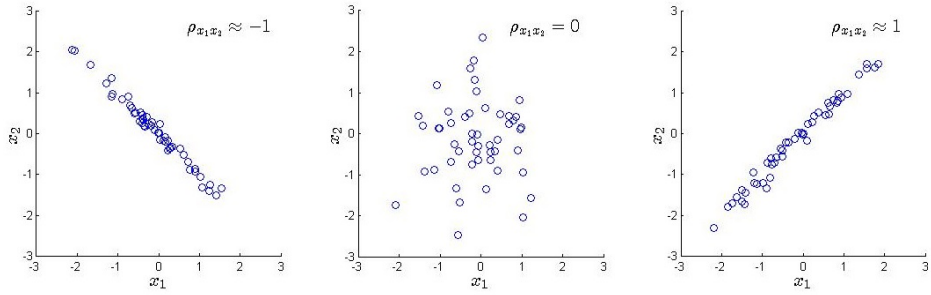

Figure 3.1: Illustration: Correlation values for three different data samples.

When there is no correlation between the variables,

$$f_{X_1 X_2}(x_1, x_2) = f_{X_1}(x_1) f_{X_2}(x_2) \tag{3.12}$$

The general n-dimensional distribution function for a vector of correlated variables, $\mathbf{X} = [X_1, X_2, \ldots, X_n]$, is generally denoted $f_{\mathbf{X}}(\mathbf{x})$.

$\mathbf{X}$ have mean

$$\mathrm{E}(\mathbf{X}) = [\mathrm{E}(X_1), \mathrm{E}(X_2), \ldots, \mathrm{E}(X_n)] \tag{3.13}$$

and covariance matrix

$$\mathbf{C_X} = \mathrm{Cov}(\mathbf{X}, \mathbf{X}^T) = \begin{bmatrix} \sigma_{11} & \sigma_{12} & \dots & \sigma_{1n} \\ \sigma_{21} & \sigma_{22} & \dots & \sigma_{2n} \\ \vdots & \vdots & \ddots & \vdots \\ \sigma_{n1} & \sigma_{n2} & \dots & \sigma_{nn} \end{bmatrix} \tag{3.14}$$

The simplification $\sigma_{ij} = \sigma_{X_i X_j}$ is used here. The definition in (3.9) implies that (3.14) is symmetric.

3.2 Regression analysis

Fig. 3.1 shows three data samples with varying degree of linear relation. Often, it is necessary to determine the properties of relationships between variables. The situation where $\mathrm{Cov}(X, Y) \equiv \pm 1$ describes a deterministic relationship between variables, and the equation $y = \alpha + \beta x$ holds for all x using some suitable α, β. However, for practical purposes such relations are *not* deterministic, and the true value of Y is given as

$$Y = \alpha + \beta x + \epsilon, \tag{3.15}$$

where ϵ is a random disturbance or error inherent in the model, commonly assumed as a random variable having zero mean and a variance of σ^2. Y thus becomes a random variable depending on the values of x and the distribution of ϵ, making the model in (3.15) probabilistic. Regression analysis deals with finding the best relationship between variables, as well as quantifying the strength of that relation. Also, the use of methods to predict response values is a part of the analysis.

The line $y = \alpha + \beta x$ is called the true regression line of the model. However, because the actual values of ϵ cannot be observed, it is not possible to define the true line, and α and β must be estimated from data samples taken from the populations described by the model. This estimate may be defined by the relation $\hat{y} = a + bx$. The regression would then involve reducing the error or residual of the model, $e = y - \hat{y}$ to a minimum. Given n data points $(x_i, y_i), i \in \{1, ldots, n\}$, taken from the model in (3.15), this is commonly done by minimizing the sum of squares of errors, i.e. finding a, b so that

$$SSE = \sum_{i=1}^{n} e_i^2 = \sum_{i=1}^{n} (y_i - \hat{y}_i)^2 = \sum_{i=1}^{n} (y_i - a - bx_i)^2 \tag{3.16}$$

is minimized. This is done by differentiating in (3.16) with respect to a and b, and setting these derivatives equal to zero. Doing this and solving for a and b, it is then found that

$$b = \frac{\sum_{i=1}^{n} (x_i - \overline{x})(y_i - \overline{y})}{\sum_{i=1}^{n} (x_i - \overline{x})^2}, \qquad a = \overline{y} - b\overline{x} \tag{3.17}$$

where $\overline{x}$ and $\overline{y}$ are the means of x_i and y_i, given by (3.6).

(3.17) defines estimates for α, β. Drawing two different data sets from the model, and calculating a and b for each set would most likely provide different results, implying that α and β also are random variables, depending on the distribution of the error term in (3.15). Proofs omitted, it can be shown that an unbiased estimate of σ^2 is given by

$$\hat{\sigma}^2 = \frac{SSE}{n-2} \tag{3.18}$$

Likewise, it can be shown that $\hat{\sigma}_A^2$ and $\hat{\sigma}_B^2$ are estimates of the variance a and b are distributed by, defined in (3.19).

$$\hat{\sigma}_A^2 = \frac{\sum_{i=1}^n x_i^2}{n\sum_{i=1}^n (x_i - \overline{x})^2}\hat{\sigma}^2, \qquad \hat{\sigma}_B^2 = \frac{1}{n\sum_{i=1}^n (x_i - \overline{x})^2}\hat{\sigma}^2 \tag{3.19}$$

For many practical applications, the variance of the error term takes on a larger value than the expressions seen in (3.19), which can be explained by their respective meaning. While $\hat{\sigma}^2$ is a measure of scatter of specific response measurements, from $\hat{\sigma}_A^2$ and $\hat{\sigma}_B^2$ it is possible to infer on the variance of the mean response. From the latter values it is possible to construct *confidence* intervals which work as bounds on the suggested mean response for a certain value of x. They can be interpreted in the same way as confidence intervals on the mean in a nonregression scenario.

Similarly, it is possible to construct bounds on a future predicted response. Obviously, these bounds are wider than the ones for the mean response. They are commonly called prediction intervals, and should be understood in the same way as the confidence intervals in 3.27. Fig. 3.2 illustrates the difference between these two concepts.

As a measure of the quality of fit, the coefficient of determination, R^2, is commonly introduced. It measures how well the variability inherent in the true model is explained by the fitted model, and is given as

$$R^2 = 1 - \frac{SSE}{SST} = 1 - \frac{\sum_{i=1}^n (y_i - \hat{y}_i)^2}{\sum_{i=1}^n (y_i - \overline{y})^2}, \tag{3.20}$$

where the total corrected sum of squares SST is introduced. R^2 takes a value close to unity if the quality of the fit is good, and approaches zero if the fitted model does not predict the response well. The value provides valuable information to whether the suggested model is adequate.

In (3.15), it was assumed that the error term had a constant, variance equally distributed about the mean of the response. This is an assumption that does not hold for all applications. Valuable information can be drawn by assessing the residuals of the model more closely, for example by plotting the data points (x_i, e_i) in a residual plot. Also other tools to assess the quality of the model do exist. Information gathered from such tools may lead to different conclusions, for instance that

1. the assumed model is adequate,

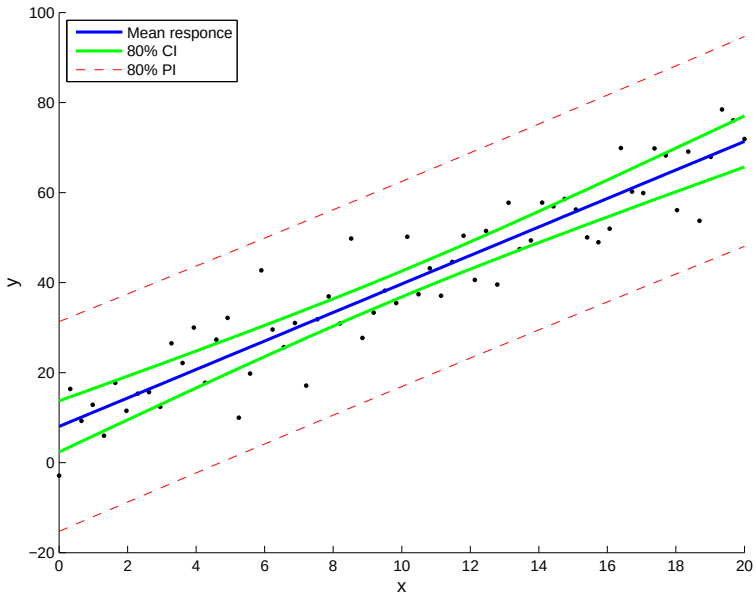

Figure 3.2: Expected mean response, confidence intervals and prediction intervals for future responses.

2. it is more suitable to use a nonlinear model,
3. the residuals display a non-homogenous behaviour,
4. it should be investigated if the response y depend on more than one variable.

In sec. 3.2.1, the latter situation will be given some concern. 3. is given concern in sec. 5.4.1

3.2.1 Multivariable linear regression

In the following, it is assumed that the response value y is linearly dependent of k independent variables $x_1, \ldots, x_k$, and that n observations $y_1, \ldots, y_n$ have been performed. The observations of the experiment can then be gathered in a matrix equation as

$$\mathbf{y} = \mathbf{X}\boldsymbol{\beta} + \boldsymbol{\epsilon}, \qquad \text{where}$$

$$\mathbf{y} = \begin{bmatrix} y_1 \\ \vdots \\ y_n \end{bmatrix}, \qquad \mathbf{X} = \begin{bmatrix} 1 & x_{11} & \ldots & x_{k1} \\ \vdots & \vdots & \ddots & \vdots \\ 1 & x_{1n} & \ldots & x_{kn} \end{bmatrix}, \qquad \boldsymbol{\beta} = \begin{bmatrix} \beta_0 \\ \beta_1 \\ \vdots \\ \beta_k \end{bmatrix}, \qquad \boldsymbol{\epsilon} = \begin{bmatrix} \epsilon_1 \\ \vdots \\ \epsilon_n \end{bmatrix} \tag{3.21}$$

x_{ij} is the observation number j of variable i, β_i are the model coefficients estimated by b_i, and ϵ_j are error terms analogous to that of (3.15). Now, minimizing the squared sum of errors involves solving the equation

$$\frac{\partial}{\partial \mathbf{b}}(SSE) = \mathbf{0}, \qquad SSE = (\mathbf{y} - \mathbf{Xb})^T(\mathbf{y} - \mathbf{Xb}) \tag{3.22}$$

finally giving

$$\mathbf{b} = (\mathbf{X^T X})^{-1}\mathbf{X^T y} \tag{3.23}$$

In sec. 3.2 it was mentioned that the regression model should sometimes be defined as nonlinear in x and y. In many cases, such models would need iterative techniques to be evaluated. However, as long as the model is linear in their parameter coefficients β_i, nonlinear models can be transformed so that they are suitable for linear regression analysis.

A special case of this applies when y is modelled as a polynomial in x, ie.

$$y = \beta_0 + \beta_1 x + \beta_2 x^2 + \ldots + \beta_k x^k + \epsilon \tag{3.24}$$

Setting $x_i = x^i, i \in \{1, 2, \ldots, k\}$ then automatically reduces to the multi variable regression model of (3.21).

3.3 Normal distribution

The normal distribution is the most important probability distribution in statistics. Its "strength" is explained by the central limit theorem. The theorem states when large samples of random variables are drawn from the same distribution, the distribution of the mean of these samples will converge towards the normal. Thus, the normal, or Gaussian, distribution is suitable for many types of populations. If it is uncertain which distribution type a random variable belongs to, a fitted normal distribution will often provide a good approximation.

The normal is a symmetric distribution described by means of the mean μ and variance σ^2, and it's bellshaped distribution curve is given by

$$f_X(x) = \frac{1}{\sqrt{2\pi}\sigma} \mathrm{e}^{-\frac{1}{2}\left(\frac{x-\sigma}{\sigma}\right)^2} \tag{3.25}$$

To define the properties of a random variable with normal distribution, the terminology $X = N(\mu, \sigma)$ is commonly used. Of special interest is the standard, normal distribution, with $\mu = 0, \sigma = 1$. All distributions can

$$X = N(\mu, \sigma) \Leftrightarrow Z = \frac{X - \mu}{\sigma} = N(0, 1) \tag{3.26}$$

The transformation of (3.26) enables to use certain reference values of the standard normal distributions, which can be found in tables or by using suitable computational software. The variance, or rather, the standard deviation $\sigma = \sqrt{\sigma^2}$, is a measure of scatter. In

a normally distributed population, about 68% of the total sample will have values within $\pm 1\sigma$ off the mean value. Similarly, the interval $\{\mu - 1.96\sigma, \mu + 1.96\sigma\}$ is found to contain 95% of the population. These types of intervals are called confidence intervals. Specifically, the $(1-\alpha)\cdot 100\%$ confidence interval is given by

$$CI_{1-\alpha} = \{\mu - z_{\frac{\alpha}{2}}\sigma, \mu + z_{\frac{\alpha}{2}}\sigma\} \tag{3.27}$$

Here, $z_{\frac{\alpha}{2}}$ is the value of a standard normal distribution that will be exceeded by $\frac{\alpha}{2}$ of the population. Fig. 3.3 illustrates how normal random variables are distributed.

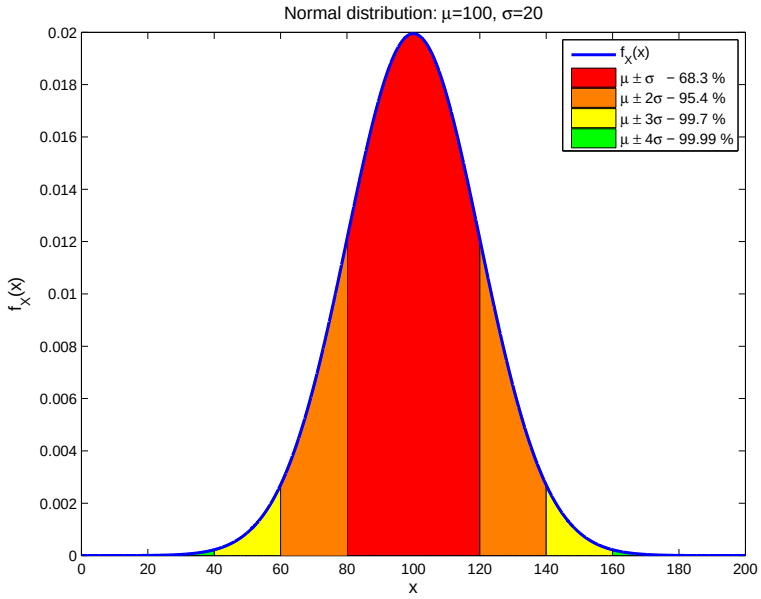

Figure 3.3: Distribution of a random variable $X = N(100, 20)$.

The cumulative distribution function (CDF) of the normal distribution cannot be expressed in closed form in terms of elementary functions, therefore, tables or computer programs are the common way to find these values. For calculations by hand, table values of the CDF of a standard normal variable x, denoted $\Phi(x)$, is a helpful tool.

3.4 Gumbel distribution - GEV I distribution

The Gumbel distribution is used to model the distribution of the maximum value of samples taken from another distribution. It is a special case of the general extreme value distribution, which, depending on some key distribution factors, is used to describe distributions of maximum or minimum values. Unlike the normal distribution, the Gumbel distribution is skewed, as the tail of the PDF is larger on the right side.

The Gumbel distribution is defined by the location parameter μ and the scale β. Using them, the PDF and CDF is defined as

$$f_X(x) = \frac{1}{\beta} \mathrm{e}^{-\left(\frac{x-\mu}{\beta} + \mathrm{e}^{-\frac{x-\mu}{\beta}}\right)}, \qquad F_X(x) = \mathrm{e}^{-\mathrm{e}^{-\frac{x-\mu}{\beta}}}, \tag{3.28}$$

respectively. The mean and standard deviation of a Gumbel distribution is given as $\mathrm{E}(X) = \mu + \gamma\beta$ and $\sigma = \beta\pi/\sqrt{6}$.

The Gumbel distribution is important for engineering purposes, because design loads on structures are often defined by their expected extreme value during some reference period. Sometimes, it is an open question if the Gumbel distribution or some of the other extreme value distributions should be used. A main difference to take into account is the fact that the Gumbel distribution is defined for all values of x, while the GEV II and III distributions have cut-off values for where the functions are defined.

3.5 Introduction to structural reliability

For the structural engineer, one of the main concerns when designing a structure is to ensure adequate safety. This goal can be pursued in various ways, but for some time, the usage of codes and standards has dominated the field. This approach is deterministic. Either the calculations tell that the structure is safe, or they show that it is not. However, when the code calculations tell about a safe structure, it does not imply that the structure is absolutely safe. On the contrary, it is crucial for the engineer to understand that there is no such thing as absolute safety. The codes ensure that the probability of failure is low enough for the purposes of the structure, but they tell nothing of the failure probability. For many applications, this knowledge is enough, while on other occasions there will be reasons to perform a probabilistic analysis of the structure in question.

The field of reliability analysis provides insight into the probabilistic nature of problems normally considered in a deterministic manner. In the following, some useful concepts in the field of structural reliability analysis are defined.

Reliability

> Reliability is the ability of an item or facility to perform its intended function for a specified period of time, under defined conditions. [19, 20].

With some nuances, the quote above is a usual way to define reliability. This is a rather broad definition; the use of words such as item, facility and function implies that reliability analysis can be applied on a wide range of problems. For example, the probability that a train arrive on time could be such a problem. The reliability would be high if the number of arrivals on or before scheduled time is high compared to the number of late arrivals. The facility considered would be the train service, while the function is the ability to arrive on time. Other reliability functions to monitor could be the probability that there are enough seats for all passengers or the probability that the train needs maintenance during a defined period.

With this definition in mind, the term *structural reliability* applies to analysis on structures, be it free supported beams, buildings or bridges. Here, reliability is achieved if loads or load effects do not exceed the associated resistance or other defined restrictions. Moan gives a more narrow meaning of this term, which is useful also for the purposes of this study:

> [...] it is the *probability* that a structure will not attain each specified limit state [...] during a specified *reference period*. [20]

The meaning of the term limit state will be addressed in sec. 3.7.

While the term safety mainly is understood qualitatively, reliability should be possible to calculate if the necessary information is available. When calculating the reliability of a certain facility, it is necessary to do the retour by finding the *probability of failure*.

Probability of failure

It is natural that the complement of reliability is named probability of failure, as failure is the only other possible outcome. Mathematically,

$$r = 1 - p_f, \tag{3.29}$$

with reliability r and probability of failure p_f. In the example with train schedules, a failure is the event that a train arrives to late. When applied on structures, a failure occurs when a defined load effect exceeds its associated resistance.

Risk

If the consequence of failure is high, impacting for instance economy, environment or humans, the reliability of the structure should also be large. To assess the necessary size of reliability, the risk R is a useful tool. The risk takes into account the expected resulting damage $\mathrm{E}(D)$ *if* a failure occurs, and is a measure for the magnitude of a hazard. The expected damage could be expressed using monetary units, human casualties or other suitable units. The risk could be defined in various ways, but the simplest relation is provided by

$$R = p_f \cdot \mathrm{E}(D), \tag{3.30}$$

which means that R is the expected value of the "penalty" should a failure occur. Design codes take the risk into account by adjusting safety factors to the purposes of the structure.

3.6 Classification of uncertainty

The probabilistic approach acknowledges that there are statistical uncertainties connected with the variables included in a structural analysis. There are two main sources for uncertainty, [20] namely

- Inherent or fundamental uncertainty
- Imperfect or incomplete knowledge.
  - Lack of information
  - Modelling assumptions

Truly random processes and phenomena possess a fundamental uncertainty. For example, it is impossible to say what the maximal wind and snow load will be during some reference period, and the resistance of steel members varies due to variability in the manfacturing process and materials. Thus, uncertainty can be a result of both natural and man-made processes. This type of uncertainty cannot be reduced by more information or gathering of larger data samples.

Uncertainty due to insufficient or incomplete knowledge is a direct result of lack of information.

Firstly, uncertainty is linked to the amount of data available to determine the probability distribution of variables. Data is collected to build a probabilistic model of some quantity, i.e. the strength of steel members produced in a factory. After some probability distribution has been selected, the numerical parameters of the distribution must be determined. Large samples are needed to produce reliable estimates of the parameters, which then they themselves must be considered random variables. This *statistical* uncertainty arises entirely due to lack of information.

Secondly, uncertainty due to the models used to describe the mechanical behaviour of a system should be addressed. For example, material properties, loads, and the mechanism of structures are often idealised and simplified in the applied model. For example, introducing linear approximations to a nonlinear problem makes the calculated result less accurate.

3.7 Calculation of failure probability

In a probabilistic analysis, some variables are statistically distributed. Hence, it is not possible to determine *(*if) the structure fails, but it is possible to find the probability that this happens. To do this, it is practical to define limit states for the considered structure. A limit state is described as the point where load effect is in perfect balance with the resistance. It is necessary to determine one limit state for each type of failure. The limit state is defined by a limit state function G, most generally presented on the following form:

$$G(C_0, X_1, X_2, \ldots, X_n) = 0 \tag{3.31}$$

Here, C_0 is some typical constant, while $X_i, i \in \{1, \ldots, n\}$ are the variables that defines the structure in question. In the following, the vector $\mathbf{X}$ represent the variables X_i. Also, $\mathbf{X}$ is distributed with the density function $f_{\mathbf{X}}(\mathbf{x})$. We then define failure to occur when the limit state is violated, i.e. when the load effect increases beyond the resistance. Thus, the probability of failure is given by

$$p_f = P\left[G(\mathbf{X}) \leq 0\right] \tag{3.32}$$

G spans out a domain in the n-dimensional space, and p_f is found by integrating $f_{\mathbf{X}}(\mathbf{x})$ over this domain.

$$p_f = \int \dots \int_{G(\mathbf{X})\leq 0} f_{\mathbf{X}}(\mathbf{x})\,\mathrm{d}\mathbf{x} \tag{3.33}$$

In the following, some different methods to evaluate 3.33 will be investigated. Generally, this integral is not possible to evaluate analytically, however, for some special cases analytical methods through solving of the integrals are available. As long as the limit states are linear in the variables $\mathbf{X}$, and $f_{\mathbf{X}}(\mathbf{x})$ is a multi-variable normal distribution, exact values of failure probabilities can be found, even though the integral is not solved explicitly. When the problems are more complicated, numerical methods dominate. Sometimes it is possible to simplify nonlinear problems using first or second order transformations, and solve them iteratively. Such solutions demand that the probability distributions and limit states are explicitly defined, which is not always seen to be the case. When explicit distributions are not available, some form of Monte Carlo simulation methods must be employed, often combined with some other methods.

It should be noted that for many real-life application of reliability analysis, there are several limit states to take into account. As long as these limit states can be considered independently of each other, the theory presented in this chapter applies. However, when the limit states are mutually dependent, the complexity of the problem increases significantly. An example is a statically indeterminate structure. In order for such structures to collapse, the yield limit must be reached in multiple distinct points of the structure. However, when the yield limit is reached in one place, the load distribution in the rest of the structure changes, giving new limit states to assess. In terms of structural reliability, such problems are called parallell systems. It is advantageous when reliability challenges can be formulated as serial systems, for which the whole structure collapse if one limit state is reached. Here, the discussion are limited to serial systems.

To shed some light on the different evaluation methods, the basic reliability problem [19] with one simple limit state, $G(R, S) = R - S$, will be considered. S is the load effect, resisted by R alone. For example, $S = \sigma$ could be the tension in a member with yield stress limit $R = f_y$.

3.7.1 The basic reliability problem

The variables S and R are considered, statistically distributed by the joint probability distribution $f_{RS}(r, s)$. Then,

$$p_f = \int_{R-S\leq 0} \int f_{RS}(r, s)\,\mathrm{d}r\mathrm{d}s \tag{3.34}$$

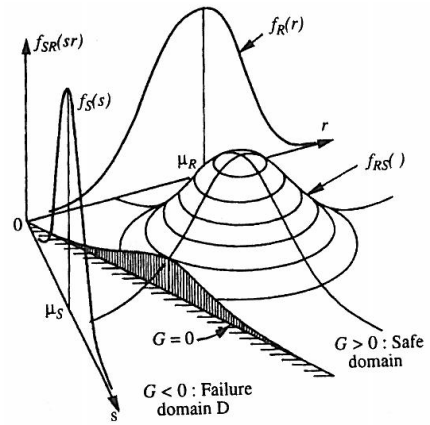

(a) Ill. of eq. (3.34)

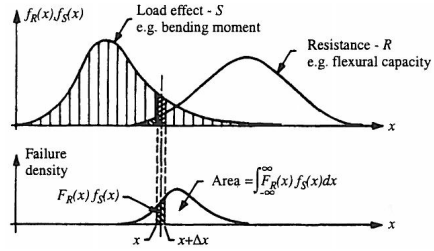

(b) Ill. of eq. (3.36)

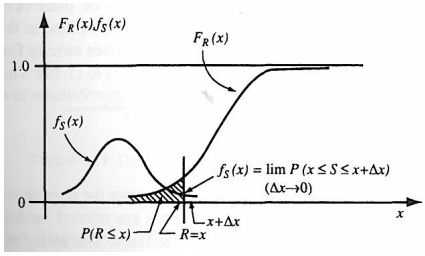

(c) Ill. of eq. (3.36)

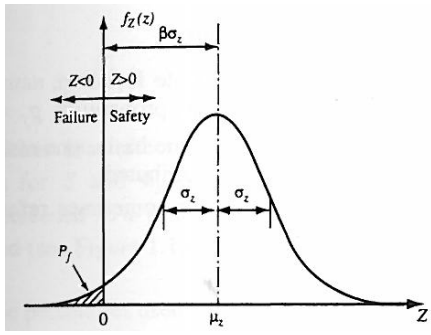

(d) Ill. of eq. (3.40)

Figure 3.4: Different ways to consider the basic reliability problem.[3]

If R and S have zero correlation, $f_{RS}(r,s) = f_R(r)f_S(s)$, and

$$p_f = \int_{-\infty}^{\infty}\int_{-\infty}^{s} f_S(s)f_R(r)\,\mathrm{d}r\,\mathrm{d}s \tag{3.35}$$

$$= \int_{-\infty}^{\infty} F_R(s)f_S(s)\,\mathrm{d}s \tag{3.36}$$

Example 1. R, S with normal distributions and mutual correlation.

When $R = N(\mu_R, \sigma_R)$ and $S = N(\mu_S, \sigma_S)$, and they are correlated with ρ_{RS}, p_f is easily found, as the single variable $M = R - S$ is distributed with $M = N(\mu_M, \sigma_M^2)$, where

$$\mu_M = \mu_R - \mu_S, \qquad \sigma_M^2 = \sigma_R^2 + \sigma_S^2 - 2\rho_{RS}\sigma_R\sigma_S \tag{3.37}$$

p_f can now be calculated as

$$p_f = P(M \leq 0) \tag{3.38}$$
$$= P(\frac{M - \mu_M}{\sigma_M} \leq -\frac{\mu_M}{\sigma_M}) \tag{3.39}$$
$$= \Phi(-\beta), \qquad \beta = \frac{\mu_M}{\sigma_M} \tag{3.40}$$

$\Phi()$ is the cumulative distribution function of the standard normal distribution, with zero mean and variance of 1. The transformation used in (3.38)-(3.39) enabled to use this function, which values can easily be found in tables or from suitable data programs. β is commonly called the safety index or the safety level of the underlying problem.

3.7.2 Hasofer-Lind method

For the simple limit state G=R-S, it was possible to reduce the problem to a single variable problem. This procedure represents a generalisation of a more general method, called the Hasofer-Lind transformation. The outline of the method for a linear limit state function depending on the n-sized correlated, normally distributed vector $\mathbf{X}$, is given below. A linear limit state function can be defined as

$$G(\mathbf{X}) = C_0 + \mathbf{B}\mathbf{X} = 0, \tag{3.41}$$

where B is a n-sized row-vector of constants. Still, we want to reduce (3.41) into a single variable problem with $M = C_0 + \mathbf{B}\mathbf{X}$. To find $\mathrm{E}(M)$ and $\mathrm{Var}(M)$ we need the following properties:

$$\mathrm{E}(M) = C_0 + \mathbf{B}\mathrm{E}\mathbf{X} \tag{3.42}$$
$$\mathrm{Var}(M) = \mathrm{Cov}(C_0 + \mathbf{B}\mathbf{X}) = \mathbf{B}\mathrm{Var}(X)\mathbf{B}^T \tag{3.43}$$

To see that this is valid, use the definition in (3.14). Again, $\beta = \mathrm{E}(M)/\sqrt{\mathrm{Var}(M)}$ can be found, and $p_f = \Phi(-\beta)$.

The strength of the procedure is that it is easily extendable to non-linear limit state functions, and even to non-normally distribution functions. When the limit states are non-linear, they can often be estimated by means of Taylor expansions, which are iteratively evaluated to find the safety index. The simplest Taylor expansion include only the first order term; in this case, the procedure is denoted a *First Order Reliability Method* (FORM). To increase accuracy, the second order term can be included, consequently applying a *SORM* method.

3.8 Monte-Carlo methods

The methods shown above all depended on limit states explicitly defined by the variables in X. An even more general procedure is provided with a numerical method, Monte-Carlo simulatons. The method makes use of the fact that

$$p_f = \lim_{N \to \infty} \frac{N_{failure}}{N} \tag{3.44}$$

(3.44) has a very clear interpretation. If the value of some limit state function were calculated for *all* possible combinations of input values, p_f would be found as the share of outcomes that violated the limit state. Obviously, N is a finite number in practical use, implying that $\hat{p}_f = N_{failure}/N_{sim}$ is an unbiased estimator of p_f. It can be shown that the variance for p_f is given by

$$\sigma_{\hat{p}_f} = \sqrt{\frac{p_f(1-p_f)}{n}} \tag{3.45}$$

An approximate $(1-\alpha)\cdot 100\%$ confidence interval for p_f can be constructed as

$$C^- \leq p_f \leq C^+, \qquad C^{\pm} = \hat{p}_f \pm z_{\alpha/2}\sigma_{\hat{p}_f}, \tag{3.46}$$

N_{sim} random vectors $\mathbf{X}$ are generated, each of them drawn with a probability that is in compliance with their probability distribution $f_{\mathbf{X}}(\mathbf{x})$. Then $G(\mathbf{x})$ are evaluated for each $\mathbf{x}$. $N_{failure}$ is the number of vectors $\mathbf{x}$ that results in $G(\mathbf{x}) \leq 0$. It is intuitive that, for a large number of simulations, approximately p_f of the simulations are failure events.

Monte Carlo analysis is strongly dependent on the computational power of modern computers. Especially for small probabilities of failure, N_{sim} must be very large to get accurate results. Also, the calculation amount needed to get the results of one single simulation can be tedious. Because the computational effort is high, and maybe because the application is straightforward, this method is sometimes called crude Monte Carlo.

An important aspect of the method is the ability to simulate vectors that "listens" to the defined distribution function.

Generation of random numbers

The method is described for a single variable with CDF $F_X(x)$.

To apply the method, computer software that contains a random number generator is needed. Such generators produces random numbers between 0 and 1. For problems of limited size, random number tables are still found in some statistical handbooks. The fact that $F_X(x)$ is a one-to-one, invertible function, which takes on the values between 0 and 1, comes in very handy.

For each random number r_i that is produced, the equation $F_X(x_i) = r_i$ should be solved to find $x_i = F_X^{-1}(r_i)$. Even if F_X is not always defined in terms of elementary functions, this number can be found by computer programs such as MATLAB for a very wide range of distribution types. The method is illustrated in fig. 3.5.

From the figure it is seen that the values of x_i centered about the mean will be generated more often than the values at the tail of the distribution, and that this fact solely depends on the slope of the CDF, which in turn is the value of the corresponding PDF.

The main limitation of the presented method rests on the fact that it is computationally expensive. To reduce the calculation effort, several modifications to the basic Monte-Carlo method are suggested. Among the most noticeable is *importance sampling*, where a suitable importance sampling function is used to attribute more weight to values in the failure domain. It is beyond the scope of this text to present the method, see [3] for a full account of the theory.

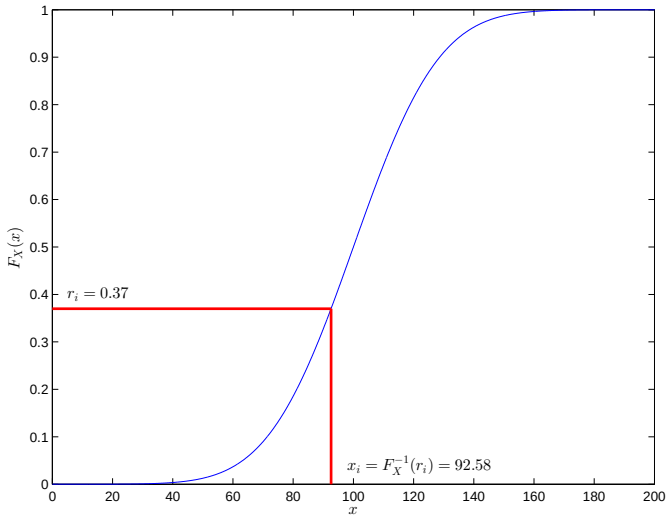

Figure 3.5: Generation of random variables. The CDF fits the normally distributed variable M of the example in sec. 3.7.1

Instead, another suggested method will be given attention. Here, p_f is estimated by extrapolating through a number of "reduced" failure probabilities, which are obtained as a result of modified limit states.

3.8.1 Enhanced Monte Carlo method

The method was presented by Arvid Næss at Department of Mathematical Sciences, NTNU.

An outline of the method, which was presented by Arvid Næss at Department of Mathematical Sciences, NTNU, is given below. As before, $p_F = P(M \leq 0)$. Now, a parameterized class of "reduced" limit states are introduced as

$$M(\lambda) = M - \mu_M(1 - \lambda), \qquad 0 \leq \lambda \leq 1 \tag{3.47}$$

It is seen that $M(1) = M$. Correspondingly, $p_f(\lambda) = P(M(\lambda) \leq 0)$ are defined. Obviously $p_f(\lambda \neq 1) > p_f$, which means that accurate estimates are obtained for fewer simulations than in the crude version.

Proceeding, Næss made the case that

$$p_f(\lambda) \approx q \cdot \exp\left\{-a\,(\lambda - b)^c\right\}, \qquad \lambda_0 \leq \lambda \leq 1 \tag{3.48}$$

The lower limit, λ_0, is introduced to justify the expression, and to increase the accuracy when $\lambda \to 1$. q, a, b, c are unknown parameters. The crucial point of the method is that it is possible to estimate these parameters, using a number of data points $(\lambda_i, p_f(\lambda_i)), \lambda_0 \leq \lambda_i < 1, i \in \{1, \ldots, m\}$. Explicitly, the parameters are found by minimizing the mean square error with respect to all four arguments on the log level, i.e. minimizing the non-linear function F

$$F(q,a,b,c) = \sum_{i=1}^{m} w_i \left(\log\hat{p}_f(\lambda_i) - \log q + a(\lambda_i - b)^c\right)^2 \tag{3.49}$$

A weighting factor w_i is introduced to emphasize more reliable data points. $w_i = \left(\log C^+(\lambda_i) - \log C^-(\lambda_i)\right)^{-2}$ is chosen in this study, but other choices can also be made. $C^{\pm}(\lambda_i)$ is defined in (3.46) with $\hat{p}_f$ replaced by $\hat{p}_f(\lambda_i)$. If $\hat{p}_f(\lambda_i) = 0$, w_i is no longer defined, which forces the minimizing procedure to stop. However, numerical errors often arise well before this point. Therefore, the upper limit λ_m must be chosen with some care. (3.49) is nonlinear, and therefore an iterative procedure must be applied. A Levenberg-Marquardt optimization method is suggested, see e.g. [21] For a more extensive presentation of the enhanced Monte Carlo method, see [22].

Example 2. $R = N(200, 10), S = N(100, 20), \rho_{RS} = \{-0.4, 0, 0.2\}$

In the following, failure probabilities for the limit state $M = R - S$ will be examined. Results both from the theoretical formulation from sec. 3.7.1, crude Monte Carlo simulations and the enhanced Monte Carlo method will be presented.

Analytical solution

Exact calculation of failure probability is straight-forward, combining (3.37) and (3.40) give the results seen in table 3.1.

ρ_{RS}	-0.4	0	0.2
β	3.893	4.472	4.880
p_f	$4.961 \cdot 10^{-5}$	$3.872 \cdot 10^{-6}$	$5.318 \cdot 10^{-7}$

Table 3.1: Safety level and failure probabilities for the basic reliability problem using different correlation values.

As expected from the formulas in (3.37), positive correlation reduces the probability of failure. For failure to happen, it is necessary that R is small while S takes on a large value. With positive correlation, this situation is less probable to happen. With negative correlation, this is more likely to occur.

Crude Monte Carlo simulations

To estimate the probability of failure, a simple MATLAB program was developed, and 10^9 simulations were performed. Table 3.2 show the results. For $\rho_{RS} \in \{-0.4, 0\}$, this gave fairly accurate results, with confidence intervals that would be acceptable for many real-life applications. The simulation with $\rho_{RS} = 0.2$ gives a value in accordance with the theoretical result, with a slightly larger confidence interval.

Enhanced Monte Carlo method

The enhanced Monte Carlo method was employed using $N_sim = 10^6$ simulations, $\frac{1}{1000}$ of the number used for crude Monte Carlo simulations. The accuracy of the results could

ρ_{RS}	-0.4	0	0.2
β	3.89	4.48	4.88
$p_f \cdot 10^7$	496.7	37.5	5.4
$CI_{95\%}$	$\pm 0.9\%$	$\pm 3.2\%$	$\pm 8.5\%$

Table 3.2: Safety levels, failure probabilities and 95 % confidence intervals calculated using $N_{sim} = 10^9$ simulations.

have been increased for larger N_{sim}. However, the results provide insight into what to expect of the enhanced method. The confidence intervals are quite wide, but since probabilities are small, the safety level is still approximated with acceptable accuracy. To assess qualitatively which accuracy to expect, one could compare the power of 10 values for N_{sim} and p_f, respectively, for example by calculating $m_{\log} = \log N_{sim} + \log p_f$. If $m_{\log} < 0$, crude Monte Carlo simulations are meaningless, because $N_f = 0$ would be the expected number of failures. On the other hand, the results of table 3.3 suggest that the enhanced method provides some accuracy even when $m_{\log} < 0$.

ρ_{RS}	-0.4	0	0.2
β	3.89	4.44	4.85
$\Delta\beta$	0.07	0.11	0.173
$p_f \cdot 10^7$	483	46	6
$CI_{95\%}$	414-555	34-56	4-9
$CI_{95\%}$ [%]	29%	50%	86%

Table 3.3: Safety levels, failure probabilities and 95 % confidence intervals calculated using the enhanced method with $N_{sim} = 10^6$ simulations.

The last row in table 3.3 shows the total width of the confidence interval compared to the estimated value of p_f. To compare with values in table 3.2, they must be divided with 2. The difference is due to the fact that confidence intervals for the enhanced method are not centered around $\hat{p}_f$. In fig. 3.6, the extrapolation technique is graphically depicted. When the extrapolation curve is linear in the log space, the problem becomes ill-defined, because there is an infinite number of pairs that solve (3.49) for q and b. To find the extrapolation curve and confidence intervals, several steps must be taken. First the reduced "failure" probabilities are found, and the confidence intervals for the chosen values are calculated. Weigthing factors can be calculated, and the extrapolation curve for p_f is calculated. Based on this curve, new confidence intervals are calculated in the range of $\lambda_0 - \lambda_M$, and lastly, the nonlinear regression model is applied to these curves as well. During this repetitive procedure, the limits of the confidence intervals often becomes approximate values, to an even larger degree than p_f is.

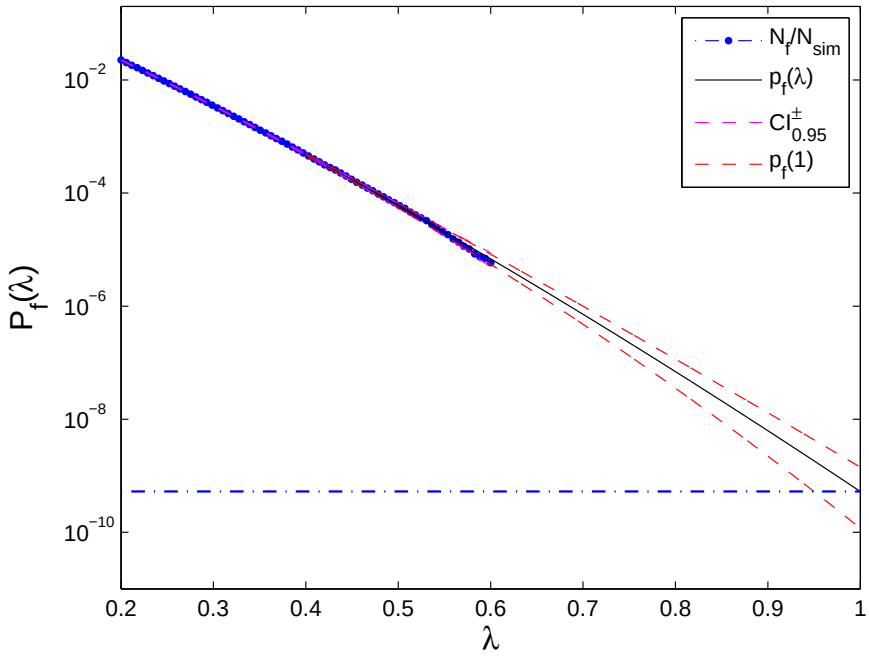

Figure 3.6: The extrapolation curve of the enhanced method. Blue dots are $\hat{p_f}(\lambda)$, black and red curves estimate failure probability and confidence limits, respectively.

Chapter 4

Uncertainties in determination of critical flutter speed

A number of factors leading to uncertainty and error sources are related to the determination of aeroelastic behaviour. For a structure subjected to wind loads, Jakobsen and Tanaka suggest a tripartite of the uncertainty sources:

1. Fundamentally, the uncertainties stem from the random nature of wind, its inborn variability.

2. Secondly, our lack of understanding of this variability, as well as of all the details of the wind load generation mechanism, including windstructure interaction, increases the uncertainty.

3. Also, simplifications introduced in the mathematical models for wind forces and structural response, streamlined for the design purposes, introduce additional uncertainty. [23]

In the following, some brief comments about 1. will be provided, while 2. and 3. considered in more depth.

4.1 The random nature of wind

At a given time and in a given position in space, it is impossible to predict the size and direction of the wind vector, and naturally, also the instantaneous wind velocity pressure is an unknown size. This means that the wind velocity fluctuations are a stochastic process, and they have to be described by their statistical properties. The random nature of the wind process can be described on two levels. Firstly, the instantaneous value of for example the vertical turbulence component is random. However, when sampling a number of events within a short term period, it is possible assess the statistical parameters which determines

the process during this short term period. Secondly, randomness stems from the fact that every one of these successive short term periods differ from each other. To some degree their statistical properties would be similar, and on some accuracy level the recording of different short term periods could look the same. However, as they are not exactly equal, the properties of these periods must also be described statistically. It is usual to record periods of 10 minutes. For example, the design rule of interest in this thesis is based on the 10 minutes mean-wind velocity that is expected to occur only once over a period of 500 years. The nature of atmospherical wind is assessed in many publications, see e.g. [17], [2].

4.2 Angle of incidence

During the formulation of self-exited forces in chap. 2, two linearisations were introduced. It was assumed that the angle of incidence is small, meaning that a linearisation of the load coefficients could be introduced. Also, nonlinear terms of the turbulence components and velocity components of the bridge was assumed to be negligible. This way, it was assumed that self-exited forces can be assessed independently of the buffeting forces from turbulence components. While practical for calculations, the simplifications lead to some inaccuracies.

When determining flutter derivatives, the mean angle of incidence are usually fixed, and the derivatives are determined in that position. This does not take into account that the balancing position of the bridge changes with the mean wind speed as well as with the charachteristics of the turbulence components. Therefore, a more accurate way to define the forces would be to update the value of derivatives so that they depended on the balancing position changes.

A variant of this problem is the fact that turbulence components change the effective angle of incidence between the bridge deck and the wind vector. As mentioned, the calculated derivatives for a bridge section are usually extracted from the balancing position. When the angle changes, the bridge section sees other derivatives than those calculated from the average position. In a full scale investigation of the Humber Bridge, which is currently the 7th longest suspension bridge in the world, built with a main span of 1410m, wind speed fluctuations in the vertical plane peaking at $\pm 10^{\circ}$ were recorded [24], suggesting that significant deviation from the mean flutter values could be observed. The angle of incidence has contributions from both bridge deck motion and vertical turbulence fluctuations, and under certain circumstances it is seen that the latter contribution outweighs the first. In an attempt to assess the effect of varying turbulence intensity upon *torsional* flutter stability, Diana found significant differences in acceleration response. To take into account the angle of incidence, a modified version of the quasi static theory was used [4]. Fig. 4.1 shows compliance between results obtained when sections were subjected to laminar flow and flow with low turbulence intensity, respectively. However, the results for high turbulence intensity differed significantly. Moreover, it is observed that the results for two different cross sections were ambiguous.

For the box shaped section subjected to low turbulence or laminar flow, a violent increase in amplitudes at the point of instability was observed. Subjected to high turbulence, amplitudes increased gradually, even beyond the instability limit seen with laminar flow.

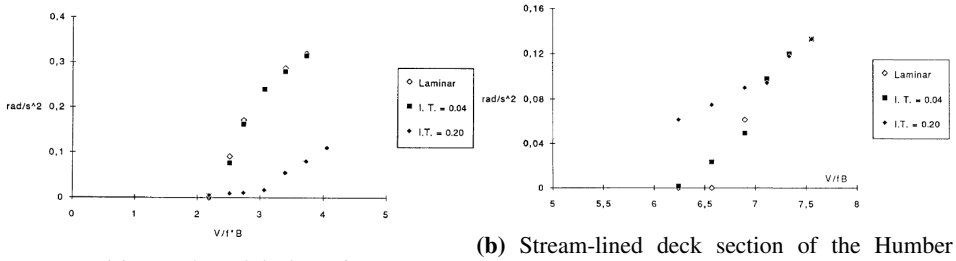

(a) Box shaped deck section

(b) Stream-lined deck section of the Humber Bridge

Figure 4.1: Numerical simulation of torsional acceleration due to laminar flow and turbulence intensities 0.04 and 0.20, respectively. Response is calculated with root mean square method.[4]

For the Humber bridge section, low turbulence and laminar flow resulted in rapid amplitude increase around the flutter limit. No sudden increase was observed in the case of high turbulence, making it hard to decide the critical speed for this configuration.

While the response behaviour of the sections in the above two cases in no sense can be viewed as general, they do suggest that the level of turbulence, especially at high levels, is able to affect the aeroelastic stability of suspension bridges.

4.3 Lack of spatial coherence

To define the multimode flutter criteria, mode shapes of the whole bridge must be taken into account. Thus, the experimentally determined aerodynamic stiffness and damping matrices are integrated along the bridge with the mode shapes taken into account. Normally, it is taken for granted that the derivative matrices are constant along the whole span of the bridge. This involves two main simplifications.

The first assumption is that the mean wind speed is constant along the whole bridge. This is not always accurate. For the Hardanger Bridge, the heigth of the girder changes from 52 m under the pylons, to 63.5 m at the midpoint of the span. Using the calculation procedure from [25], this leads to a difference in mean wind velocity of approx. 8 %. Likewise, the mean wind speed depend on the horizontal distance from the coastline, meaning that the total difference of mean speed between the middle of the fjord and at the pylons, is possibly even larger than 8 %.

If a construction or a natural obstacle hinder a free path for the wind towards parts of the bridge, the assumption of $L_{exp} = L$ could lead to inaccuracies. In the case of the Hardanger Bridge, however, this is not a problem.

The second assumption is that the turbulence components are perfectly correlated along the span-wise direction of the bridge. Generally, this is not the case. Several studies have been performed to examine the consequences of this simplification. It has been indicated that this lack of coherence justifies an increase of the critical speed limit. More specifically, bridges subjected to turbulent wind, experiences increased amplitudes at subcritical speed, but the flutter limit is shifted towards higher values. This effect has been observed both by full model wind tunnel testing and analysis (see e.g. [4], [5], [26]). The

trend is illustrated by means of fig. 4.2.

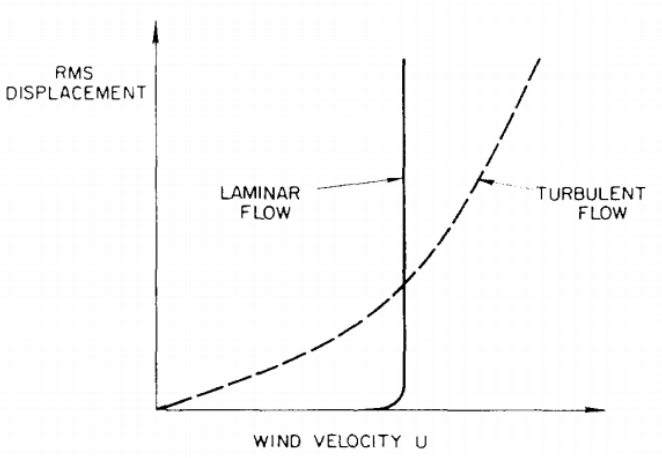

Figure 4.2: Displacement trends of bridge decks subjected to laminar and turbulent flow, respectively. [5]

Here, the same trend as in fig. 4.1 are observed. However, the approach to reach this conclusion differ. While Diana calculated a shift in the flutter speed limit due to the effect of angular differences, Scanlan uses fig. 4.2 to point out the effect of lack of spatial coherence.

4.4 Experimental determination of flutter derivatives

One of the basic assumptions of Scanlans approach, is that aerodynamical derivatives can be experimentally determined using wind tunnel testing. The accuracy of which self-exited forces are modelled thus depend strongly on the accuracy of the wind tunnel testing.

Sec. 4.2 and 4.3 suggest that turbulence effects should be taken into account when wind tunnel testing is performed. Indeed, it is generally accepted that wind tunnel flows should replicate the characteristics of atmospherical wind [17]. Today, it is possible to control turbulence intensity and other characteristics of wind in common test tunnels to a certain degree. However, this is only one of the challenges arising when downscaled models are tested. To obtain physical similitude between model and full scale structure, several similarity criteria have to be satisfied. Generally, it is observed that all of these criteria cannot be met, and some compromising is necessary. It is beyond the scope of this text to dive into the extensive theory of similarity requirements. However, two basic considerations are mentioned here.

The dimensional ratio between the full scale structure and the section model, should be replicated by the ratio of some typical lengths of turbulence eddies in the longitudinal wind direction, also measured in reality and in the wind tunnel. Here the typical length of turbulence components must be understood in an average sense. If the integral scale of turbulence components are adopted, such typical lengths are found to be between 100-

500 m at 60 m elevation [17]. Using a scaling of 1:50, it can sometimes be difficult to replcate suffiently long integral scales in wind tunnels, meaning that the turbulence similitude demand is violated.

To replicate the full scale structure, the section model should be tuned so that the ratio between the most important frequencies of the bridge are similar. Basically, the section model is a stiff beam suspended in a set of springs. If motion in all directions is allowed, the model have three degrees of freedom. This makes it possible to replicate three frequencies, one in each direction. In the early stage of analysis, it can be difficult to assess which frequencies that should be replicated.

Chapter 5

Modelling of aerodynamical derivatives

5.1 Risk reliability analysis on bridges

For bridge projects of wind class III, the design codes specify that $V_{Cr} \geq 1.6V_{S,500}$, where $V_{S,500}$ is the 10-min mean velocity wind expected to return every 500 years. By experience, the safety level this limitation provides is large. However, quantitative information about the reliability levels associated with this design rule, are as of today very limited.

The chosen safety level is reasonable for a number of reasons. Firstly, the resulting consequences of a bridge reaching critical speed are fatal. Secondly, the random nature of wind makes calculations uncertain. Thirdly, all modelling uncertainties are not fully understood.

In the present study, probability of failure is defined by $p_f = P(V_{Cr} - V_S \leq 0)$. In this context, V_S is represented by a probability distribution for the extreme 10-min mean wind velocity expected to occur during one year. V_{Cr} is the critical speed obtained by solving (2.22). V_{Cr} is a random variable because the parameters that contribute to the equation are random. If the exact distribution function of all variables contributing to (2.22) were known, the distribution of V_{Cr} could be estimated very accurately. For practical reasons, this is neither possible nor necessary. By performing a sensitivity analysis on the deterministic problem, it would be possible to find which variables that contribute the most to the variance of V_{Cr}.

Making a case study of the Messina Straits Bridge, Argentini et. al. found that the flutter derivatives $A_i^*, i \in \{1, 4\}$ and $H_i, i \in \{1, 3\}$, as well as the natural frequencies of 1st symmetrical torsional and vertical mode, had a large impact on variance[27]. Cheng found that still air material properties, i.e. mass, material stiffness, and geometry, were of minor importance[28]. Also, an assessment of the Hålogaland Bridge suggested that uncertainty of modal damping ratios were of minor importance compared to that of flutter derivatives [16]. The methods they used differ considerably, and the results cannot be

viewed as general.

In the present study, it is chosen to focus solely on the flutter derivatives, while fixing all the other variables. Thus, the reliability problem consists of 19 independent variables, namely the flutter derivatives $P_i^*, H_i^*, A_i^*, i \in \{1, 2, ..., 6\}$, as well as the extreme value of wind speed, V_S. If the formulation seen in 3.31 is applied, the problem can be defined as

$$p_f = P\left[G(P_i^*, H_i^*, A_i^*, V_S) \leq 0\right], \qquad i \in \{1, 2, \ldots, 6\} \tag{5.1}$$

Here, the flutter derivatives must be viewed as mutually correlated variables, while V_S is treated independently of the critical speed problem. Since G does not have a closed-form solution, it is chosen to use the enhanced Monte Carlo method presented in 3.8.1. However, before Monte Carlo methods can be applied, there are several questions that must be answered. In this chapter, solutions to the following "problems" are suggested:

Extraction of eigenmodes to include in the eigenvalue problem To solve the equation that defines flutter, it is necessary to determine which eigenmodes to include. Eigenmodes are normally found through use of a FEM-model. In sec. 5.2, some characteristics of the provided solutions are presented.

Modeling of flutter variables The flutter derivatives are determined experimentally using a section test. The test campaign provides information about flutter derivatives at discrete points. To implement the variables in a routine to find critical speed, it is necessary to model the derivatives as continuous functions. The inherent uncertainty of wind dynamics, as well as the applied methods, implies that there is significant variance to take into account when modelling. Two different solutions on howto take this into account are suggested in sec 5.4.

Implementation of a routine to solve the eigenvalue problem To solve the eigenvalue problem defined in (2.22), data implementation employing an iterative technique is necessary. In sec. 5.5, a description of the routine used to solve the problem is given.

Determination of wind field V_{Cr} represents the "resistance" part of the reliability problem. Obviously, it is also necessary to define the load effect of the problem. The calculations providing a probability distribution describing the wind field at the construction site are given in 5.6.

5.2 FEM-analysis of the bridge

To get a starting point for analysis, it is necessary to calculate the eigenmodes and eigenfrequencies of the bridge. These models give undamped frequencies and modes in a steady environment, (in-wind effects are not included). Finite element method (FEM) modelling is the dominating approach to achieve this information. The Hardanger Bridge has been subject to several calculations. In [8], an ALVSAT model of the bridge girder was used to extract the eigenmodes and eigenfrequencies. For the purposes of this thesis, an ABAQUS model provided by The Norwegian Public Road Administration has been used. A FEM model of the Hardanger Bridge is shown in 5.1. While the ALVSAT model provided very

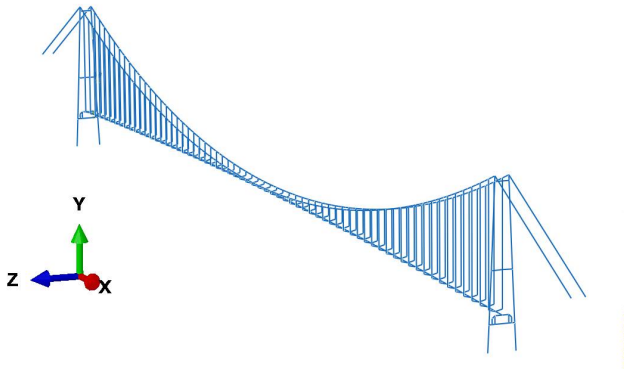

Figure 5.1: ABAQUS model of the Hardanger Bridge.

”clean” mode shapes, the eigenmodes from ABAQUS include pure tower/cable modes, as well as modes with motion where all the different parts of the bridge are excited.

Because the purpose of this text is to perform a reliability analysis including small values of probability, accurate results regarding the multi mode flutter calculations were important, and therefore more modes than usual were considered. Among the first 50 natural eigenmodes, 32 were found to partially or fully excite the bridge deck. 14 of them were horizontal modes, 14 were vertical eigenmodes, 3 were pure torsional modes, and one mode combined significant deflections in torsional *and* horizontal direction.

For all modes, the damping ratios are chosen as $\zeta_{0,n} = 0.005$. This is not necessarily accurate, but since the purposes of the study is to assess the effect stochastic flutter derivatives, it is probably an approximation accurate enough. The numbering seen in table 5.1 will be used in the remaining part of this thesis.

5.3 Results from section test

The test data used in this thesis has been extracted from wind tunnel testing on a section model at Svend Ole Hansen ApS, a Danish wind engineering company, on behalf of the Norwegian Public Roads Administration (SVV). The testing was performed on a 1:50 section model, the length being 1.7m.

The section is calibrated to imitate the behaviour of the Hardanger Bridge, based on information received from SVV regarding geometry, mass, mass of moment inertia and natural frequencies. The test results include information regarding static load coefficients, critical flutter speed, flutter derivatives, admittance functions and vortex induced vibrations. The flutter derivatives are of special interest; however, also a brief comparison with quasi-static load coefficients are provided.

Traditionally, vertical and torsional motions have been included in bridge section testing, which makes it possible to find the 8 derivatives $H_i^*, A_i^*, i \in \{1, 2, 3, 4\}$. In 2006, the first tests of the Hardanger Bridge model were performed this way. However, in 2007 the section model of the Hardanger Bridge was designed with the possibility to include

Mode no.	Nat. frequency	Direction	Mode shape.	Equ. mass
1	0.314	H	S	12020
2	0.615	H	A	9865
3	0.693	V	A	13298
4	0.883	V	S	12953
5	1.061	H	S	10065
6	1.239	V	S	12951
7	1.325	V	A	13061
10	1.467	H	A	64509*
11	1.536	H	S	59757*
12	1.711	V	S	12961
13	1.840	H	A	10451
14	2.068	V	A	12918
15	2.260	T	S	481161
17	2.463	H	S	41194*
18	2.475	V	S	12867
19	2.550	H	A	113069
21	2.717	H	S	13251
22	2.895	V	A	12925
23	3.123	H	S	93314*
24	3.165	H	A	190664*
26	3.289	T	A	485880
27	3.327	V	S	16144
28	3.479	V	S	47802*
29	3.480	H	S	68338*
31	3.670	H	A	59626*
33	3.853	V	A	13174
34	4.004	H	A	10973
36	4.246	H	S	276563*
43	4.348	V	S	15263
46	4.553	V	S	52525*
49	4.923	T	S	491445
50	4.956	V	A	13123
58	6.329	T	A	573094

Table 5.1: Eigenmodes that exited the bridge girder. Mode numbering, still-air eigenfrequencies, motion characteristics and equivalent mass are provided. H - Horizontal, V - Vertical, T - Torsional *: These modes have significant deflections in more than one part of the bridge, making the equivalent mass calculation unvalid.

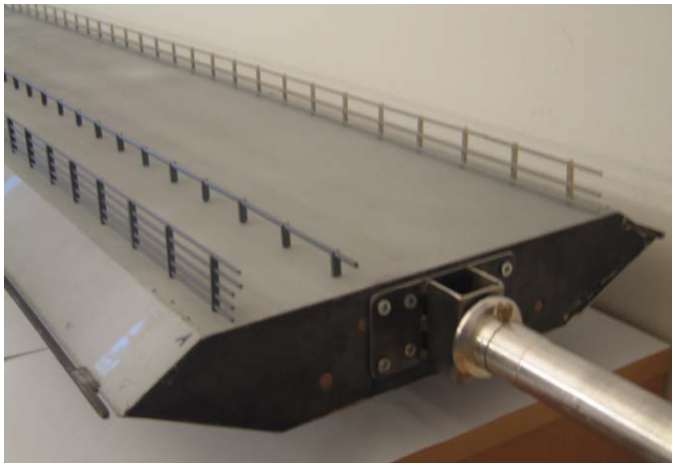

Figure 5.2: Part of the section model with railings and girders [6].

horizontal motion, making it possible to calculate all the 18 flutter derivatives. Altogether, three test series including horizontal degree of freedom have been performed.

Test series	Response components	$\frac{\omega_\phi}{\omega_z}$	$\frac{\omega_\phi}{\omega_y}$
FL10	V+H+T	2.53	1.40
FL13	V+H+T	4.71	2.55
FL15	H+T	-	1.53

Table 5.2: Test series including horizontal degree of freedom. The tests are performed with angle of incidence 0° and walking path upstream.

Test Series FL15 was excluded because it does not comprise vertical degree of freedom. The remaining two test series differed by the tuning of natural frequencies. In FL10 the relationship between the natural frequencies of the fundamental vertical mode and the torsion mode were comparable with reality. According to the ABAQUS model in sec. 5.2, $\gamma_{z\phi} = 2.26/0.88 = 2.56$, while the section model had $\gamma_{z\phi} = 2.53$. The ratio between the horizontal and torsional natural frequencies of the model was 1.40, which is consistent with the ratio between the 3rd symmetrical horizontal mode (mode 11) and the 1st torsional mode (mode 15). Test Series FL13 was calibrated to a situation where the ratios between the natural frequencies are larger, and is not as relevant for the purposes of this study. For that reason, FL10 was selected to provide data for the study. Measurement series for flutter derivatives was performed for wind speeds between 1.86 m/s and 6.3 m/s in the wind tunnel, a total of 28 registrations were made for different speeds. Some of the measuring points were considered to be less reliable than the remaining values. This was the values associated with high wind speeds, where the motion measured with a frequency near the vertical natural frequency was damped heavily. These values were therefore omitted from the subsequent modelling. The measurements are shown in fig. 5.3 and 5.4.

Extra caution should be given to the flutter derivatives associated with horizontal mo-

tion. The reason for this is that the reduced wind velocity in the tunnel for the horizontal degree of freedom is related to the eigenfrequency of the third symmetric horizontal mode. This frequency is about 5 times higher than the natural frequency of the first horizontal mode, which means that the reduced velocity associated with the first horizontal mode is multiplied with 5, far beyond the experimental data boundaries. In addition, it is expected that the interaction between the wind and the bridge at such high speeds can be approximated as static (the reduced frequency becomes very low). For this reason it is recommended in the test report that the relevant flutter derivatives are replaced with values from the quasi-static analysis, see (2.27). The quasistatic curves are added in fig. 5.3 and 5.4.

5.4 Modelling mean response of flutter derivatives

To enable use of the iterative procedure shown in fig. 5.8, it is necessary that the flutter derivatives are modelled as continuous curves depending on the reduced velocity V_{red}. To do this, a suitable polynomial trend line can be fitted to the scattered values from the test campaign. The polynomial should reproduce the general development of the measured derivatives, and does not need to reproduce all the fluctuations seen in the scatter. This implies that a polynomial of relatively low order is sufficient. The best fitted polynomials can be found by means of a least square method, which means that they can be found trough a linear regression model.

How the polynomial is constructed depends on several considerations. Should the calculation of the trend line be in good agreement with the flutter measurements within the tested range of reduced velocities only, or should reasonable behaviour outside the test area also be ascribed significance? Especially, should the fact that no aerodynamic effects exists in still-air, be reflected by the trend lines? In that case, a constraint giving $\mathbf{C}_{ae}(V=0) = \mathbf{K}_{ae}(V=0) = 0$ should be forced upon the curves.

In 2, the quasi-static formulation of self-exited forces was compared with Scanlan's approach. It was seen that the flutter derivatives of the aerodynamic damping matrix were linear functions of V_{red}, while the derivatives of K_{ae} had a quadratic variation with V_{red}. Should the polynomial try to reproduce this theoretical behaviour, or should only the observed behaviour be given emphasis?

In this study, two different sets of trend lines are suggested.

Case 1

Linear polynomials are fitted through the flutter derivatives of $\mathbf{K}_{ae}$, while second order polynomials are fitted through the flutter derivatives of $\mathbf{C}_{ae}$. Also, it is demanded that the polynomials pass through $(0,0)$, which is in line with the physical reality. The regression model of (3.24) becomes

$$\begin{aligned} X_i^* &= b_{1i} V_{red} + e_{X_i}(V_{red}), && i \in \{1,2,5\}, \\ X_i^* &= b_{1i} V_{red} + b_{2i} V_{red}^2 + e_{X_i}(V_{red}), && i \in \{3,4,6\} \end{aligned} \tag{5.2}$$

with $X \in \{P, H, A\}$, and where the lack of constant terms b_{0i} implies that $X_i^*(0) = 0$ must be satisfied. The distribution and modelling of error terms e_i will be addressed in sec. 5.4.1. In MATLAB, several tools are available to solve these kinds of regression problems. For case 1, the construction of polynomials was performed using the built-in MATLAB function polyfit.m with a slight modification, which enabled to assign each data point a weight, making it possible to force the polynomials through origo. These trend lines are displayed with blue colour in fig. 5.3-5.4.

Case 2

Second order polynomials are fitted for all flutter derivatives, without giving any concern to the behaviour of the derivatives for reduced velocities outside those of the test campaign. Thus the 18 regression models for the flutter derivatives become

$$\begin{aligned} X_i^* &= b_{0i} + b_{1i} V_{red} + b_{2i} V_{red}^2 + e_{X_i}(V_{red}) \\ i &\in \{1, 2, \ldots, 6\}, \qquad X \in \{P, H, A\} \end{aligned} \tag{5.3}$$

The regression for case 2 was performed using mvregress.m, which also made variance estimates readily available. These trend lines are displayed with black colour in fig. 5.3-5.4.

In general, the two sets of polynomials are in good compliance, at least in the range of tested reduced velocities. The most considerable differences are seen for flutter derivatives A_5^* and H_5^*. The quasi-static, linear approximations for horizontal-related motion also show some compliance with the fitted lines. In this particular test campaign of quasi-static load coefficients, C_D' was equal to zero. This gave a zero value of P_3^*, which deviates significantly from the fitted polnomial curves. Based on the relatively good coherence between quasi-static load coefficients and horizontal flutter derivatives, it was concluded that it is in the order to use the derivatives in the modelling.

5.4.1 Modelling uncertainty of flutter derivatives

As seen from fig. 5.3-5.4, the quality of the fit varies between the different flutter derivatives. For some values, e.g. P_3^*, H_3^* and A_3^*, the polynomial curve adapts well to the measured values, while the uncertainty linked to the regression analysis of e.g. A_5^* and H_4^* is larger. In order to perform a probabilistic analysis of the critical velocity, an accurate description of the uncertainty of flutter derivatives is essential. In this study two different models were proposed:

- Case 1: Using the uncertainty of the residual term, ie constructing curves based on variance of a predicted response.
- Case 2: Using the uncertainty of the coefficients, ie constructing curves based on variance of the mean response.

The two models had widely different implications, as described in chap. 6, 7. In the following, the modelling assumptions for each case are described.

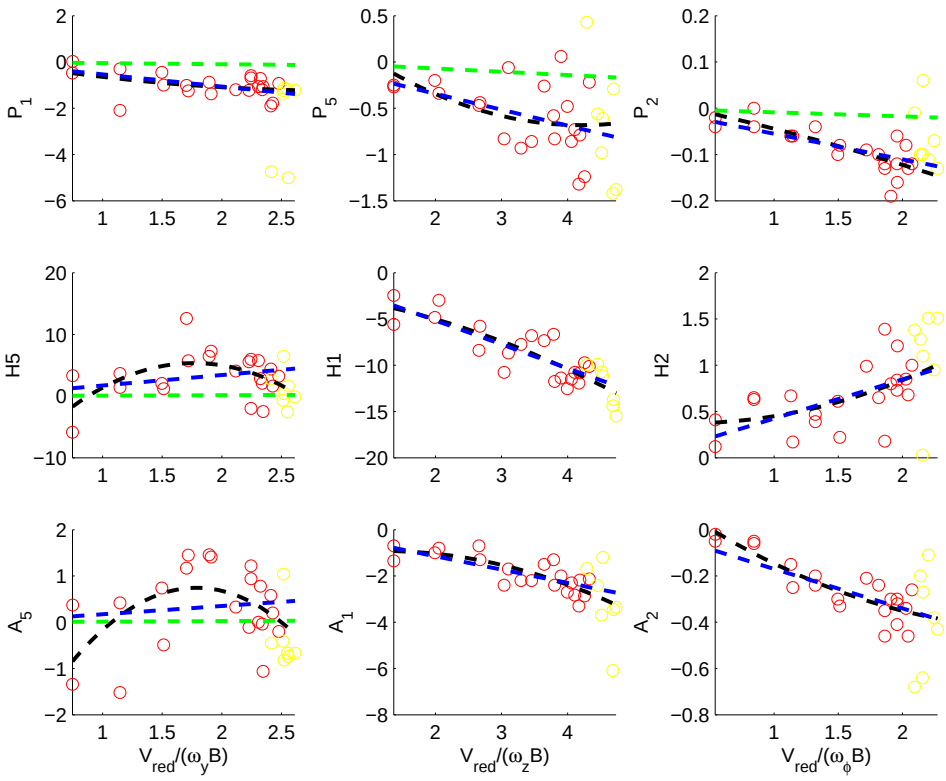

Figure 5.3: Measurements, mean trend lines and quasi-static load coefficients for damping related flutter derivatives [6].

Modelling of uncertainty: Case 1

In sec. 3.2, some key values describing the variance of linear regression were derived. A basic assumption was that the error terms, or rather the residuals, of the model were homogenously distributed with constant variance and zero mean. For the present measurements of flutter derivatives, this was seen to be inaccurate. To investigate further, residual plots were made for each $e_{X_i} = X_i^* - \hat{X}_i^*$. For 15 of the 18 derivatives, the hypothesis that the residuals were distributed by a normal distribution could not be rejected to a 5% significance level. For some of the derivatives, the assumption of variance homogenously distributed for all values of V_{red}, also seemed to be fulfilled. However, it was also observed that the absolute value of some of the residuals increased with increasing reduced velocity. It was in no sense possible to decide that this behaviour was inherent in the measurements; however, this observation suggested that residuals behave in accordance with the assumed model of mean response. In other words, it was suggested that

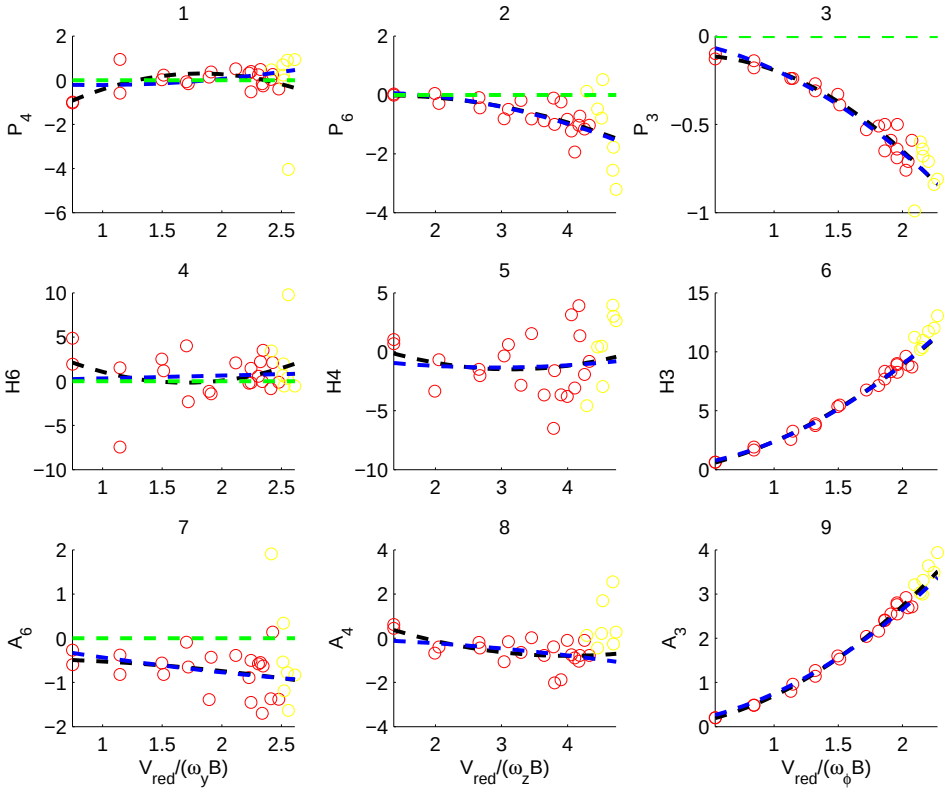

Figure 5.4: Measurements, mean trend lines and quasi-static load coefficients for stiffness related flutter derivatives [6].

$$\begin{aligned} \sigma_{e_{X_i}} &\propto V_{red}, \qquad i \in \{1, 2, 5\} \\ \sigma_{e_{X_i}} &\propto V_{red}^2, \qquad i \in \{3, 4, 6\} \end{aligned} \tag{5.4}$$

If the assumptions of (5.4) were true, scaled residual terms e_{X_i} with $K = 1/V_{red}$ and $K^2 = 1/V_{red}^2$, respectively, would be homogenously distributed throughout the range of V_{red}. Plots of these scaled residuals, denoted ε_{X_i} in the following, were made to assess whether they could be used for modeling instead of the unscaled terms. The assumption that ε_{X_i} was normally distributed, was rejected on a 5% significance level for 7 of 18 derivatives, slihgtly worse than the unscaled residuals. However, it was seen that poor performance mostly was related to the measurements with low value of V_{red}. These values are not seen to be relevant at flutter speed (see chap. 6). If the first 4 measurements were omitted, only 1 of 18 the distributions were rejected. More notably, around the reduced velocities of flutter, ε_{X_i} was somewhat more homogenously distributed than e_{X_i}, based

on ”the evidences of a visual test.” Therefore, it was decided to use the values of ε_{X_i} to construct a distribution to fit the residuals. Fig. 5.5 illustrates the modelling of a flutter derivative that behaves in accordance with the assumption of (5.4), while fig. 5.6 shows a flutter derivative with a lesser fit to the assumption.

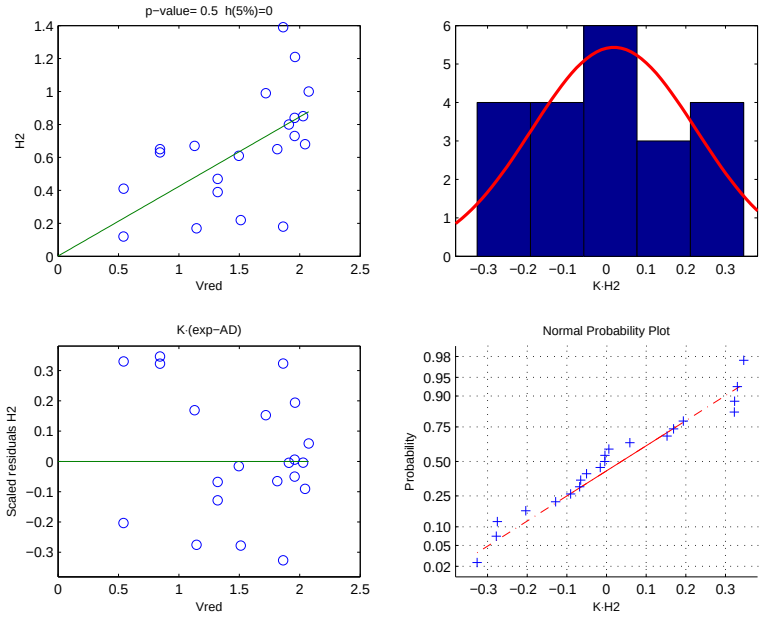

Figure 5.5: Plots of scaled residuals of flutter derivative H_2^*. The measurements fit well to the assumptions in eq. (5.4).

The covariance between residuals of different flutter derivatives also should be taken into account in the uncertainty modelling. A covariance matrix was constructed in accordance to the methods of (3.10) and (3.14), where the covariance between scaled residuals, $\sigma_{\varepsilon_{X_i}\varepsilon_{X_j}}$, were found. Also here some considerations should be made. To study the nature of covariance between derivatives, scatter plots combining the residual vectors with each other were made. At some occations, single outliers affected the correlation value significantly, giving an artificial high correlation value between two vectors. In the early stage of the modelling procedures, some attempts were made to reduce these values to produce a more correct covariance matrix. However, this yielded the matrix ill-defined, and it was finally determined to proceed with the covariance matrix based on all the residual values. The covariance matrix is shown in table B.4, while the means of the residual plots are provided in table B.3.

Modelling of uncertainty: Case 2

For case 2, where the response curves of all flutter derivatives were modelled by 2nd order polynomials, it was suggested to use the variance of the mean response of the flutter derivatives to predict uncertainty. While the uncertainty modelling of case 1 was performed by

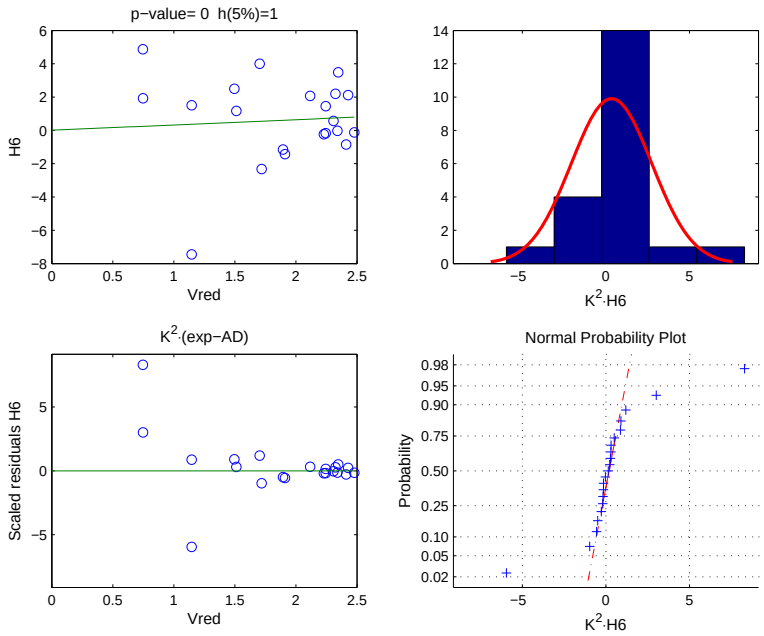

Figure 5.6: Plots of scaled residuals of flutter derivative H_6^*. The measurements fit poorly to the assumptions in eq. (5.4).

establishing sensible covariance and mean matrices of scaled residuals, the aim of the approach in case 2 was to establish the covariance matrix of the coefficients. For a single variable, the variance could be found according to the results of (3.19). For multi variable models, covariance should also be found, increasing the complexity. Not assessing the different consequences for calculations of critical speed, the approach of mean response had some technical advantages.

1. Possibly non-homogenous behaviour of residuals is taken directly into account by the variance of the coefficients. For example, increasing variance of error with reduced speed could suggest that the 2nd order term should be modelled with a relatively larger variance than the constant term.

2. The mean response is less affected by the presence of possible outliers than the models of residuals are.

In sum, this implies that a standard multi variable regression model would be capable of predicting the variance of mean response satisfyingly. The function mvregress.m is advantageous because the covariance between coefficients from different regression models is easily extracted.

For clarity, the definition of the two cases are repeated below.

5.4.2 Definition of case 1 and case 2

- **Case 1**
  - The continuous regression curves of the flutter derivatives are forced through origo to reflect aerodynamic behaviour in still-air.
  - Derivatives relevant for damping are modelled as linear, while stiffness derivatives are modelled as 2nd order polynomials.
  - The uncertainty modelling is based on the variance of *scaled* residuals.
- **Case 2**
  - Behaviour of modelling curves outside the velocity range of the test campaign are not given emphasis.
  - All derivatives are modelled as 2nd order polynomials.
  - The uncertainty modelling is based on the variance of the *mean* response.

5.5 Calculation of critical speed

A deterministic analysis of critical speed is performed by using the curves of mean response, while neglecting the variance. In the probabilistic assessment it is necessary to perform a large number of simulations to find critical speed, using the whole spectre of possible "flutter curves". The frequency of which a certain combination of flutter curves is used should be in accordance with the covariance and mean value matrices defined in sec. 5.4.1. Since it is assumed that the multi variable variance is normally distributed, a number of random dependent vectors can easily be generated, in accordance to the outline from sec. 3.8. For case 2, this method would generate the coefficients of each polynomial curve, which could then be directly implemented in an iterative technique to solve (2.22). For case 1, an extra step is needed to achieve the correct distribution of polynomial curves. The generated vectors provide the values of scaled residuals. These values should then be multiplied with either V_{red} or V_{red}^2, and added to the curves of mean response.

Each of the generated vectors thus provides a set of polynomial curves of flutter derivatives, making it possible to find critical speed by performing deterministic simulations for each set of curves.

Solving the eigenvalue problem in (2.22) must be done by an iterative procedure. For convenience, the equation is repeated here.

$$\left(\lambda_n^2\tilde{\mathbf{M}}_{\mathbf{0}} + \lambda_n\left(\tilde{\mathbf{C}}_{\mathbf{0}} - \tilde{\mathbf{C}}_{ae}\left(V,\omega\right)\right) + \left(\tilde{\mathbf{K}}_{\mathbf{0}} - \tilde{\mathbf{K}}_{ae}\left(V,\omega\right)\right)\right)\hat{\boldsymbol{\eta}} = 0, n \in \{1,\ldots,2N_{mod}\} \tag{2.22}$$

The matrices $\tilde{\mathbf{C}}_{ae}, \tilde{\mathbf{K}}_{ae}$ are nonlinear in V and ω, or rather in V_{red}, at the same time ω is contained in the eigenvalues λ_n. Therefore the solution technique needs iterations both on ω and V. Fig. 5.8 describes a routine that is in common use today. Initially, which modes to include are determined, and still-air constructional properties are defined, so as $\tilde{\mathbf{M}}_{\mathbf{0}}, \tilde{\mathbf{C}}_{\mathbf{0}}$ and $\tilde{\mathbf{K}}_{\mathbf{0}}$. Also, tolerance limits and maximal number of iterations for each loop

are defined. The tolerance limits guarantee that the obtained solutions are obtained with satisfying accuracy with respect to frequency, critical speed and damping. Because certain combinations of flutter curves can cause the iterations to diverge, the routine should be stopped after a reasonable number of iterations.

An initial value of V is defined, and for each mode, the belonging complex eigenvalue solution is established, thus providing the in-wind eigen-frequency for each mode. If the real term of one of the eigenvalues is within tolerance limit to zero, flutter is reached. If not, the value of V is increased with dV, and the procedure is repeated. Usually, at some point it is seen that the damping term of some eigenvalue increases beyond zero, giving a value of V that is higher than critical speed. When this happens, the procedure rejects the value of V, and perform another iteration with reduced velocity increment.

In addition to the outline above, which is in accordance with routine descriptions from literature, a slight improvement was suggested. Because it was seen that only a very limited number of modes were able to reach zero damping, the routine was changed, limiting the iteration to these modes only. The alteration reduced the computational effort significantly. For case 2, a solution was rejected if the value of V_{red} was outside the values from the test campaign. Here, the limit was set at $V_{red} = 4$. This did not have any practical consequence, as no simulations exceeded that value. Visually, the development of the routine is seen in fig. 5.7.

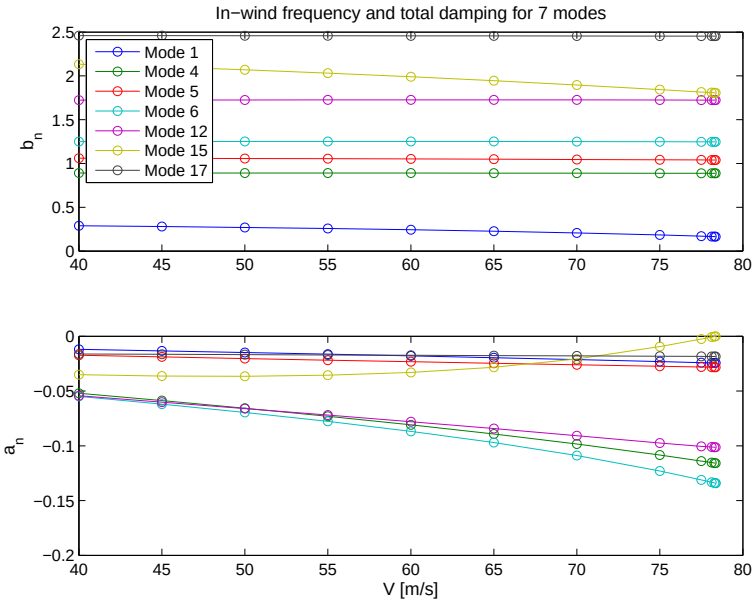

Figure 5.7: The development of an eigenvalue solution for a situation with 7 modes included. Flutter is reached when 1st torsional mode has zero damping. $dV = 5$ initially, but velocity steps are halved successively close to flutter speed.

In the figure, the upper plot represent frequency values, while the lower plot gives in-wind damping ratio. For each velocity step, stable damping ratios and frequency values

were found for each eigenmode. If none of the damping values were zero, the velocity was increased, and new values were found. The solution was found when one of curves in the lower plot reached zero. Notably, the frequency of the 1st torsional mode dropped at increasing wind speeds.

5.6 Determination of the wind field

According to Handbook 185 by the Norwegian Public Road Administration, the wind load on the Hardanger Bridge should be modelled accordingly to Wind load class III, because the bridge satisfies the following two conditions:

$$T_{min} \geq 2\,\mathrm{s}, \qquad L \geq 300\,\mathrm{m}, \tag{5.5}$$

where T_{min} is the minimal period of oscillation, and L is the length of the bridge. Wind load class III applies to bridges where significant dynamical interactions between wind load and bridge can be expected, and the design rules demand thorough investigations to ensure that instability is not reached. The design rules demand i.a.:

$$\frac{V_{Cr}}{\gamma_{Cr}} \geq V_S(z = z_m, T = 600\mathrm{s}, R = 500\mathrm{y}), \tag{5.6}$$

where V_{Cr} is the calculated critical flutter speed of the bridge, $\gamma_{Cr} = 1.6$ is a safety factor, while V_S is the mean wind component at the construction site that the bridge should be designed to withstand. It is assumed that V_S attacks the bridge normal to the main axis of the bridge. V_S is defined as the highest mean wind speed, averaged over a period T, expected to take place during a design period $R = \frac{1}{p}$, where p is the probability that V_S is the most extreme wind speed during one year. $T = 600\mathrm{s}$ is the standard averaging time, while $R = 500\,\mathrm{years}$ is the design period for instability calculations. $z = z_m$ is a reference position for calculation of critical wind speed, for example the shear center of the bridge girder in its highest position. [29]

V_S is calculated according to technical standard NS-EN-1991-1-4 [25], which specify that

$$V_S(z, T = 600\mathrm{s}, R) = c_r(z) \cdot c_o(z) \cdot c_{prob}(R) \cdot c_{dir} \cdot c_{season} \cdot v_{b,0} \tag{5.7}$$

where

$c_r(z)$	is the roughness factor
$c_o(z)$	is the topography factor, taken as 1.0
$c_{prob}(R)$	is the probability factor
c_{dir}	is the directional factor, taken as 1.0
$c_{season}(z)$	is the season factor, taken as 1.0
$v_{b,0}$	is the fundamental value of the basic wind velocity

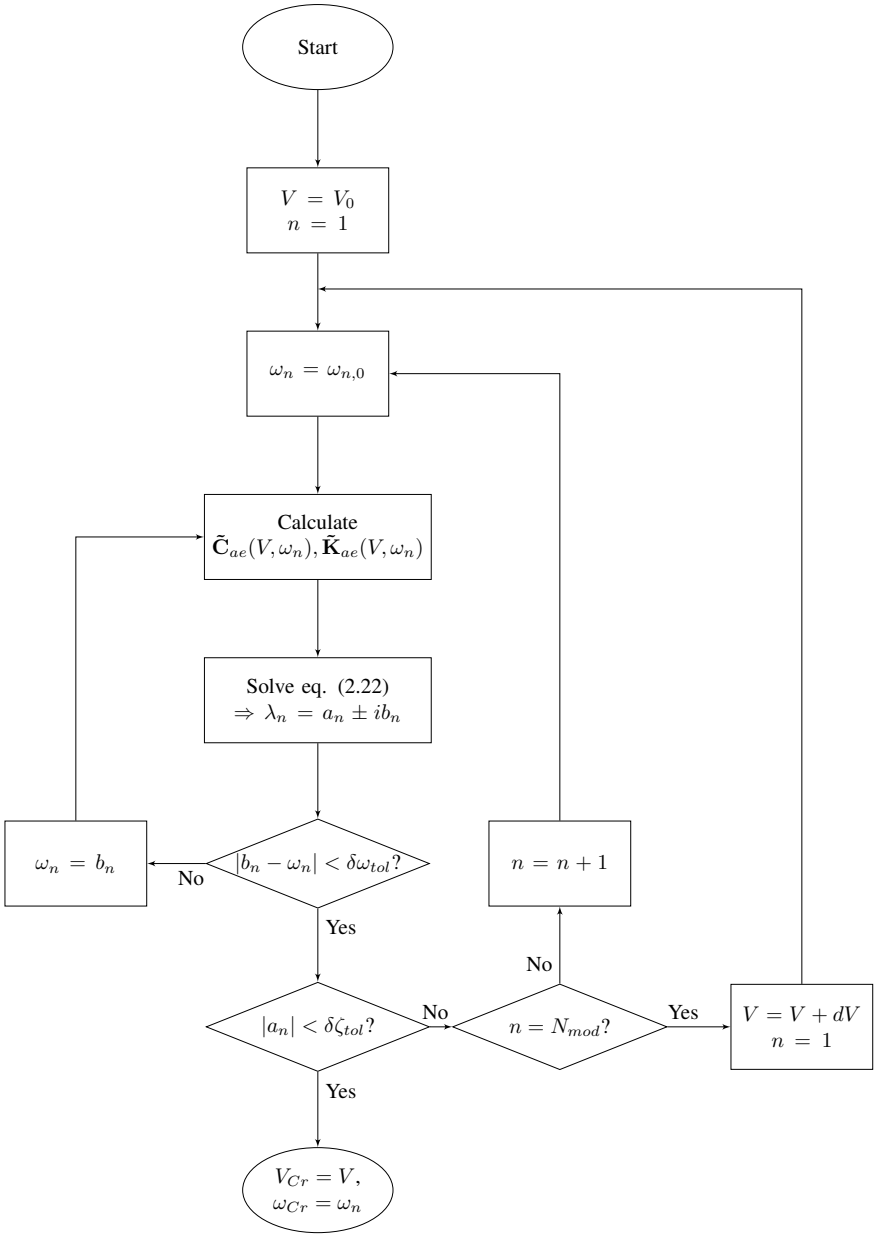

Figure 5.8: Routine for calculation of critical flutter velocity. A maximum number of iterations should be defined for loops both on ω and V, as the routine does not necessarily converge.

The roughness factor is defined as follows:

$$c_r(z) = k_r \cdot \ln\left(\frac{z}{z_0}\right), \qquad z_{min} \leq z \leq z_{max} \tag{5.8}$$

$$k_r = 0.19 \left(\frac{z_0}{z_0, II}\right)^{0.07} \qquad \text{is the terrain factor} \tag{5.9}$$

z_0 is the roughness length at the construction site, taken as 0.01m for the Hardanger Bridge, which belong to terrain class I. $z_{0,II} = 0.05\mathrm{m}$ is the roughness length of terrain class II. Terrain class I gives $z_{min} = 1\mathrm{m}$, while $z_{max} = 200\mathrm{m}$ is a fixed value.

$c_{prob} = 1$ for a return period of 50 years, otherwise it is defined as

$$c_{prob}(R) = \left(\frac{1 - 0.2 \ln\left(-\ln\left(1-p\right)\right)}{1 - 0.2 \ln\left(-\ln\left(1-0.02\right)\right)} \right)^{0.5} \tag{5.10}$$

(5.10) differ slightly from the expression for c_{prob} found in [29]; however, the same values are produced.

The value of $v_{b,0}$ is specified for each Norwegian municipality in [25]. The Hardanger Bridge crosses the Hardangerfjord in Ullensvang municipality, where $v_{b,0} = 26\mathrm{m/s}$ applies. Combining all the expressions, and using that $z_m = 63.5\mathrm{m}$ (see sec. 1.3), V_S is finally found as

$$V_S(63.5\,\mathrm{m}, 600\,\mathrm{s}, 500\,\mathrm{y}) = 43.3 \frac{\mathrm{m}}{\mathrm{s}} \tag{5.11}$$

For the purpose of this text, also a stochastic distribution of the extreme mean wind value is determined.

5.7 Probabilistic distribution of extreme mean wind value

The extreme wind value of sec. 5.6 have a probability of $\frac{1}{500} = 0.002$ to be exceeded each year. A probabilistic distribution would specify a probability of exceedance for each possible wind value. In order to find such a distribution, extreme wind values with a reference period of 2, 10, 50, 100 and 500 years, respectively, are calculated. Then, a Gumbel distribution is fitted to these data points (see sec. 3.4).

For each reference period only c_{prob} changes value, thus providing the results seen in table 5.3.

$R[y]$	$p[1/y]$	$V_S[m/s]$
2	0.5	29.95
10	0.1	34.80
50	0.02	38.57
100	0.01	40.05
500	0.002	43.29

Table 5.3: Extreme wind values, their expected reference period, and yearly probability of occurence.

In sec. 3.4, the CDF of a Gumbel distribution was defined as

$$F_X(x) = \mathrm{e}^{-\mathrm{e}^{-\frac{x-\mu}{\beta}}} \tag{3.28}$$

In this case, $F_X(x)$ is the probability that the maximum 10-min mean wind value a particular year is *below* the values specified in table 5.3. Therefore, the aim of curve fitting is to provide the values of μ, β that minimizes the total error of

$$1 - p = \mathrm{e}^{-\mathrm{e}^{-\frac{V_S - \mu}{\beta}}} \tag{5.12}$$

for the specified values. It is convenient to invert 5.12, making it linear in μ, β:

$$V_S = \mu - \beta \ln(-\ln(p)) \tag{5.13}$$

Using the built-in function regress.m in MATLAB, the parameters are found as

$$\mu = 29.4125, \qquad \beta = 2.2850 \tag{5.14}$$

The data points used in the regression is depicted together with the fitted CDF in fig. 5.9. The fit is relatively good, especially for high wind speeds.

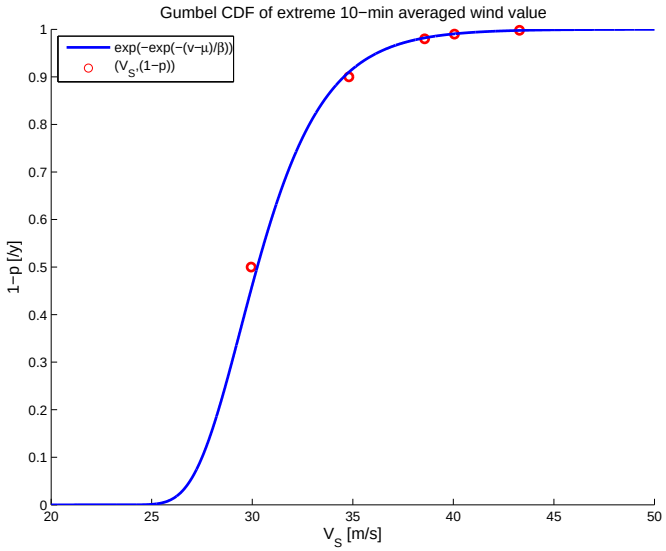

Figure 5.9: The cumulative distribution function associated with the extreme 10-min mean wind value at the Hardanger Bridge.

Chapter 6

Results

Based on the methods and models elaborated upon in 5, a probabilistic analysis of the Hardanger Bridge has been performed. The main aim of the simulations is to draw inferences about the reliability of the bridge. Obviously, also information and characteristics about the stochastic distribution of critical speed can be extracted. In this chapter, results are presented according to the natural order of which they were extracted. First, results from a deterministic analysis are presented. Secondly, critical speed simulations from case 1 and case 2 are presented. Thirdly, results from the reliability analysis for each of the cases are given.

6.1 Deterministic analysis

To get a starting point for probabilistic simulations, a deterministic analysis was performed. In this way it was possible to see which mode combinations to include in the probabilistic analysis. Even if it is theoretically possible to include 50 or even more modes in the analysis, computational effort increases rapidly when including additional modes. The aim of the deterministic analysis was to find a balance between accuracy and computational time. The deterministic analysis is simply performed by setting the covariance matrix of variables equal to zero.

Calculations were performed using the mean variables of both case 1 and case 2 (as defined in chapter 5). First, bimodal flutter speed were calculated using the 1st torsional mode together with the 1st and 2nd vertical mode, respectively. Then more modes were added succesively to see if they contributed to flutter. Among the first 50 modes, all symmetrical modes were tested to see if they reduced flutter velocity. Obviously, also modes with low shape similarity were checked in the multi mode flutter analysis, because small differences were assumed to make a difference for the probabilities involved.

In addition to the 1st and 2nd vertical and 1st torsional mode, which were identified as the modes dominating flutter in [8], the Abaqus model from SVV identified symmetrical torsional motion in mode 17. Inclusion of this mode gave a significant reduction of flutter velocity. After including the two first symmetrical horizontal modes (1, 5), as well as the

3rd symm. vertical mode (12), for a total of 7 modes, it was seen that additional modes changed the mean velocity very little.

	Case 1		Case 2	
Mode combinations	$V_{cr}[m/s]$	$\omega_{cr}[\frac{rad}{s}]$	$V_{cr}[m/s]$	$\omega_{cr}[\frac{rad}{s}]$
4+15	103.62	1.47	93.57	1.58
6+15	89.98	1.69	86.36	1.69
4+6+15	81.71	1.79	81.44	1.76
4+6+15+17	79.71	1.78	79.95	1.75
4+6+12+15+17	78.66	1.80	79.42	1.76
1+4+5+6+12+15+17	78.36	1.81	79.36	1.76
3 vert., 2 tors., 6 hor.	78.33	1.81	79.33	1.77
50 modes	78.30	1.81	79.67	1.77

Table 6.1: Critical flutter speed and critical frequency for different mode combinations for each of the two cases from sec. 5.4.2. Modes not contributing to critical flutter speed are not presented.

Table 6.1 shows the flutter speed and critical frequency for relevant mode combinations for both case 1 and 2 . The results differ beetween the two configurations, especially large differences are seen for the first bimodal flutter speed. For most other combinations, the calculated speeds differed with approx. $1m/s$. For the configuration where the 50 first modes were included, the critical speed velocity is reduced a little for case 1, compared to the value calculated with 7 modes included. However, the value increased for case 2. For both cases, including four horizontal modes (23, 24, 29, 36) in addition to the 7 mentioned, was identified to reduce V_{Cr} a little. All these 11 modes are shown in fig. 6.1.

The figure shows that all the modes are symmetrical, and that, generally, mode similarity is high. Especially, the high-numbered, horizontal modes are very similar. It should be noted that all of the 4 most high-numbered modes includes motion in parts of the bridge that is not accounted for in the flutter analysis, i.e. the pylons and the cables. Thus, even if they have similar mode shapes in the girder, there might be opposite deflections in the pylons and cable, making it less probable that these modes couple. It is not assessed whether this in fact is the case.

6.2 Probabilistic analysis of critical speed

Based on the calculations of mean flutter speed, it was chosen to proceed with 4 mode combinations, namely the ones including 3, 4, 7 and 11 modes from table 6.1. The mode combinations are given in the list below. Invaraiably, the different combinations are referred to as the ”3 mode combination”, the ”4-mode combination” as well as ”the combination using 7 modes”.

- 3-mode combination: Modes 4+6+15
- 4-mode combination: Modes 4+6+15+17
- 7-mode combination: Modes 1+4+5+6+12+15+17

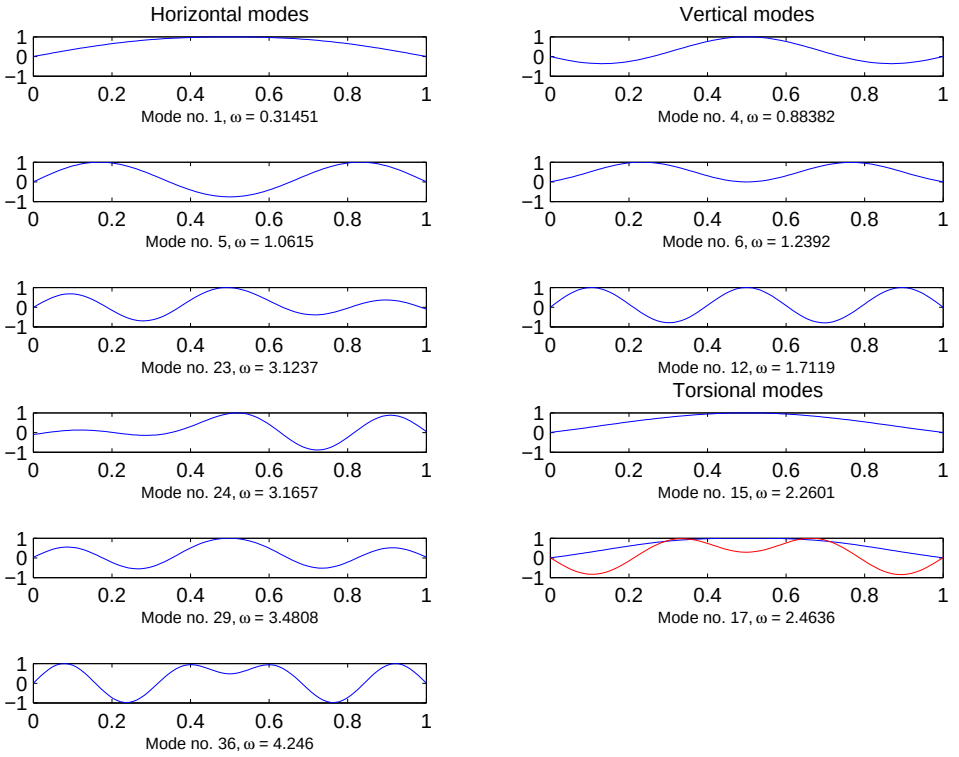

Figure 6.1: The 11 modes which had the strongest influence on flutter speed. Mode 17 had significant motion both in torsional (blue) as well as horizontal (red) direction. The ratio of the deflections of these two modes is not correct in the figure.

- 11-mode combination: Modes 1+4+5+6+12+15+17+23+24+29+36

Calculation time was the limiting factor for the scope of the simulations. Especially, the proposed method in case 1 was computationally expensive. For this reason, case 1 was evaluated only for the combinations with 3 and 4 modes, for which a total of $7 \cdot 10^5$ simulations was performed. For case 2, mode combinations with 3 and 11 modes were simulated $3 \cdot 10^6$ times. For mode combinations with 4 and 7 modes, $7 \cdot 10^6$ simulations were performed.

For some of the simulations, the routine did not converge towards critical speed within the specified number of frequency iterations. These simulations were removed from the data set when accumulating. To ensure that this did not give large differences in N_{sim} between the different cases and mode combinations, the number of simulation values was initially increased by 1-5 %, ensuring that enough valid simulations was recorded.

6.2.1 Critical speed - case 1

From the simulations of critical speed with flutter derivatives as defined in case 1 of sec. 5.4.2, it is seen that the mean values of table 6.1 are not reproduced exactly, deviating with about 1 m/s. This is due to the fact that the distributions are significantly skewed, implying that even though the deterministic calculations use the mean of the input values, the resulting value does not represent the true mean of the problem. The complexity of the problem does signalise that such an effect is not unexpected. From table 6.2 and fig. 6.2, 6.3, it is seen that the distributions of critical speed is skewed slightly to the left, giving a negative skewness value. This makes the mean value calculation somewhat non-conservative, because the distribution has an obesity of values to the left of the peak. The skewness is mainly seen in the extreme range of the tails. On the left side it could be described as thin and long, while on the left side it is thicker but shorter. The standard deviation is large, giving 99 % confidence interval about [40 - 110 m/s] for both mode combinations.

While the mode combination of case 3 was stable in the sense that very few outliers were observed, the raw data from mode combination 4 showed significant deviations from what would be reasonable to expect. In the velocity distribution at the upper left corner of fig. 6.3, no outliers are seen. However, in the frequency distribution, a small peak is seen where $\omega_{Cr} \approx 2.4$, as well as a few outliers for $\omega_{Cr} \approx 1.1$. The effect of these outliers upon critical speed is seen in the scatter plot at the lower right corner of the figure. They are distributed over a wide range of velocities. Notably, the 500 year design speed of 69 m/s was violated in 13.5% and 14.1% of the simulations for the 3-mode and 4-mode combination, respectively.

In table 6.3, these values are seen to result in a very high skewness value of the distribution. If the outliers are removed, all results are in accordance with what could be expected from the combination with 3 modes. Since the high valued frequencies were distributed over a wide range of critical velocities, no significant effect of these were seen upon the mean value of critical speed.

Also for a little share of the simulations with the 4-mode combination, the routine did converge at very high velocity, giving a frequency equal to zero. This occured for simulations where the random residual input gave a high initial damping value for the 1st torsional mode. Zero frequency corresponds to the physical phenomenon of static divergence, however, the routine is not constructed to take this into account, so it is not given that these events actually occurred because of static divergence. The number of simulations were this occured was very low, so it was decided to remove these data point from the sample.

For the 4-mode combination with outliers removed, V_{Red} had a mean value of 2.41. A 99 % confidence interval was given by $\{1.06\text{-}3.76\}$. The most extreme values of this interval is outside the velocity range of the test campaign, but not by large numbers.

V_{Cr}				
N_{mod}	μ	σ	γ_1	$\mathrm{CI}_{99\%}$
3	80.512	12.062	-0.276	39.58-113.61
4	78.957	10.935	-0.157	41.83-110.63
4*	78.924	10.888	-0.178	41.80-110.25

Table 6.2: Mean, standard deviation, and skewness values of critical speed based on $7 \cdot 10^5$ simulations.
*: Results with outliers removed.

ω_{Cr}			
N_{mod}	μ	σ	γ_1
3	1.816	0.126	0.277
4	1.814	0.126	0.649
4*	1.812	0.120	0.278

Table 6.3: Mean, standard deviation, and skewness values of critical frequency based on $7 \cdot 10^5$ simulations.
*: Results with outliers removed.

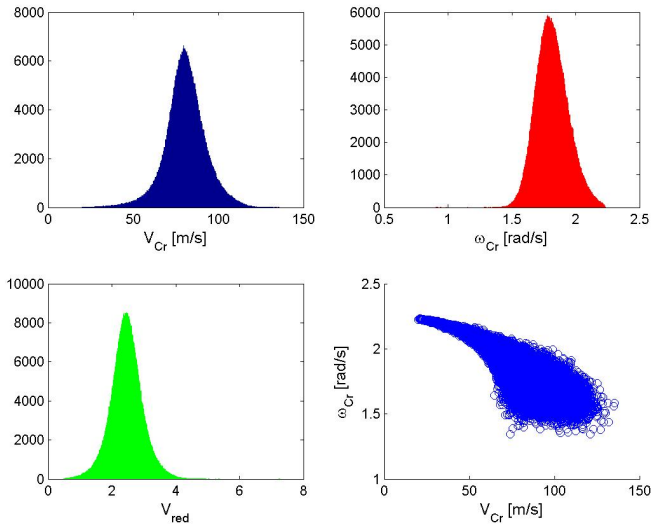

Figure 6.2: Distributions for the 3 mode combination. V_{Cr}, ω_{Cr} and V_{red}, and a scatter plot illustrating correlation between V_{Cr} and ω_{Cr}.

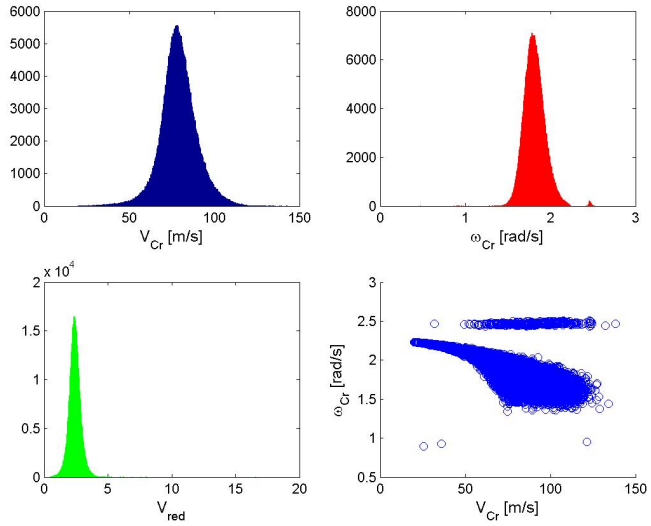

Figure 6.3: Distributions for the 4 mode combination with outliers included. V_{Cr}, ω_{Cr} and V_{red}, and a scatter plot illustrating correlation between V_{Cr} and ω_{Cr}.

6.2.2 Critical speed - case 2

While all the stochastic input variables for calculation of critical speed were normally distributed, simulations demonstrated that the output values, most notably the critical speed and critical frequency, were not normally distributed. However, the skewing was in the opposite direction of what was seeen in case 1. The tables and fig. 6.4 show that the distribution is positively skewed. This tendency can also be noted from the extreme values of the 7 mode simulations, which are 67.50 m/s and 95.74 m/s respectively. The first value is somewhat closer to the mean value. For the 7 mode combination a 99% confidence interval symmetrically distributed about the median was calculated to be $73.71 - 86.91 m/s$. The distributions show significant skewness for all different mode configurations, even though the means of the stochastic distributions are not very far from the values calculated in table 6.1. The same is true for the critical frequency. Some key characteristics of the distributions are summed up in tables 6.4 and 6.5.

V_{Cr}				
N_{mod}	μ	σ	γ_1	$\text{CI}_{99\%}$
3	81.567	2.306	0.328	76.29-88.24
4	80.050	2.212	0.241	74.80-86.24
7	79.597	2.643	0.338	73.71-86.91
11	79.576	2.644	0.334	73.71-86.84

Table 6.4: Mean, standard deviation, and skewness values of critical speed based on $3 \cdot 10^6$ simulations.

ω_{Cr}			
N_{mod}	μ	σ	γ_1
3	1.757	0.039	-0.567
4	1.746	0.039	-0.499
7	1.760	0.044	-0.676
11	1.759	0.044	-0.679

Table 6.5: Mean, standard deviation, and skewness values of critical frequency based on $3 \cdot 10^6$ simulations.

The distributions of critical frequency also show little deviation from the calculations in sec. 6.1. Here, a distinct negative skew is seen. Large values of frequency correspond very closely to low values of critical speed, as seen in 6.4. For the 7 mode combination, a correlation coefficient of -0.914 was calculated.

From the simulations of V_{Cr} and ω_{Cr}, information about V_{red} is readily available. For the 7 mode combination, the mean of V_{red} was found to be 2.48, while a 99% confidence interval was given by $\{2.19\text{-}2.90\}$. In the case of 3 modes, the same values were found as 2.54 and $\{2.27\text{-}2.93\}$, respectively.

Among the calculated probability distributions, the combination with 4 modes points out not to follow the same tendency as the other curves. Especially, the values of σ and γ_1 for critical velocity do not follow the trend that is outlined by the three other mode combinations. For critical frequency, all values deviate somewhat from what would be expected. However, the discrepancies are small. Fig. 6.4 and 6.5 provide distributions of critical velocity and frequency for the 7-mode and the 4-mode combinations, respectively. For the velocity, the peak is more significant in the latter figure, which is consistent with the slightly lower variance seen for the 4-mode combination.

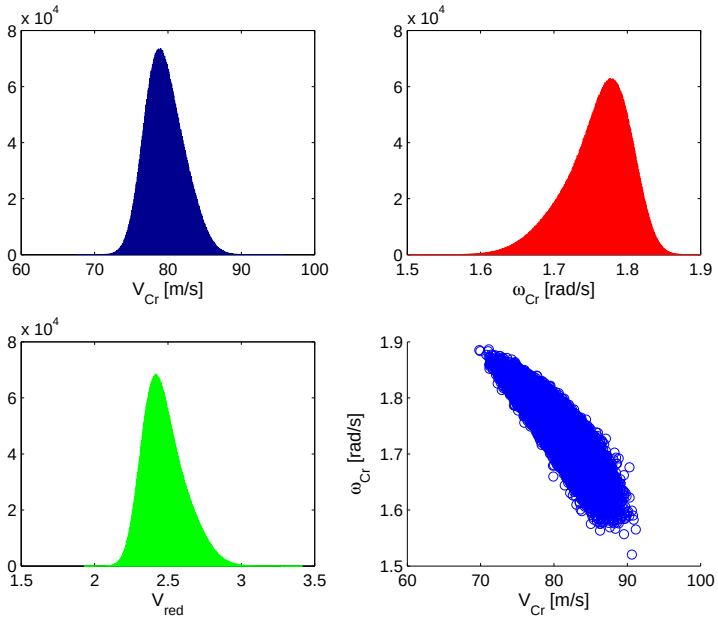

Figure 6.4: Distributions for the 7 mode combination. V_{Cr}, ω_{Cr} and V_{red}, and scatter plot illustrating correlation between V_{Cr} and ω_{Cr}.

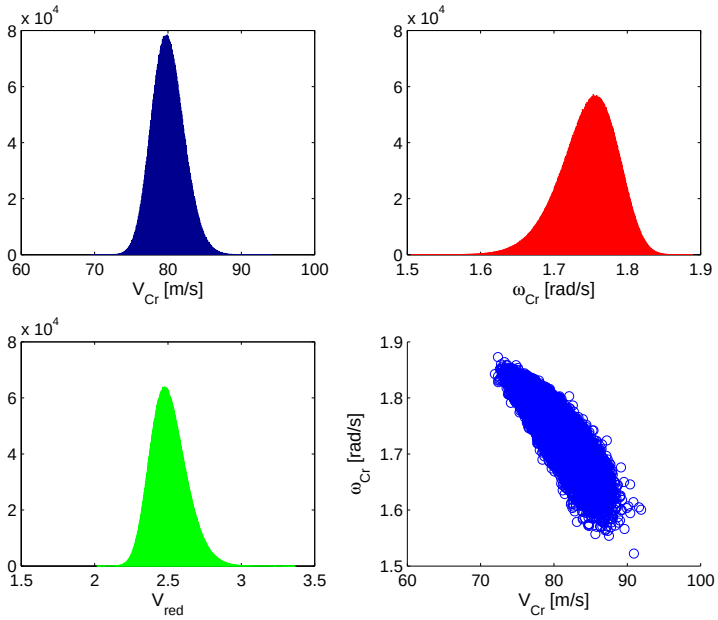

Figure 6.5: Distributions for the 4 mode combination. V_{Cr}, ω_{Cr} and V_{red}, and scatter plot illustrating correlation between V_{Cr} and ω_{Cr}.

6.3 Reliability analysis

In sec. 3.8.1, it was suggested that extrapolation from a series of "reduced" probabilities of failure, based on a parametrized class of limit state functions, could yield good estimates of the true failure probability.

$$M(\lambda) = M - \mu_M(1-\lambda), \qquad 0 \leq \lambda \leq 1 \tag{3.47}$$

Calculations using the enhanced Monte Carlo method was performed based on ACER_1.m, a MATLAB program developed at NTNU. The program was adjusted to suit the current application. The implementation of the enhanced method used in the program was seen to be very sensitive to input values. Næss noted that the problem of estimating an extrapolation curve for failure probability becomes ill-defined when the input parameter $c_0 \approx 1$. This issue also arose in some of the cases studied in this thesis. To avoid the problem, some executions were made with a rewrite of the limit state function, namely

$$M = \sqrt{V_{Cr}} - \sqrt{V_S} = 0 \tag{6.1}$$

The value of this function is the same as the original function at the limit $M = 0$, and it is negative when $M = V_{Cr} - V_S$ is. It should therefore produce the same value of failure probability at this point. However, for nonzero values of M, the parametrization $M(\lambda)$ takes on different values, making the extrapolation curve follow another path. For

the cases with 4, 7 and 11 modes, the limit state in 6.1 performed better than the original function. In the code, it is attempted to construct extrapolation curves not only for the failure probability, but also for 95 % confidence intervals enclosing the $p_f(\lambda)$ curve. Therefore, the problem could become illdefined for one of the three regression problems in an execution, while not for the remaining. For some of these cases, values could be found for failure probability even though estimates of confidence intervals could not be provided.

Because the performance of (6.1) was generally good, this was implemented for all mode combinations. A comparison of the results using this limit state and the limit state $M = V_{Cr} - V_S$ is provided for the combination with three modes in case 2. For all mode combinations, estimates of failure probabilities, confidence intervals and safety levels are provided for different combinations of N_{sim} and λ_M. While λ_M, the maximal parameterization value used as basis for regression calculations, were seen to have some effect on the extrapolation curve, λ_0 mainly affected the stability of the regression problem; it did not have a significant effect upon the resulting failure probability. In case 1, it was set at 0.6 because of the high probabilities involved, while in case 2, it was fixed at 0.2.

The probability distribution of the maximal 10-min mean wind value, the "second part" of the reliability analysis, was found in sec. 5.5. For convenience, an illustration of the probability density function (PDF) is given in fig. 6.6.

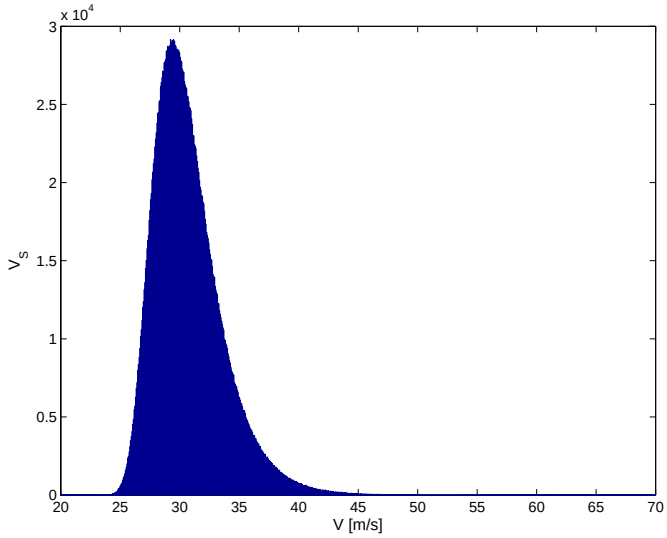

Figure 6.6: $3 \cdot 10^6$ realisations of the 10-min extreme mean wind distribution. The values of the distribution express the probability that a specific wind speed is exceeded during *one* year.

The distribution is skewed to the right of the peak, typical for extreme value distributions. The distribution is bounded, not theoretically, but for practical purposes, by a lower limit of approx. 24 m/s. Since the probabilities calculated in the following section express the probability of failure during one year, they could also be understood as expected *frequencies* of failure, meaning e.g. that a failure probability of 0.1 implies that flutter speed

is expected to occur once every ten years.

6.3.1 Reliability analysis - case 1

Because of the large variance seen in the distributions of case 1, failure probabilities are expected to be high. Even crude Monte Carlo simulations yielded an approximate value of failure probability, since the unparametrized limit state function was violated in some of the cases.

For the three mode combination, crude Monte Carlo simulations gave $pf_0 \approx 1.58 \cdot 10^{-3}$. The 4 mode combination yielded $1.23 \cdot 10^{-3}$ and $1.27 \cdot 10^{-3}$ with and without outliers included, respectively. Also from fig. 6.7 and 6.8, it is seen that the limit state is violated by some of the values.

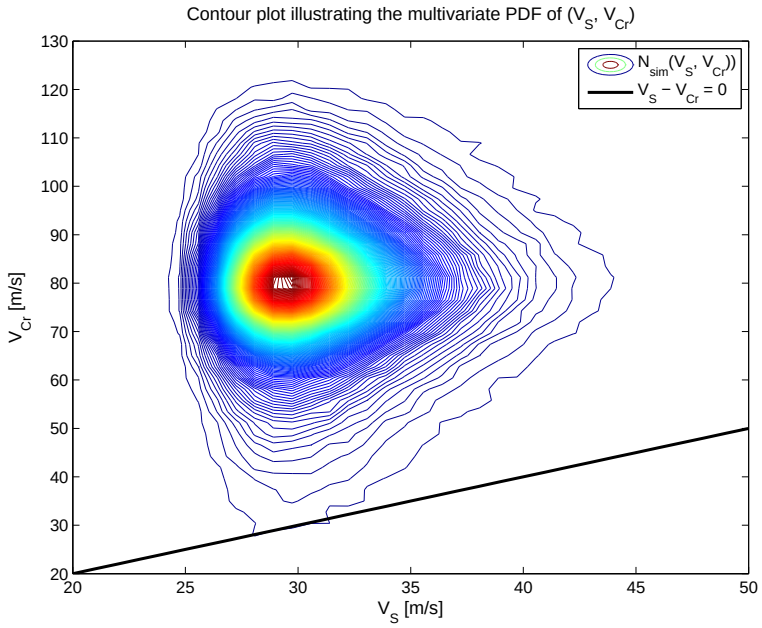

Figure 6.7: 3 mode combination: Contour plot for the bivariate density distribution of the reliability analysis. 200 isosceles contour plots are shown for a total of $7 \cdot 10^5$ simulations.

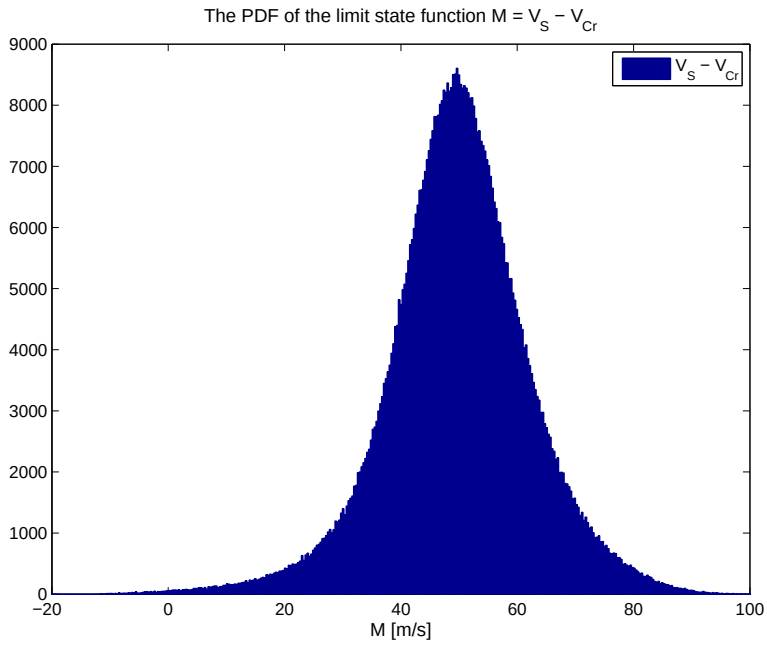

Figure 6.8: Graphical realisation of the limit state function shown for combination with three modes case 1.

Because of the high probailities involved, the accuracy achieved with the method is very high, not only for safety levels, but also for the probabilities calculated. The results are summarised in table 6.6. Also, fig. 6.9 illustrates the extrapolation for a case using the 3 mode combination with $\lambda_M = 0.8$. The blue "bullet points" is the calculated values of reduced failure probabilities. In the log space, it is seen that the extrapolation curve follow the points very closely. Also, the confidence bands are very narrow.

The results are not in accordance with the safety level that is needed and expected for this type of construction. Above all, they indicate that something is wrong with the suggested modelling of flutter derivatives. In chapter 7, the approaches used for the two different cases are discussed.

$N_{sim} = 7 \cdot 10^5$		3 modes			4 modes		
		$p_f \cdot 10^3$	$CI_{95\%} \cdot 10^3$	β	$p_f \cdot 10^3$	$CI_{95\%} \cdot 10^3$	β
λ_M	0.7	2.2	2.1-2.3	2.85	1.8	1.7-1.9	2.91
	0.8	2.0	1.9-2.1	2.88	1.5	1.4-1.6	2.96
	0.9	1.8	1.7-1.9	2.91	1.2	1.1-1.3	3.03

Table 6.6: Failure probabilities, 95 % confidence intervals and safety levels for two different mode combinations of case 1. 4-mode combination is calculated with outliers removed.

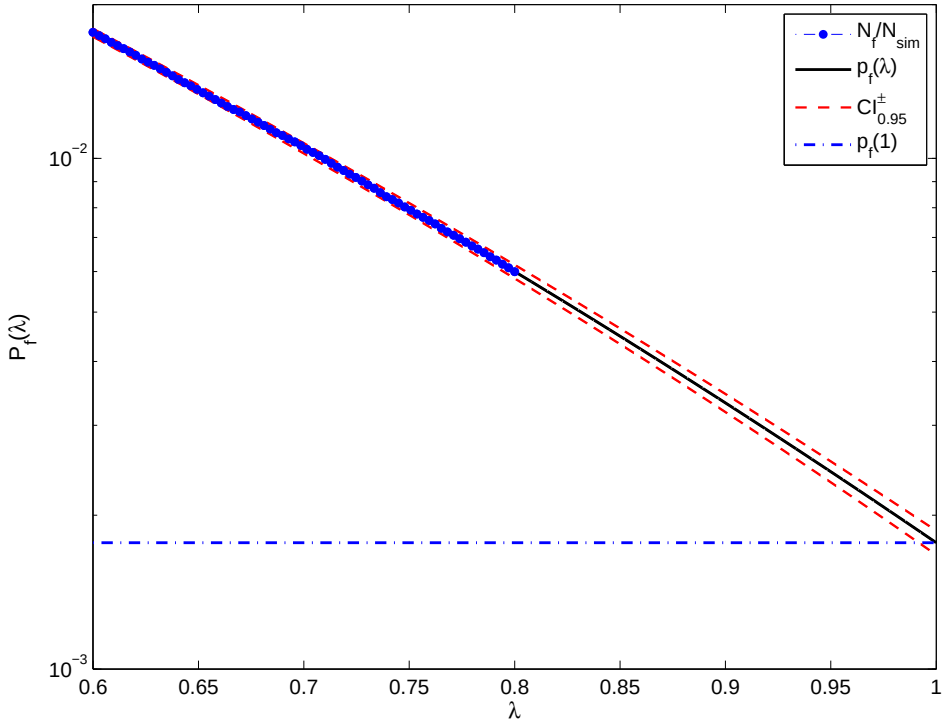

Figure 6.9: Case 1, 3 mode combination: Extrapolation curves for failure probability using different combinations of N_{sim} and λ using enhanced Monte Carlo simulation.

6.3.2 Reliability analysis - case 2

The simulations performed with case 2 are distributed more narrowly than the ones observed in case 1, implying that the failure probabilities will be significantly lower. Indeed, this was seen to be the case. For the failure probabilities seen for case 2, the coefficients of variance between different estimates were relatively high. However, the estimates of the safety level $\beta = \Phi^{-1}(p_f)$ were found to be within reasonable bounds for most of the simulations. Generally, the failure probabilities were in the range of $1^{-10} - 3^{-9}$, giving safety indexes ranging from approx. 5.8 to 6.4.

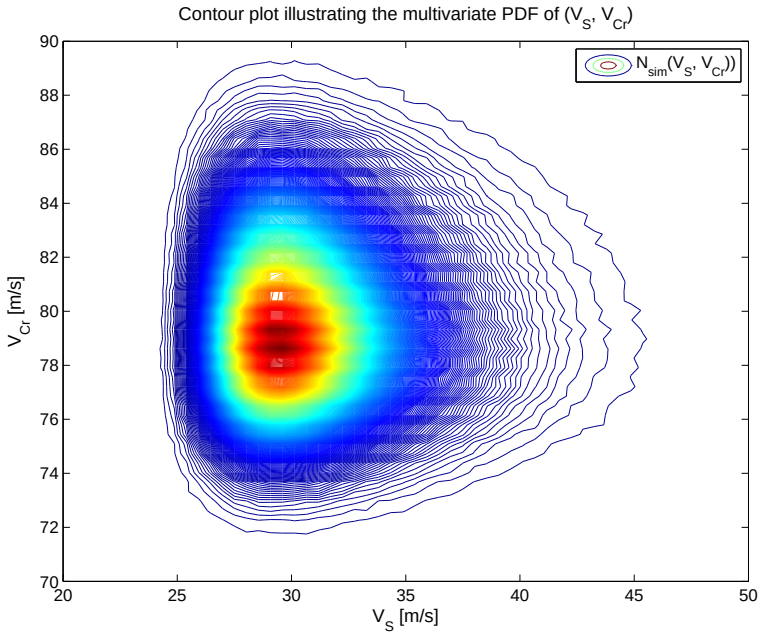

Figure 6.10: 7 mode combination: Contour plot for the bivariate density distribution of the reliability analysis. 400 isosceles contour plots are shown for a total of $7 \cdot 10^6$ simulations.

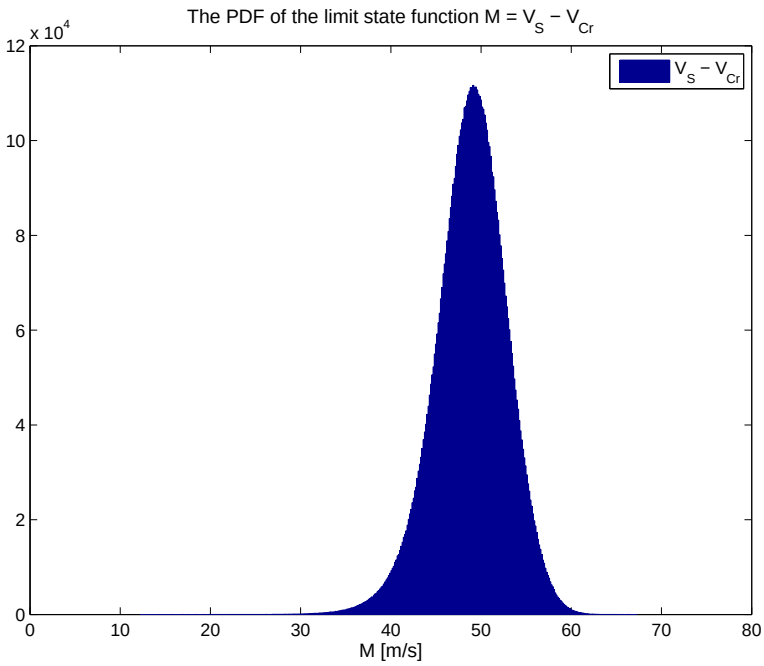

Figure 6.11: Graphical realisation of the limit state function shown for combination with seven modes case 2.

Fig. 6.10 and 6.11 clarifies why traditional simulation methods cannot provide estimates of failure for the flutter reliability problem. The extreme value of the limit state distribution for the 7 mode combination with $7 \cdot 10^6$ simulations is approx. 12 m/s. The shape of the critical speed distribution, as well as the Gumbel distribution of the extreme 10-min mean wind speeds, are visible in 6.10. Seeing from bottom to top, the contours are slightly closer to each other on the negative side of the peak, in accordance with the right skew found in sec. 6.2.2. In the following, failure characteristics are defined for four different mode combinations. The failure probability is assessed using different values of λ_M and N_{sim}. Full tables with the calculated probabilities of failure are found in app. A. All referenced figures are gathered in the end of the chapter.

Mode combination with 3 modes

For the mode combination with modes 4, 6 and 15 included, a total of $3 \cdot 10^6$ simulations were performed. To decide which value to choose for λ_M, an estimate is given by studying the development of $\hat{p}_f(\lambda)$. When the curve of $(\lambda, \hat{p}_f(\lambda))$ no longer follow a smooth path, no additional information is expected to be retrieved by increasing λ_M. The development of these data points are seen as the blue dots in fig. (6.12). For the case of $3 \cdot 10^6$ simulations, the limit was found for $\lambda_M \approx 0.6$. It was chosen to gather failure probabilities and confidence intervals by variying the maximal λ value of λ between 0.4 and 0.7, and vary N_{sim} in the range of $0.7 - 3 \cdot 10^6$. The most stable results were found for the values of

N_{sim} and λ_M, shown in fig. 6.13. In the plot, the trend-lines connect failure probabilities for one value of λ_M, while the x-axis show increasing values of N_{sim}. Each group of data points show calculations for the same value of N_{sim}. However, to show the error bars properly, they are slightly separated in the figure.

In the plot, some surprising development is seen. When the number of simulations are increased, it would be expected that uncertainty is reduced, at least for the same values of λ_M. In fig. 6.13, the tendency is the opposite, as the width of the confidence intervals increases. Also, it is seen that different intervals do not cover the same values, which is not in accordance with what one would expect if they were based purely on statistical assumptions. Further, the probabilities values do not seem to converge towards a stable value. It suggests that the number of simulations should be further increased to get a better estimate.

On the other hand, for the probabilities involved, the calculated values could be said to deviate relatively little, with probability estimates ranging at $0.7 - 6 \cdot 10^6$. If the values were studied in the log space, in accordance with the nature of the enhanced method, the variation seen in fig. 6.13 would have been reduced. This is realised when studying the values of the safety index.

Fig. 6.12 illustrates the nature of the calculations, and how the estimates of p_f deviate in the log space. In table 6.7, some typical values of the safety index are provided.

For the 3 mode combination, a very brief comparison between the square root limit state and the original limit state function was performed. The results for the extrem values of N_{sim} are suggested in fig. 6.14. The green and blue bars show the values using the square root limit state, while red and orange colours are estimates using the original function. Notably, the x-axis here show the values of λ_M. No distinct differences are seen; however, the two methods obviously do not produce exactly the same result.

$\beta_f = \Phi^{-1}(p_f)$		N_{sim} /1000	
		700	3000
λ_M	0.4	6.16	6.15
	0.5	6.29	6.11
	0.6	6.33	6.24
	0.7		6.26

Table 6.7: Level of safety against failure using the square root limit state.

Mode combination with 4 modes

The investigations for the 4 mode combination, where modes 4, 6, 15 and 17 are included, were performed in the same manner as suggested in sec. 6.3.2. A total of $7 \cdot 10^6$ simulations were performed, and N_{sim} was varied between $0.7 - 7 \cdot 10^6$. The most stable solutions were found for λ_M between $0.45 - 0.6$, which are illustrated. in fig. 6.15. For other values, one of the confidence bands often became ill-defined.

The variation along the curves in 6.15 indicates that the p_f values stabilizes for $N_{sim} \geq 5.5 \cdot 10^6$. However, the variation of λ_M has a more significant effect upon the failure probability. Somewhat surprisingly, it was seen that $\lambda_M = 0.55$ yielded the highest failure

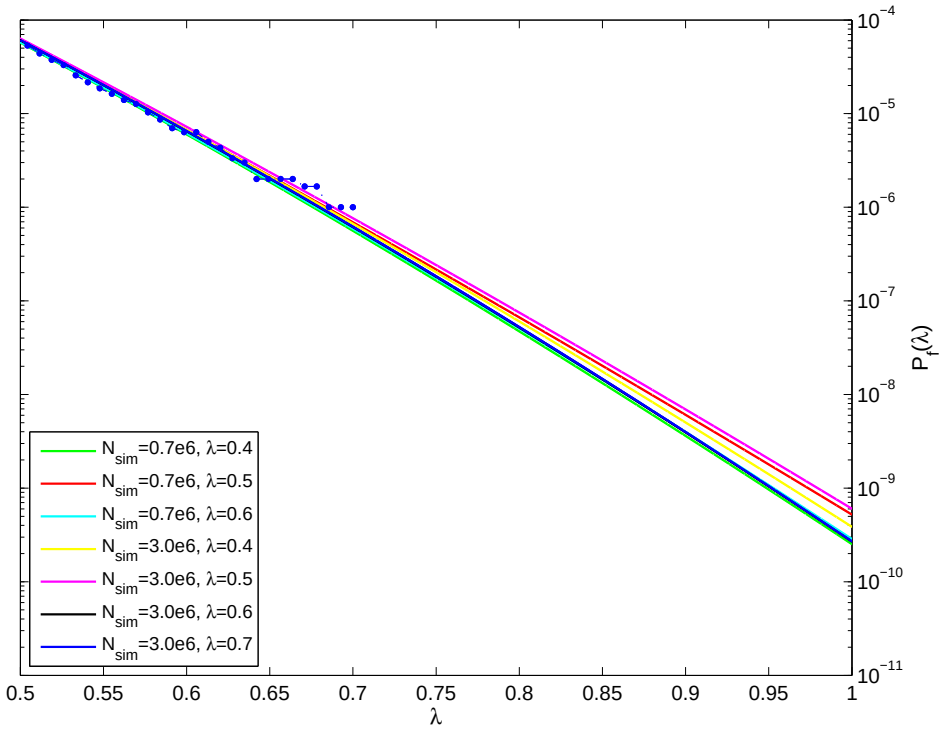

Figure 6.12: 3 mode combination: Extrapolation curves for failure probability using different combinations of N_{sim} and λ using enhanced Monte Carlo simulation.

probabilities. This stabilizing tendency was in opposition to what was observed with the 3 mode combination. However, both probabilities and confidence intervals took on larger values, with failure probabilities in the range of $4 - 12 \cdot 10^6$.

Table 6.8 illustrates that the variation of the safety index still is small.

$\beta_f = \Phi^{-1}(p_f)$		N_{sim} /1000		
		700	3000	7000
λ_M	0.4	5.96	6.19	6.10
	0.5	5.95	5.98	6.08
	0.6		6.02	6.08
	0.7		6.07	6.13

Table 6.8: 4 mode comb.: Typical values of the safety index.

6.3.3 Mode combination with 7 modes

The investigations performed for the 7 mode combination, where modes 1, 4, 5, 6, 12, 15 and 17 are included, were performed in the same manner as suggested in sec. 6.3.2. A

total of $7 \cdot 10^6$ simulations were performed, and N_{sim} was varied between $0.7 - 7 \cdot 10^6$. The most stable solutions was found for λ_M between $0.45 - 0.6$, which are illustrated. in fig. 6.16. Using a large number of simulations together with a low λ_M sometimes made the regression problem ill-defined, somewhat surprisingly.

Here, in opposition to what was seen for the 3 mode combination, the results do seem to be stable at high values of N_{sim}. However, both probabilities and confidence intervals take on larger values, with failure probabilities in the range of $8 - 25 \cdot 10^6$.

Table 6.9 illustrates that the variation of the safety index still is small.

$\beta_f = \Phi^{-1}(p_f)$		N_{sim} /1000		
		700	3000	7000
λ_M	0.4	5.88	5.90	5.95
	0.5	5.90	5.88	6.01
	0.6		5.95	6.06
	0.7		6.02	6.10

Table 6.9: 7 mode comb.: Typical values of the safety index.

6.3.4 Mode combination with 11 modes

For the 11-mode combination, modes 23, 24, 26, 29 were included in addition to the 7 previously mentioned. A total of $3 \cdot 10^6$ simulations were performed, and N_{sim} was, as for the 3 mode combination, varied between $0.7 - 3 \cdot 10^6$. The main results are depicted in fig. 6.17.

As with the 3 mode combination, the figure shows that stable values were not achieved for the current number of simulations. Especially noticeable is the peak found for some of the λ values at $N_{sim} = 2.5 \cdot 10^6$. The probabilities ranged in the area $2 - 12 \cdot 10^6$.

$\beta_f = \Phi^{-1}(p_f)$		N_{sim} /1000	
		700	3000
λ_M	0.4	6.22	6.15
	0.5	6.10	6.08
	0.6	6.20	6.21
	0.7	6.04	6.21

Table 6.10: 11 mode comb.: Typical values of the safety index.

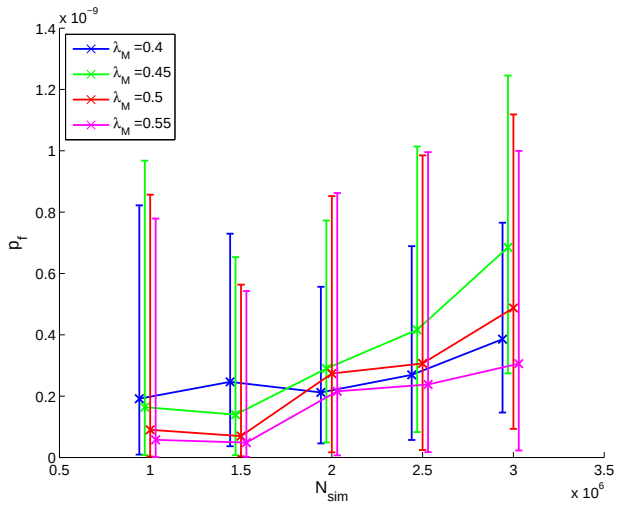

Figure 6.13: 3-mode combination: Failure probability and confidence intervals for different combinations of N_{sim} and λ.

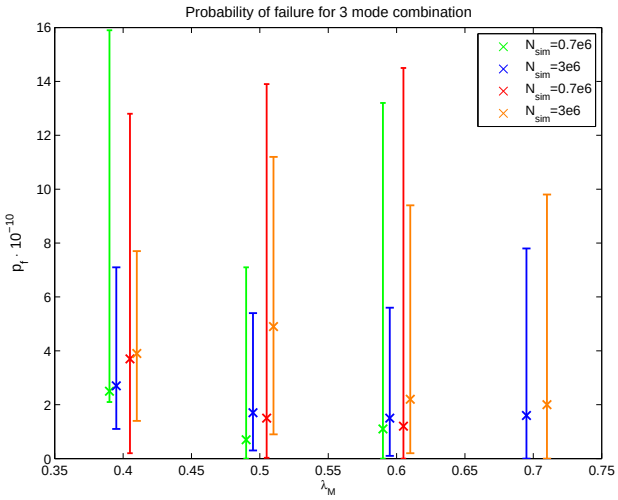

Figure 6.14: 3-mode combination: Failure probabilities using both the square root limit state function (blue, green) and the original (red, orange).

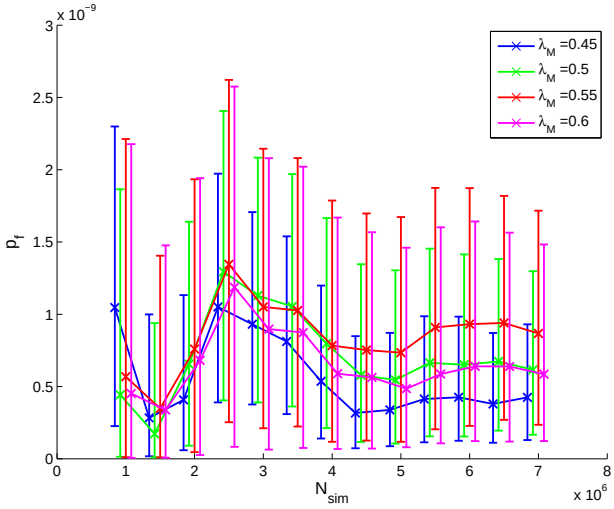

Figure 6.15: 4-mode combination: Failure probability and confidence intervals for different combinations of N_{sim} and λ.

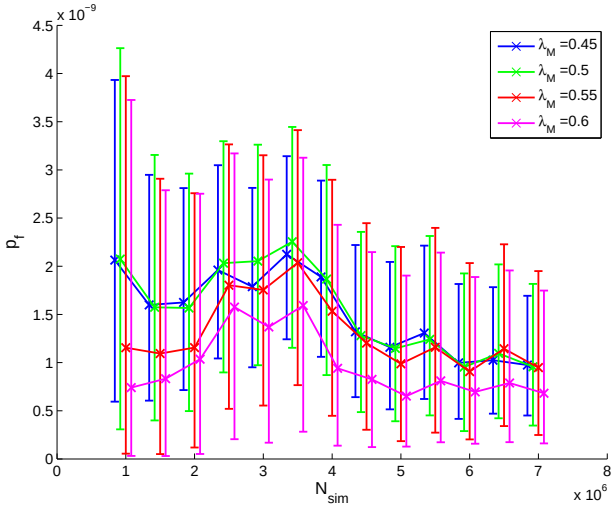

Figure 6.16: 7-mode combination: Failure probability and confidence intervals for different combinations of N_{sim} and λ.

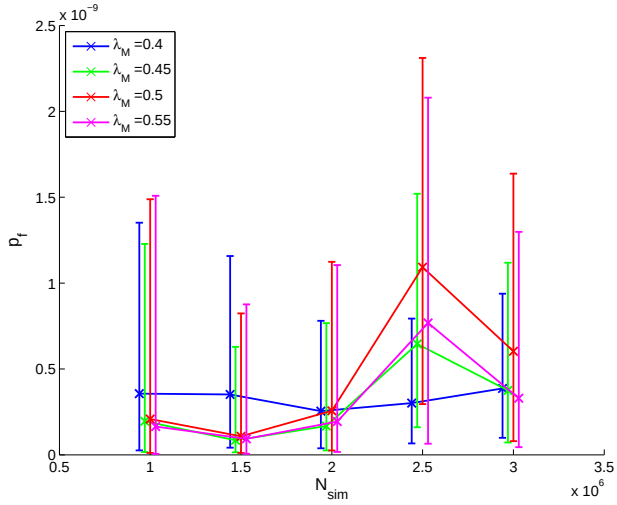

Figure 6.17: 11-mode combination: Failure probability and confidence intervals for different combinations of N_{sim} and λ.

Chapter 7

Discussion

In the previous chapter, a number of probability failure calculations based on different choices of N_{sim}, λ_M and mode combinations, has been performed.

The variation of the values seems to depend on all the three parameters. For the 3 and 11 mode combination, $3 \cdot 10^6$ simulations were generated. By varying N_{sim} between $0.7 - 3 \cdot 10^6$ the failure probability did not stabilize. It was not possible to conclude that mode combination 11 had a higher probability of failure, as would be expected from the distribution of the simulations. For this range of values, p_f varied between $1 - 24 \cdot 10^{-10}$, with corresponding safety indexes from 6.36 to 5.85. Mode combination 7 took on the highest values. Including the 95 % confidence intervals, probability values from 0 to $50 \cdot 10^{-10}$ were recorded, providing a lower safety index of 5.7. Even if the figures in the last chapter suggest that there is a large uncertainty in the determination of p_f, the difference in the safety index β is limited.

For the 4 and 7 mode combination, $7 \cdot 10^6$ simulations were generated. Higher N_{sim} stabilized the values of p_f. For $N_{sim} \in \{5 - 7 \cdot 10^6\}$, p_f ranged from $3 \cdot 10^{-10}$ to $15 \cdot 10^{-10}$, with an upper confidence limit of $24 \cdot 10^{-10}$. The respective values of β are 6.19, 5.93 and 5.85. In structural design codes, the necessary value of β are taken implicitly into account to calibrate safety factors, while the actual value of the safety index are rarely provided. However, in a more general overview, Schneider suggests that $\beta = 5.0$ *per year* provides sufficiently safety for non-redundant failure of bridges [19]. While it is the previously mentioned design rule that should be used to assess whether sufficiently accuracy is provided, Schneiders value works as a comparison to what the β value means.

Normally, confidence intervals would be interpreted as bounds of the *true* value of some size. Here, they are estimated by use of extrapolation, resulting in a large scatter of the distribution of upper and lower limits. Sometimes, two different confidence limits share no common points, which leave it rather obvious that at least one of them is incorrect. Thus, the size of the confidence intervals should be taken as a qualitative measure of the quality of the calculated value, rather than quantitative estimates of the 95 % confidence limits.

In this chapter, four main items will be discussed.

1. The results from the deterministic critical speed analysis will be considered. (sec. 7.1)

2. An explanation to why the two derivative modelling cases predict very different values will be given, and it will be concluded that case 2 is the preferable way of modelling. (sec. 7.2)

3. A comparison between the results from case 2 is provided. (sec. 7.3)

4. The validity of the results will be discussed. (sec. 7.4)

7.1 Results from deterministic analysis

In the previous chapter, results from a deterministic analysis for each of the two modelling cases in the study was presented in tab. 6.1. While the results showed the same tendency, a significant difference of approx. 1 m/s was observed for the extreme mode combinations. No evidence was found as to why this difference was observed. The different mean trendlines for the flutter derivatives predict very similar values at the point of critical speed, at least for all flutter derivatives thought to produce a significant impact on flutter speed. In Øiseth's thesis, critical speed was found at 78 m/s, for a trimodal combination. Since the Abaqus model used in this study "splits" fundamental torsional motion into two different modes, the trimodal flutter limit in [8] should be compared to the limit of the present 4 mode combination. Thus, it seems that the value of case 1 complies best with Øiseth's work. Whether the true critical speed is found at 78 m/s, 79 m/s or at some other value could still not be said with certainty. However, it is interesting to study what effect such a difference yields upon the probability of failure. Obviously, the distributions from case 1 and case 2 cannot be compared directly. Therefore, to assess this, failure probabilities were calculated for the 7-mode combination of case 2, successively shifting the mean of the distribution 1, 2 and 3 m/s in the negative direction. The results are depicted in fig. 7.1.

Since exactly the same random variables are used in each calculation, the resulting shift of probability values are comparable for each value of N_{sim}. For high values of N_{sim}, the first shift results in p_f increasing from $5 - 6 \cdot 10^{-10}$ to $9 - 10 \cdot 10^{-10}$. From many of the figures in the previous chapter, it is seen that different choices of λ_M can provide the same shift of failure probabilities. A shift of 3 m/s increases failure probability to $30 \cdot 10^{-10}$.

One of the purposes of this study was to see if the inclusion of experimentally determined horizontal derivatives, would have any significatn impact on the critical speed and its stochastic distribution. From the deterministic results in tab. 6.1, one might infer that the contribution from horizontal modes is of minor importance. In the modelling of case 1, the achieved reduction of flutter speed by introducing the two first horizontal modes, are 0.3 m/s, while in case 2, the difference is as low as 0.06 m/s. Similar values were found by calculating the mean from the probabilistic data samples in tab. 6.2 and 6.4. From the discussion in chapter 4, as well as the differences obseved by the different predictions of mean response, it is obvious that the true critical speed cannot be calculated with decimal accuracy. In the deterministic analysis, appropriate accuracy therefore seems to be achieved by inclusion of the four first modes. In sec. 7.3, it is investigated if the variance contributions from horizontal modes have any significance.

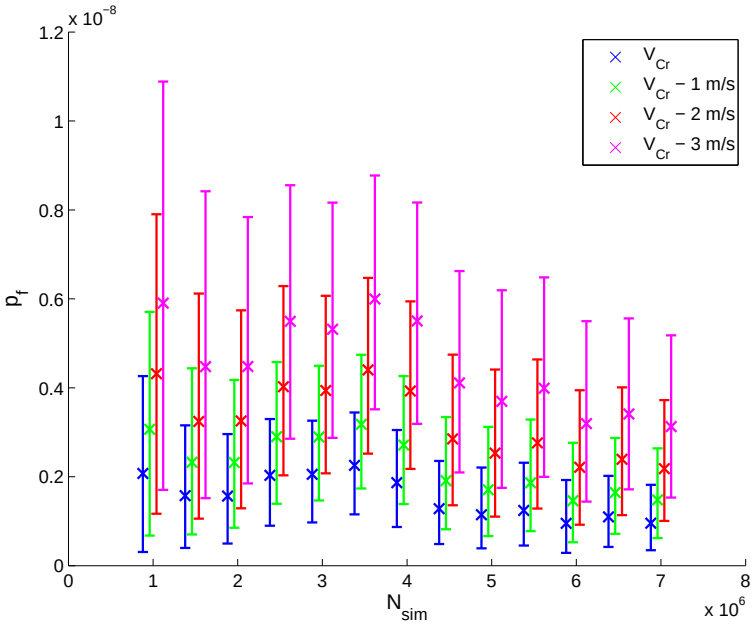

Figure 7.1: 7 mode combination: Effect of shifting mean value. $\lambda_M = 0.5$

7.2 Comparison between the two cases

From the results in 6, one remarkable tendency stands out. The difference between the results accumulated in case 1 and case 2 is very large. Above all, this is due to the modelling assumptions which are suggested in 5. In case 1, the variance modelling was based on uncertainty of the residual terms, while in case 2, the variance modelling was based on the uncertainty of the mean response. The first case follow the same guidelines as a previous thesis, where a probabilistic analysis of critical speed at the Hålogaland Bridge was performed [16]. Here, reasonable results, with limited variance of flutter speed, were provided. Comparing with this study, two main differences are seen. Firstly, quasi-static coefficients were used for the horizontal derivatives. Secondly, the flutter derivative residuals from section testing of the Hålogaland Bridge were somewhat more narrowly distributed. In the present analysis of case 1, two mode combinations were tested. Neither of these included horizontal modes. Therefore, the significance of horizontal modes should not be significant. However, the differences in residual scatter could provide some explanation to the differences observed.

Attempting to explain why the results from the two cases differ, a closer look at the flutter derivative modeling is required. In a case study on the proposed project of the Messina Bridge, a sensitivity analysis revealed that flutter derivatives H_3^* and A_2^* were the most influential derivatives, followed by A_3^*, A_1^* and H_1^* [27]. This implies that if all derivatives had the same coefficient of variance, H_3^* and A_2^* would be most influential on the variance of critical speed. While the results presented in this study might not be rep-

resentative for the Hardanger Bridge, they provide a starting point to compare the results of the two cases. The section tests of the Hardanger Bridge provided measurements of H_3^* and A_3^* with very little variance, while the scatter for H_1^*, A_1^* and A_2^* were larger. In 7.2-7.4, 100 realisations of the randomly distributed curves are provided for each of the three derivatives H_1^*, A_1^* and A_2^*.

Visually, the realisations differ significantly. Above all, the fact that the flutter curves of case 1 are forced to pass through zero makes a significant difference. However, the value of the flutter curves for low values of critical speed is not seen to make a significant difference. The critical reduced speed is centered around $V_{red} \approx 2.5$, and in the 7 mode combination a 99 % confidence interval of $\{2.10, 2.90\}$ is found. For case 1, the spread is larger, but still, 99 % of the values is between $\{1.06\text{-}3.76\}$. Consequently, the values of the flutter curves for these values are the most interesting. For case 2, the realisations for the different derivatives are within the bounds of the most extreme measurements. This is expected, because the curves are variations of the mean response. Outside the measurement range, the extreme realisations of flutter curves take on values which are not realistic. Especially, this is observed for derivative A_2^*, for which the testing campaign only provided measurements for values of V_{red} up to 2.1. The fact that the V_{red} values from measurements are not equal for all derivatives, are explained from the nature of the test, which is described in chap. 5.

For case 1, more extreme deviations from the measurements are seen in the range of critical reduced velocity. As previously stated, residual terms are provided as increasing functions of V_{red}, the assumption behind being the size of residuals increasing with wind velocity. From fig. 7.2-7.4, this assumption can be justified. However, it is also evident that after the scaling (see 5.4.1), the significance of residuals for low wind speeds increases, and the uncertainty is overestimated in the range of critical speed. For derivative A_2^*, which is the term relevant for torsional damping, visual evidence of this is given in fig. 7.4. Many of the curves predicting the measurements for low wind speed well, overestimates the measurements for large values of V_{red} with a significant margin. The same tendency holds for fig. 7.2-7.3 as well, residuals for low wind speed are predicted with good accuracy, while the curves overshoot the scattered values at high wind speed.

Also, the figures suggest that there are challenges of forcing the curves through (0,0). Again, the realisations for A_2^* can be used as an example. Without imposing the origo constraint, the mean curve would have estimated the first measurements very well, providing small residuals, and reducing their impact when quantifying the uncertainty. For the two other derivatives illustrated, this tendency is not equally evident, due to the fact that the measurement for low velocities are scattered on both sides of the mean polynomial curve. However, the origo constraint is not seen to increase the accuracy of the prediction in the range of critical speed. Thus, in this case study the imposing of a constraint on one part of the curve, is undesirable for estimation of values in other ranges of reduced speed.

Realising this, a natural assumption would be that extreme values of reduced velocity are a result of extreme realisations of some of the flutter derivatives. To investigate this, random variables for a sample of low critical speeds in the 4 mode combination of case 1 were saved. Their respective curves were then plotted against the measurements similar to fig. 7.2-7.3. The results were inconclusive. For all of the derivatives thought to be significant, the realisations was distributed comparingly to the grey curves in fig. 7.2-7.3.

It thus seems as it is a combination of unfavourable realisations that provides the extreme values of critical speed.

These considerations provide good reasons to doubt the results generated from case 1. However, from the basic modelling assumptions, it was immediately evident that the results from case 1 would be more conservative than the results of case 2. The uncertainty of a predicted response is naturally larger than the uncertainty of the mean response. Because the current variance modelling in case 1 was seen not to predict uncertainty at critical speed well, an important question still remains unanswered: Is it correct to model the uncertainty based upon the mean response, or would an alternative residual uncertainty modelling have provided more correct results?

In order to answer this, it should be realised that the measurements are discrete data samplings on a section model, while the aim of uncertainty modelling is to fit curves with correct variance through the measured data points. In the current modelling of case 1, the extremal realisations of such curves are associated with the probability that one extremal *measurement* is recorded during the test campaign, which is a much higher value, implying that the variance of the curves in case 1 is too high.

Now, it could be argued that the modelling should only be concerned with the scatter of measurements at critical speed, and the curves being tools that help to predict the scatter at critical speed. However, this assumption would imply that the aerodynamical behaviour of the bridge for different wind speeds is independent, as the measurements imply. This is physically most unlikely, and the measurements should thus be interpreted as attempts to construct a mean curve, implying that the modelling of case 2 is correct.

7.3 Comparison of the case 2 results

Considering the critical speed parameters for case 2 modelling, which is seen in tab. 6.4, two tendencies stand out. Firstly, the mean of the distributions is reduced when more modes are included. Secondly, the variance is increased when more modes are included, with an exception for the 4-mode combination. Because of the large simulation numbers involved, the results are statistically significant. However, the differences are relatively small. For the mode combinations chosen in this study, the intuitive assumption would be that the failure probability increases with the number of included modes. To see if the calculations support this hypothesis, a comparison is appropriate.

For the 3- and 11-mode combinations, fig. 6.13 og fig 6.17 suggest that the solutions are not converging, and that more simulations would have been advantageous, thus, making the validity of the present results questionable. However, for both of these combinations, most of the calculations suggest that the probability of failure is well below $10 \cdot 10^{-10}$, and there is no evidence to support that the 11 mode combination has a higher probability of failure. For the 4- and 7-mode combinations, the calculated values are more stable for high simulation numbers. In the comparable range of N_{sim}, however, both of these combinations have higher failure probabilities than the 3- and 11-mode combinations. However, by varying the values of λ_M, it was observed that the differences within the same mode combination occasionally were larger than the deviation between different mode combinations. This is observed not only for low values of N_{sim}, but in the full range of simulation values. Thus, it is reasonable to treat also the results for the 4- and 7-mode

combinations with caution.

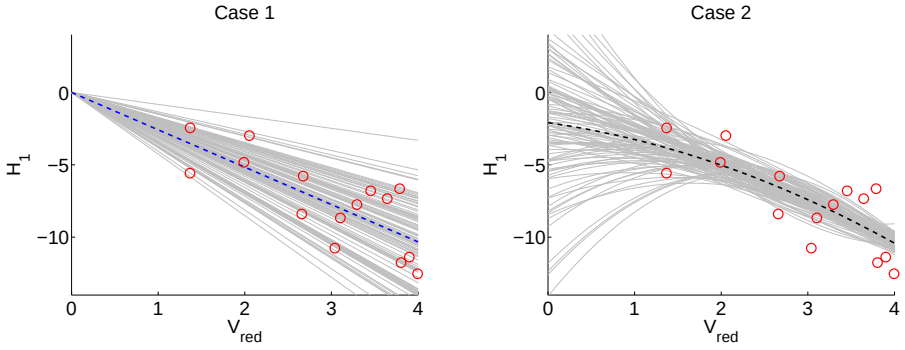

Figure 7.2: 100 realisations of H_1^* using the different models.

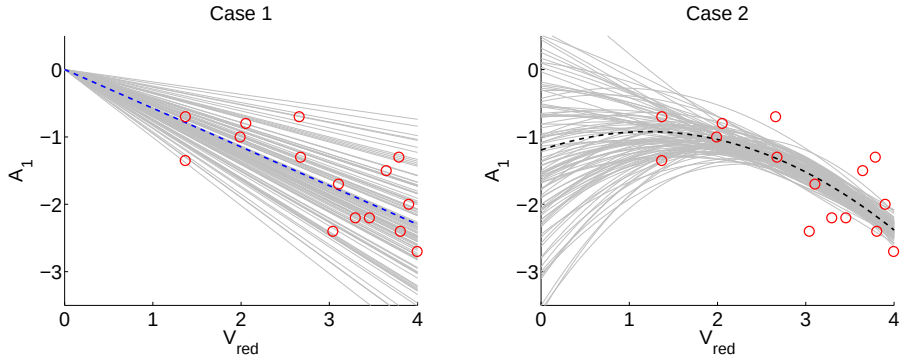

Figure 7.3: 100 realisations of A_1^* using the different models.

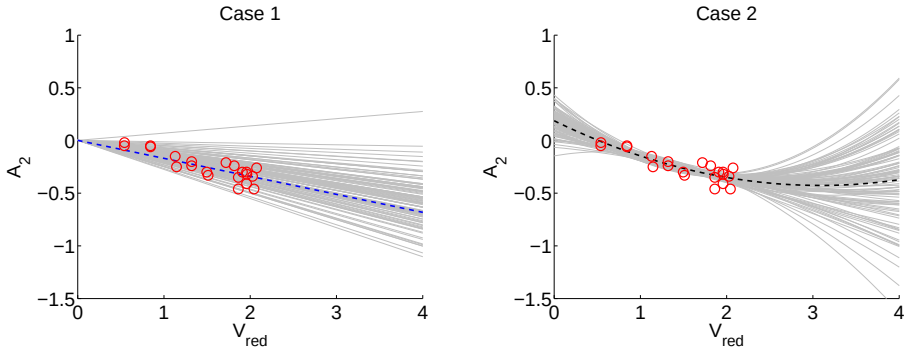

Figure 7.4: 100 realisations of A_2^* using the different models.

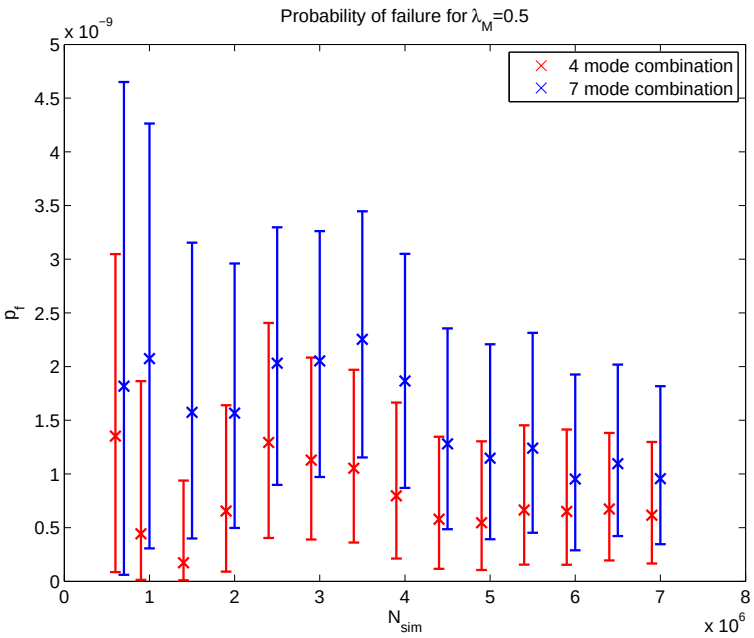

Figure 7.5: 11 mode combination: Failure probability and confidence intervals for different combinations of N_{sim} and λ.

In fig. 7.5-7.6, a comparison for the 4- and 7-mode combinations are made. For the first figure, it should be emphasized that other values of λ_M could make the picture look differently, and the same holds true for other N_{sim} values in the second figure. However, the tendency of mode combination 4 to take on slightly lower values is consistent with other configurations, which is in line with what to expect from reality. The difference of the distribution means is 0.57. However, in tab. 6.1 it was observed that the main contribution to this reduction is due to the effect of vertical mode 12. When correcting for the mean effect of mode 12, the difference between the values of failure probability is effectively halved. Assuming that some of the increased variance seen for the 7 mode distribution can be traced to mode 12, the contributions from horizontal modes to failure probability seem to be very small.

To assess this question with more accuracy, it would have been preferable to compare the 7-mode combination with a 5-mode combination including the 12th mode. Also, increasing the ammount of data would increase the validity of the results.

However, in the present study there is no evidence to suggest that horizontal mode effects impact the flutter limit of the Hardanger Bridge in terms of failure probability.

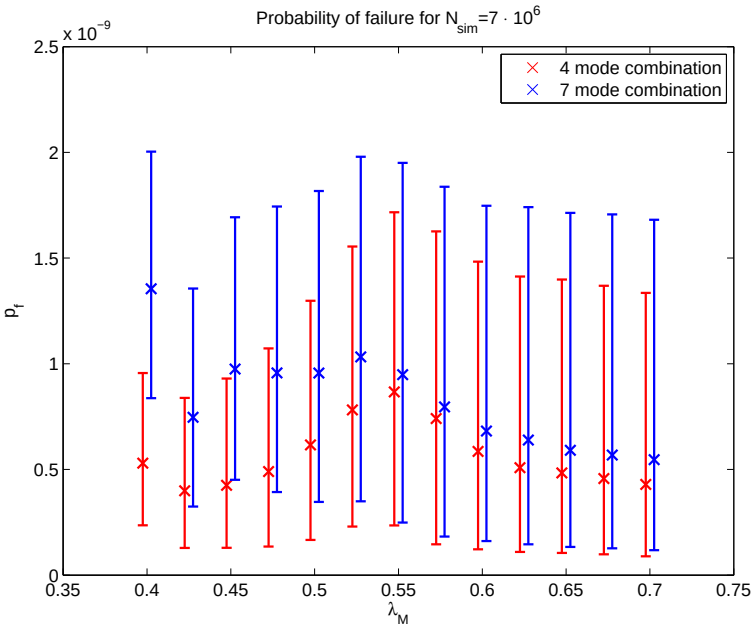

Figure 7.6: 11 mode combination: Failure probability and confidence intervals for different combinations of N_{sim} and λ.

7.4 Validity of the results

During the discussion in chapter 4, a number of uncertainties arising in the struggle to find critical speed for a bridge, was pointed out. Even though the discussion did not provide a full account of all the problems, it clarified that the field is still not fully understood, and that the results should be assessed with a critical eye. An evidence of uncertainty is provided in this study as well, as one of the proposed modelling methods for flutter derivatives turned out to be unsuitable. All of these complications must be taken into account at an early stage of the analysis. In this section however, only a discussion of the most important limitations that were seen during the last step of the analysis provided in this study, namely the enhanced Monte Carlo method, is included.

The enhanced method deals with inferences about the tail behaviour at extreme values of distributions. Here, traditional fitting procedures become useless, because the well-known distribution types fail to predict the tail behaviour. For example, using the mean and variance of the distribution of $M = V_{Cr} - V_S$ to construct a normal distribution would render $p_f = P(M \leq 0) \approx 10^{-30}$. In this case, it is even visually obvious that the estimated curve do not fit the tail of the distribution well. The same holds true for other distribution types. Thus, no basis for comparison is readily available to validate the results. In [22, 30], the enhanced method is applied to example problems where the log ratio $m_{\log}$ ranged from -0.85 to 0.4. ($m_{\log} = \log N_{sim} + \log p_f$ was introduced in sec. 3.8.1 to the convenience of the author). Here, it is applied to a problem where the ratio is predicted to

be between -1.8 and -3.2. Thus, it is not immediately evident that the method performs as well as in the examples in the papers published by Næss.

To investigate further, a basic investigation was made on a normal distribution, for which the probability of failure can easily be obtained. Specifically, M was distributed with $N(6.3, 1)$, with $P(M \leq 0) = \Phi(-6.3) \approx 1.5 \cdot 10^{-10}$. The results, using $\lambda_M = 0.5 - 0.6$, are depicted in fig. 7.7

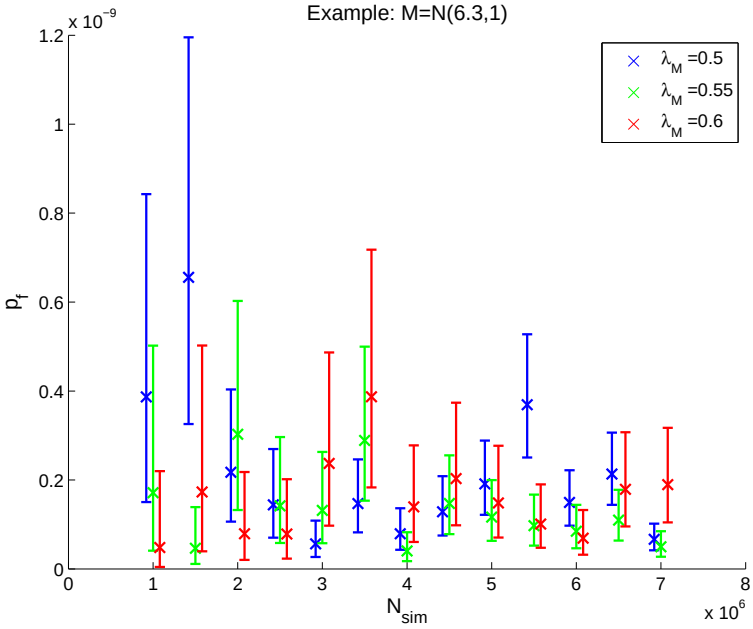

Figure 7.7: Example: Failure probability and confidence intervals for a normal distribution with $\mu = 6.3, \sigma = 1$ and theoretical $p_f = 1.49 \cdot 10^{-10}$.

The figure provides more narrow confidence intervals than noted in the study of the Hardanger Bridge. Also, the probabilities predicted are in good accordance with the theoretical result, especially for high values. On the other hand, some outliers points out, in good accordance with the results in chapter 6. It should be noted that the method was developed based on assumptions which hold true for normal distributions, making it more probable that these distributions are fitted well. Even so, the example suggests that the method *can* be applied for low-value probabilities as well.

For the different mode combinations of case 2, the calculated failure probabilities take on values varying from $0.7 \cdot 10^{-10}$ to $25 \cdot 10^{-10}$, a factor of about 35. The realisations of the confidence intervals vary from 0 to $45 \cdot 10^{-}10$. A zero value implies that the regression of the lower confidence curve failed, which was the situation for several of the calculations. In most cases, this did not affect the calculations of failure probability. Consequently, also such calculations were included in the results. For design purposes, the lower confidence interval is not of significant importance.

More worthwile to note was the scatter of results when applying different values of

λ_M. The experiences from this study suggest that one main concern is to find the correct value to apply. In fig. 7.8, an example of a wrong choice is illustrated. The estimation is based on a curve that clearly has diverged, because the number of data samples in the tail of the distribution is low. For the failure probability this is not crucial, because these data points are provided with a low weight; however, the result is less reliable than desired. On the other hand, if a low value of λ_M is used, the result is uncertain because of the long extrapolation path. The correct choice should be somewhere in between, for the present study values between 0.5 and 0.6 were often seen to provide reasonably consistent results. However, the effect of the choice of value is presently not fully understood.

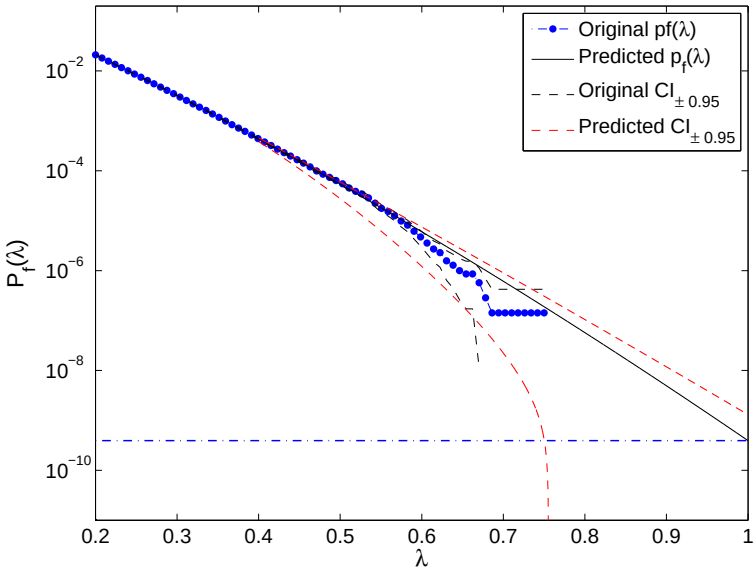

Figure 7.8: Typical extrapolation curves for the enhanced Monte Carlo method. Wrong choice of λ_M.

Chapter 8

Conclusion

In the present study, a reliability analysis of the Hardanger Bridge has been performed, using the multi mode flutter criteria as the limit state. The analysis was separated in three main parts. Firstly, the uncertainty of flutter derivatives was modelled. Secondly, a probabilistic analysis of the critical flutter speed was made. Thirdly, the results were compared with the stochastic distribution of the extreme 10-min mean wind value at the construction site.

According to the calculations, the reliability of the bridge was found to be high. Using the most reliable results, the safety index against flutter during one year was found as $\beta \in \{5.84 - 6.36\}$ or $\beta = 6.10 \pm 0.26$. The values correspond to failure probabilities in the range of $p_f \in \{1 \cdot 10^{-10} - 25 \cdot 10^{-10}\}$. However, the study also revealed that not all uncertainties were accounted for when these numbers was found. In the study, there was found no evidence to suggest that inclusion of horizontal modes had significant effect on the flutter limit of the bridge, neither in terms of critical speed nor in terms of failure probability. The confidence intervals constructed by the applied method were seen not to be "true" limits of confidence. Rather, they must be considered as qualitative measures of uncertainty connected to the calculations.

While previous stability assessments of the Hardanger Bridge used quasi-static load coefficients to determine horizontal load effects, experimentally determined horizontal derivatives was available for the present study.

In order to apply the measurements from the test series, and take into account the inherent uncertainty, it was necessary to model the derivatives as continuous, stochastic variables. Two different suggestions were made. In Case 1 the uncertainty was modelled by taking the variance of the *residual* terms into account. In addition each polynomial fitting curve was forced to pass through origo, to acknowledge the fact that no in-wind effects are present in still-air. In Case 2 uncertainty was modelled based on the variance of the *mean* responce.

The study revealed that both modelling conditions in Case 1 was based on wrong assumptions, and therefore, the results from this case have very limited validity. The study justifies that case 2 modelling is more in accordance with the nature of self-induced forces.

In addition to the modelled uncertainty of flutter derivatives, there are a large number of uncertainties connected to critical speed calculations that is not taken into account in the present mathematical analysis. Among these, but not limited to, are the sensitivity to changes of eigen-frequencies and damping coefficients, the assumption of independence between angle of incidence and flutter derivative, the frequency tuning choices connected to section model testing, as well as the assumption of full spatial coherence of the wind vector along the bridge.

A deterministic analysis to find critical speed suggested proceeding with 4 mode combinations, the two last including 2 and 6 horizontal modes, respectively.

The probabilistic analysis of critical wind speed was performed by applying the deterministic flutter criteria on a number of randomly generated input vectors distributed according to the case 2 modelling of flutter derivatives. For each of the 4 mode combinations, either $3 \cdot 10^6$ or $7 \cdot 10^6$ simulations was performed, the numbers chosen due to time limitations. For all combinations, the resulting critical speed distributions had similar characteristics, with the expected variation both on mean response and standard deviation. The mode combination including 7 modes was distributed with $\mu = 79.60$ m/s and $\sigma = 2.64 m/s$.

An enhanced Monte Carlo simulation technique was presented. Using the limit state $M = \sqrt{V_{Cr}} - \sqrt{V_S} = 0$, the method was applied on the calculated distributions of critical speed, varying the number of simulations and λ_M, one of the key parameters used in the method. The calculations with $N_{sim} = 7 \cdot 10^6$ was found to be of most interest, because a stabilizing tendency was seen when increasing the number of simulations beyond $5 - 5.5 \cdot 10^6$. Notably, a slightly higher failure probability was seen for the 7 mode combination compared to the 4 mode combination, which was as expected. However, due to the fact that vertical mode 12 was included in the first combination, while not in the latter, it is difficult to conclude that horizontal modes have impact on failure probability.

The solutions were seen to rest heavily on the choice of λ_M. The variation within each mode combination due to changes of λ_M, was often seen to be more dominant than the variation between mode combinations. To increase the accuracy of results, a conscious choice of λ_M is in order. Increasing the number of simulations even further would also be an aid to increase accuracy. However, judging on the calculated safety levels, the method seems to provide a level of accuracy that is appropriate, compared to the total level of uncertainty that is associated with flutter speed calculations.

8.1 Limitations and further work

In this study, the changes in the calculated reliability level of the Hardanger Bridge due to the choice of different mode combinations were studied. The extent to which statistically significant conclusions could be made was limited because of the numbers of simulations available, as well as the understanding of the variation due to different choices of λ_M.

It would be of interest to assess which effect the uncertainty of isolated flutter derivatives, as well as other uncertain variables, has upon the failure probability. Also, the impact of possible measurement outliers from the testing campaign, is not taken into account here.

To increase the accuracy of the calculations, even higher simulation numbers would have been advantageous. However, this would soon imply an unreasonable demand on

computational efforts. Possibly, the enhanced method could be combined with some form of importance sampling function. Also, it has been suggested to use response surface methodology to estimate the critical speed as an explicit function of flutter derivatives, which would increase calculation speed considerably. The critical point of such a method would be to ensure that the tail behaviour is estimated well by the response surface. Such methods are currently being investigated at NTNU.

Bibliography

[1] Statens Vegvesen. Brua, http://www.vegvesen.no/vegprosjekter/hardangerbrua/brua, June 12 2014.

[2] E.N.Strømmen. *Theory of Bridge Aerodynamics*. Springer, 2010.

[3] R.E.Melchers. *Structural Reliability Analysis and Prediction*. Wiley, 2nd edition, 1999.

[4] G.Diana et.al. Turbulence effect on flutter velocity in long span suspended bridges. *Journal of Wind Engineering and Industrial Aerodynamics*, (48):329–342, 1993.

[5] R.H.Scanlan and N.P.Jones. Stochastic aspects of bridge deck aeroelasticity under turbulent flow. *Probabilistic Engineering Mechanics*, 6(3-4):129–133, September-December 1991.

[6] S.O.Hansen et al. The hardanger bridge. static and dynamic wind tunnel tests with a section model.

[7] R.H.Scanlan and J.J.Tomko. Airfoil and bridge deck flutter derivatives. *Journal of the Engineering Mechanics Division*, 97(6):1717–1737, November-December 1971.

[8] O.A.Øiseth. *Dynamic behaviour of cable-supported bridges subjected to strong natural wind*. PhD thesis, NTNU, November 2011.

[9] A.K.Chopra. *Dynamic of Structures - Theory and Applications to Earthquake Engineering*. Pearson Prentice Hall, 3rd edition, 2007.

[10] J.A.Jurado. *Bridge Aeroelasticity*. WIT Press, 2011.

[11] T.J.A. Agar. Aerodynamic flutter analysis of suspension bridges by a modal technique. *Engineering Structures*, 11(2):75–82, April 1989.

[12] Matsumoto et. al. Effects of aerodynamic interferences between heaving and torsional vibration of bridge decks: the case of tacoma narrows bridge. *Journal of Wind Engineering and Industrial Aerodynamics*, 91:1547–1557, 2003.

[13] T.Theodorsen. General theory of aerodynamic instability and the mechanism of flutter. *NACA report, Langley*, 1934.

[14] H.Katsuchi, N.Jones, and R.H.Scanlan. Multimode coupled flutter and buffeting analysis of the akashi-kaikyo bridge. *Journal of Structural Engineering*, 125(1):1547–1557, January 1999.

[15] L.Singh et.al. Identification of lateral flutter derivatives of bridge decks. *Journal of the Wind Engineering and Industrial Aerodynamics*, 60:81–89, 1996.

[16] T.H.Kvamstad. *Assessment of the flutter stability limit of the Hålogaland Bridge using a probabilistic approach*. NTNU, June 2011.

[17] E.Simiu. and R.H.Scanlan. *Theory of Bridge Aerodynamics*. Springer, 2010.

[18] C.Dyrbye and S.O.Hansen. *Wind loads on structures*. John Wiley & Sons, 1997.

[19] J.Schneider. *Introduction to Safety and Reliability of Structures*, volume 5 of *Structural Engineering Documents*. Zürich: International Association for Bridge and Structural Engineering, 2nd edition, 2006.

[20] T.Moan. *Structural Risk and Reliability Analysis*. Department of Marine Technology, NTNU, 2008.

[21] D.W.Marquardt. An algorithm for least-squares estimation of nonlinear parameters. *Journal of the Society for Industrial and Applied Mathematics*, 11(2):431–441, June 1963.

[22] A.Næss et.al. System reliability analysis by enhanced monte carlo simulation. *Structural Safety*, 31(5):349–355, September 2009.

[23] J.B.Jakobsen and H.Tanaka. Modelling uncertainties in prediction of aeroelastic bridge behaviour. *Journal of Wind Engineering and Industrial Aerodynamics*, (91):1485–1498, 2003.

[24] M.Bocciolone et.al. Wind measurements on the humber bridge and numerical simulations. *Journal of Wind Engineering and Industrial Aerodynamics*, (41-44):1393–1404, 1992.

[25] Standard Norge. Eurocode 1: Actions on structures, part 1-4: General actions - wind actions, September 2009.

[26] G.Diana et.al. Comparisons between wind tunnel tests on a full aeroelastic model of the proposed bridge over stretto di messina and numerical results. *Journal of Wind Engineering and Industrial Aerodynamics*, (54-55):101–113, 1995.

[27] T.Argentini et.al. Monte carlo analysis of total damping and flutter speed of a long span bridge: Effects of structural and aerodynamic uncertainties. *Journal of Wind Engineering and Industrial Aerodynamics*, 128:90–104, 2014.

[28] J.Cheng et.al. Flutter reliability analysis of suspension bridges. *Journal of Wind Engineering and Industrial Aerodynamics*, 93:757–775, 2005.

[29] Statens Vegvesen. Håndbok 185: Bruprosjektering, October 2009.

[30] M.Papadrakakis et.al. *Computational Methods in Stochastic Dynamics*, volume 2. Springer, 2013.

Appendices

Appendix A

Failure probabilities

Failure probability p_f					
$N_{sim} \backslash \lambda_M$	0.4	0.45	0.5	0.55	0.6
700000	3.7e-10	7e-10	1.5e-10	1.3e-10	1.2e-10
1000000	1.9e-10	1.6e-10	9e-11	5.7e-11	4.9e-11
1500000	2.5e-10	1.4e-10	7e-11	4.9e-11	4.5e-11
2000000	2.1e-10	2.9e-10	2.7e-10	2.2e-10	2.3e-10
2500000	2.7e-10	4.2e-10	3.1e-10	2.4e-10	2.1e-10
3000000	3.9e-10	6.8e-10	4.9e-10	3.1e-10	2.2e-10
Lower confidence limit $CI_{-0.95}$					
700000	2.4e-11	4.9e-11	3e-12	1e-12	-2.2e-15
1000000	9.4e-12	7.6e-12	3e-12	1.1e-12	-2.2e-15
1500000	3.7e-11	7.4e-12	3.7e-12	1.7e-12	9.6e-13
2000000	4.6e-11	4.9e-11	1.7e-11	6.8e-12	5e-12
2500000	5.7e-11	8.3e-11	2.4e-11	1.7e-11	1.2e-11
3000000	1.5e-10	2.7e-10	9.3e-11	2.3e-11	1.6e-11
Upper confidence limit $CI_{+0.95}$					
700000	1.3e-09	1.9e-09	1.4e-09	1.4e-09	1.4e-09
1000000	8.2e-10	9.7e-10	8.6e-10	7.8e-10	7.6e-10
1500000	7.3e-10	6.5e-10	5.6e-10	5.4e-10	5.7e-10
2000000	5.6e-10	7.7e-10	8.5e-10	8.6e-10	9.3e-10
2500000	6.9e-10	1e-09	9.9e-10	1e-09	1e-09
3000000	7.7e-10	1.2e-09	1.1e-09	1e-09	9.4e-10

Table A.1: 3 mode combination: Failure probabilities with lower and upper 95 % confidence limits. High values of N_{sim} and λ_M 0.45-0.55 provide the most reliable results.

Failure probability p_f							
0	0.4	0.45	0.5	0.55	0.6	0.65	0.7
700000	1.3e-09	1.4e-09	1.4e-09	1.5e-09	1.4e-09	1.4e-09	1.5e-09
1000000	1.4e-09	1e-09	4.4e-10	5.7e-10	4.5e-10	4.8e-10	6.1e-10
1500000	5.5e-10	2.8e-10	1.7e-10	3.5e-10	3.4e-10	3.8e-10	3.5e-10
2000000	2.2e-10	4.1e-10	6.5e-10	7.6e-10	6.8e-10	6.9e-10	5.9e-10
2500000	4e-10	1.1e-09	1.3e-09	1.3e-09	1.2e-09	1.2e-09	1e-09
3000000	3e-10	9.3e-10	1.1e-09	1.1e-09	9e-10	8.6e-10	6.5e-10
3500000	3.8e-10	8.1e-10	1.1e-09	1e-09	8.7e-10	8.2e-10	5.8e-10
4000000	4.4e-10	5.4e-10	8e-10	7.8e-10	5.9e-10	4.6e-10	3.8e-10
4500000	4.1e-10	3.2e-10	5.8e-10	7.5e-10	5.6e-10	4.3e-10	3.7e-10
5000000	4.6e-10	3.4e-10	5.5e-10	7.3e-10	4.9e-10	4.2e-10	3.6e-10
5500000	4.8e-10	4.1e-10	6.6e-10	9.1e-10	5.9e-10	4.9e-10	4.3e-10
6000000	5.2e-10	4.3e-10	6.5e-10	9.3e-10	6.4e-10	5.2e-10	4.6e-10
6500000	4.6e-10	3.8e-10	6.7e-10	9.4e-10	6.4e-10	5e-10	4.4e-10
7000000	5.3e-10	4.3e-10	6.2e-10	8.7e-10	5.9e-10	4.8e-10	4.3e-10
Lower confidence limit $CI_{-0.95}$							
700000	4.2e-10	3e-10	8.5e-11	2e-11	1.1e-11	1.2e-14	1.9e-13
1000000	5.6e-10	2.3e-10	1.4e-11	1.1e-11	6.1e-12	6.3e-15	1.4e-13
1500000	1.6e-10	1.7e-11	9.5e-12	9.5e-12	6.5e-12	5.7e-15	1.3e-13
2000000	3.2e-11	5.9e-11	9.1e-11	4.6e-11	2.6e-11	2.1e-11	1e-13
2500000	1e-10	3.9e-10	4e-10	2.5e-10	8.2e-11	7.4e-11	1.5e-13
3000000	8.2e-11	3.8e-10	3.9e-10	2.1e-10	6.3e-11	5.7e-11	1.2e-13
3500000	1.2e-10	3.1e-10	3.6e-10	2.2e-10	7.5e-11	6.6e-11	1.2e-13
4000000	1.5e-10	1.4e-10	2.1e-10	1.2e-10	6.8e-11	5.9e-11	1.2e-13
4500000	1.4e-10	7.3e-11	1.2e-10	1.3e-10	7e-11	5.9e-11	1.4e-13
5000000	1.6e-10	8.7e-11	1.1e-10	1.2e-10	8e-11	6.8e-11	1.5e-13
5500000	1.8e-10	1.1e-10	1.6e-10	2e-10	1.1e-10	9.2e-11	1.7e-13
6000000	2.1e-10	1.2e-10	1.5e-10	2.3e-10	1.2e-10	1.1e-10	1.8e-13
6500000	1.9e-10	1.1e-10	2e-10	2.7e-10	1.2e-10	1e-10	8.6e-11
7000000	2.4e-10	1.3e-10	1.7e-10	2.4e-10	1.2e-10	1e-10	8.9e-11
Upper confidence limit $CI_{+0.95}$							
700000	2.5e-09	3e-09	3e-09	3.5e-09	3.6e-09	3.2e-09	3.8e-09
1000000	2.4e-09	2.3e-09	1.9e-09	2.2e-09	2.2e-09	2.3e-09	2.5e-09
1500000	1.2e-09	1e-09	9.4e-10	1.4e-09	1.5e-09	1.6e-09	1.6e-09
2000000	6.7e-10	1.1e-09	1.6e-09	1.9e-09	1.9e-09	2e-09	1.9e-09
2500000	9.5e-10	2e-09	2.4e-09	2.6e-09	2.6e-09	2.6e-09	2.5e-09
3000000	7.2e-10	1.7e-09	2.1e-09	2.1e-09	2.1e-09	2.1e-09	1.9e-09
3500000	8.3e-10	1.5e-09	2e-09	2.1e-09	2e-09	2e-09	1.8e-09
4000000	9.2e-10	1.2e-09	1.7e-09	1.8e-09	1.7e-09	1.6e-09	1.5e-09
4500000	8.6e-10	8.5e-10	1.3e-09	1.7e-09	1.6e-09	1.5e-09	1.4e-09
5000000	9.2e-10	8.7e-10	1.3e-09	1.7e-09	1.5e-09	1.4e-09	1.3e-09
5500000	9.4e-10	9.9e-10	1.5e-09	1.9e-09	1.6e-09	1.5e-09	1.5e-09
6000000	9.8e-10	9.8e-10	1.4e-09	1.9e-09	1.6e-09	1.5e-09	1.5e-09
6500000	8.7e-10	8.7e-10	1.4e-09	1.8e-09	1.6e-09	1.4e-09	1.4e-09
7000000	9.6e-10	9.3e-10	1.3e-09	1.7e-09	1.5e-09	1.4e-09	1.3e-09

Table A.2: 4 mode combination: Failure probabilities with lower and upper 95 % confidence limits. High values of N_{sim} and λ_M 0.5-0.6 provide the most reliable results.

Failure probability p_f							
0	0.4	0.45	0.5	0.55	0.6	0.65	0.7
700000	2.1e-09	1.5e-09	1.8e-09	1.4e-09	1.4e-09	1.5e-09	1.8e-09
1000000	2.3e-09	2.1e-09	2.1e-09	1.2e-09	7.4e-10	6.7e-10	9.8e-10
1500000	1.8e-09	1.6e-09	1.6e-09	1.1e-09	8.3e-10	7.2e-10	7.5e-10
2000000	1.9e-09	1.6e-09	1.6e-09	1.2e-09	1e-09	8.3e-10	7.8e-10
2500000	2.1e-09	2e-09	2e-09	1.8e-09	1.6e-09	1.3e-09	1.2e-09
3000000	1.8e-09	1.8e-09	2.1e-09	1.8e-09	1.4e-09	1e-09	8.6e-10
3500000	2e-09	2.1e-09	2.3e-09	2e-09	1.6e-09	1.1e-09	9.1e-10
4000000	1.9e-09	1.9e-09	1.9e-09	1.5e-09	9.4e-10	6.5e-10	6e-10
4500000	1.3e-09	1.3e-09	1.3e-09	1.2e-09	8.3e-10	5.8e-10	5.4e-10
5000000	1.1e-09	1.2e-09	1.1e-09	9.9e-10	6.5e-10	5.3e-10	5.1e-10
5500000	1.3e-09	1.3e-09	1.2e-09	1.2e-09	8.1e-10	7.1e-10	6.5e-10
6000000	1.3e-09	1e-09	9.5e-10	9.1e-10	7e-10	6.1e-10	5.8e-10
6500000	1.5e-09	1e-09	1.1e-09	1.1e-09	7.9e-10	6.7e-10	6.1e-10
7000000	1.4e-09	9.7e-10	9.6e-10	9.5e-10	6.8e-10	5.9e-10	5.5e-10
Lower confidence limit $CI_{-0.95}$							
700000	6.3e-10	1.3e-10	6.1e-11	3.3e-11	1.8e-11	3.2e-14	2.3e-13
1000000	1.1e-09	5.9e-10	3.1e-10	5.5e-11	3.1e-11	3.1e-14	2.6e-13
1500000	9.2e-10	6e-10	4e-10	5e-11	3e-11	6e-14	2.1e-13
2000000	1.1e-09	7.2e-10	5e-10	1.2e-10	5.1e-11	3.8e-11	2e-13
2500000	1.3e-09	1e-09	9e-10	5.2e-10	2.1e-10	8.3e-11	2.1e-13
3000000	1.2e-09	9.5e-10	9.7e-10	5.5e-10	1.7e-10	8.7e-11	2.3e-13
3500000	1.3e-09	1.2e-09	1.2e-09	7.7e-10	2.8e-10	1.3e-10	2.6e-13
4000000	1.2e-09	1.1e-09	8.7e-10	4.5e-10	1.4e-10	1.1e-10	2.5e-13
4500000	7.3e-10	6.4e-10	4.9e-10	3e-10	1.2e-10	9.5e-11	3.1e-13
5000000	6.1e-10	5.1e-10	3.9e-10	1.9e-10	1.3e-10	1e-10	8.9e-11
5500000	7.6e-10	6.2e-10	4.5e-10	2.7e-10	1.7e-10	1.4e-10	1.2e-10
6000000	7.7e-10	4.2e-10	2.9e-10	2e-10	1.6e-10	1.3e-10	1.1e-10
6500000	9.8e-10	4.7e-10	4.2e-10	3.4e-10	1.7e-10	1.4e-10	1.3e-10
7000000	8.4e-10	4.5e-10	3.5e-10	2.5e-10	1.6e-10	1.3e-10	1.2e-10
Upper confidence limit $CI_{+0.95}$							
700000	4.1e-09	4e-09	4.7e-09	4.6e-09	4.8e-09	4.9e-09	5e-09
1000000	3.8e-09	3.9e-09	4.3e-09	4e-09	3.7e-09	3.7e-09	4e-09
1500000	2.9e-09	2.9e-09	3.2e-09	2.9e-09	2.8e-09	2.7e-09	2.8e-09
2000000	2.9e-09	2.8e-09	3e-09	2.8e-09	2.8e-09	2.6e-09	2.6e-09
2500000	3e-09	3e-09	3.3e-09	3.3e-09	3.2e-09	3.1e-09	3e-09
3000000	2.7e-09	2.8e-09	3.3e-09	3.2e-09	2.9e-09	2.6e-09	2.6e-09
3500000	2.8e-09	3.1e-09	3.4e-09	3.4e-09	3.1e-09	2.8e-09	2.7e-09
4000000	2.7e-09	2.9e-09	3.1e-09	2.9e-09	2.4e-09	2.1e-09	2.1e-09
4500000	2e-09	2.2e-09	2.4e-09	2.4e-09	2.1e-09	1.9e-09	1.9e-09
5000000	1.9e-09	2e-09	2.2e-09	2.2e-09	1.9e-09	1.8e-09	1.8e-09
5500000	2.1e-09	2.2e-09	2.3e-09	2.4e-09	2.1e-09	2.1e-09	2.1e-09
6000000	2.1e-09	1.8e-09	1.9e-09	2e-09	1.9e-09	1.9e-09	1.9e-09
6500000	2.2e-09	1.8e-09	2e-09	2.2e-09	2e-09	1.9e-09	1.9e-09
7000000	2e-09	1.7e-09	1.8e-09	2e-09	1.7e-09	1.7e-09	1.7e-09

Table A.3: 7 mode combination: Failure probabilities with lower and upper 95 % confidence limits. High values of N_{sim} and λ_M 0.5-0.6 provide the most reliable results.

Failure probability p_f					
0	0.4	0.45	0.5	0.55	0.6
700000	2.5e-10	1.6e-10	5.2e-10	3e-10	2.9e-10
1000000	3.6e-10	2e-10	2.1e-10	1.6e-10	1.6e-10
1500000	3.5e-10	8.5e-11	1.1e-10	9.3e-11	9.5e-11
2000000	2.5e-10	1.7e-10	2.6e-10	1.9e-10	1.7e-10
2500000	3e-10	6.5e-10	1.1e-09	7.7e-10	6.1e-10
3000000	3.9e-10	3.8e-10	6e-10	3.3e-10	2.7e-10
Lower confidence limit $CI_{-0.95}$					
700000	1.4e-11	9.4e-12	1.1e-11	5.5e-12	2.3e-12
1000000	2.6e-11	1.6e-11	1.1e-11	5.8e-12	3e-12
1500000	4.2e-11	1.5e-11	1.1e-11	6.3e-12	3.7e-12
2000000	3.8e-11	2.6e-11	2.5e-11	1.7e-11	1.1e-11
2500000	6.7e-11	1.6e-10	3e-10	6.5e-11	3.9e-11
3000000	9.9e-11	7.2e-11	8e-11	4.5e-11	3.2e-11
Upper confidence limit $CI_{+0.95}$					
700000	1.3e-09	1.4e-09	2.6e-09	2.5e-09	2.6e-09
1000000	1.4e-09	1.2e-09	1.5e-09	1.5e-09	1.6e-09
1500000	1.2e-09	6.3e-10	8.2e-10	8.8e-10	1e-09
2000000	7.8e-10	7.7e-10	1.1e-09	1.1e-09	1.2e-09
2500000	7.9e-10	1.5e-09	2.3e-09	2.1e-09	2e-09
3000000	9.4e-10	1.1e-09	1.6e-09	1.3e-09	1.3e-09

Table A.4: 11 mode combination: Failure probabilities with lower and upper 95 % confidence limits. High values of N_{sim} and λ_M 0.45-0.55 provide the most reliable results.

Appendix B

Aerodynamic derivatives

	β_{2i}	β_{1i}	β_{0i}
P_1^*	-0.00	-0.53	0.00
P_2^*	0.00	-0.06	0.00
P_3^*	-0.00	-0.05	-0.14
P_4^*	-0.00	-0.46	0.24
P_5^*	0.00	-0.17	0.00
P_6^*	-0.00	0.19	-0.11
H_1^*	0.00	-2.58	0.00
H_2^*	0.00	0.42	0.00
H_3^*	-0.00	0.29	2.08
H_4^*	0.01	-0.92	0.16
H_5^*	0.01	1.70	0.00
H_6^*	0.01	0.31	0.00
A_1^*	0.00	-0.57	0.00
A_2^*	0.00	-0.17	0.00
A_3^*	-0.00	0.18	0.57
A_4^*	0.00	-0.04	-0.04
A_5^*	-0.01	0.18	0.00
A_6^*	-0.00	-0.48	0.05

Table B.1: Case 1: Coeff. of polynomials, $X_i^* = \beta_{2i} \cdot V_{red}^2 + \beta_{1i} \cdot V_{red} + \beta_{0i}$.

	β_{2i}	β_{1i}	β_{0i}
P_1^*	0.10	-0.89	0.15
P_2^*	0.02	-0.06	-0.01
P_3^*	-0.13	0.14	-0.20
P_4^*	-3.21	3.85	-1.06
P_5^*	0.55	-0.58	0.07
P_6^*	-0.18	0.28	-0.12
H_1^*	-2.09	-0.85	-0.31
H_2^*	0.39	-0.11	0.17
H_3^*	-0.53	1.11	1.80
H_4^*	2.72	-2.67	0.42
H_5^*	-15.81	23.95	-6.78
H_6^*	7.11	-8.57	2.53
A_1^*	-1.20	0.45	-0.19
A_2^*	0.19	-0.40	0.06
A_3^*	-0.06	0.12	0.64
A_4^*	1.91	-1.36	0.17
A_5^*	-3.94	5.24	-1.47
A_6^*	-0.45	-0.00	-0.07

Table B.2: Case 2: Coeff. of polynomials, $X_i^* = \beta_{2i} \cdot V_{red}^2 + \beta_{1i} \cdot V_{red} + \beta_{0i}$.

P_1	P_2	P_3	P_4	P_5	P_6	H_1	H_2	H_3	H_4	H_5	H_6	A_1	A_2	A_3	A_4	A_5	A_6
-0.02	0.00	-0.02	-0.10	0.00	-0.00	0.00	0.02	-0.04	0.07	-0.06	0.34	0.00	0.02	-0.03	0.02	-0.07	-0.02

Table B.3: Mean values of scaled residuals, Case 1.

	P_1	P_2	P_3	P_4	P_5	P_6	H_1	H_2	H_3	H_4	H_5	H_6	A_1	A_2	A_3	A_4	A_5	A_6
P_1	0.13	-0.01	-0.00	-0.00	0.00	0.01	-0.05	-0.01	-0.03	-0.00	0.10	0.47	0.00	-0.00	0.00	0.01	0.12	-0.03
P_2	-0.01	0.00	-0.00	-0.00	0.00	-0.00	-0.00	0.00	0.00	-0.00	-0.00	-0.01	0.00	0.00	-0.00	-0.00	-0.00	0.00
P_3	-0.00	-0.00	0.00	0.02	-0.00	0.00	-0.00	0.00	0.01	-0.01	0.02	-0.05	0.00	-0.00	0.00	-0.01	0.01	0.00
P_4	-0.00	-0.00	0.02	0.24	0.00	0.00	0.05	-0.00	0.05	-0.16	0.62	-0.66	0.03	-0.01	0.02	-0.05	0.15	0.01
P_5	0.00	0.00	-0.00	0.00	0.01	0.00	0.00	0.00	-0.00	-0.01	-0.04	-0.02	0.01	0.00	-0.00	-0.00	-0.00	-0.00
P_6	0.01	-0.00	0.00	0.00	0.00	0.00	0.00	0.00	-0.00	-0.00	-0.00	0.00	0.00	-0.00	0.00	-0.00	0.01	-0.00
H_1	-0.05	-0.00	-0.00	0.05	0.00	0.00	0.40	-0.00	0.04	-0.07	0.46	-0.90	0.06	-0.00	-0.00	-0.00	0.06	-0.04
H_2	-0.01	0.00	0.00	-0.00	0.00	0.00	-0.00	0.04	-0.01	-0.01	-0.30	0.04	0.01	0.01	-0.00	-0.00	-0.06	0.00
H_3	-0.03	0.00	0.01	0.05	-0.00	-0.00	0.04	-0.01	0.04	-0.04	0.15	-0.34	0.00	-0.01	0.01	-0.02	0.01	0.01
H_4	-0.00	-0.00	-0.01	-0.16	-0.01	-0.00	-0.07	-0.01	-0.04	0.13	-0.30	0.47	-0.03	0.01	-0.02	0.04	-0.10	0.00
H_5	0.10	-0.00	0.02	0.62	-0.04	-0.00	0.46	-0.30	0.15	-0.30	8.17	-3.31	0.08	-0.05	0.07	-0.12	1.41	-0.07
H_6	0.47	-0.01	-0.05	-0.66	-0.02	0.00	-0.90	0.04	-0.34	0.47	-3.31	5.82	-0.20	0.04	-0.08	0.18	-0.32	-0.03
A_1	0.00	0.00	0.00	0.03	0.01	0.00	0.06	0.01	0.00	-0.03	0.08	-0.20	0.03	0.00	-0.00	-0.00	0.02	-0.01
A_2	-0.00	0.00	-0.00	-0.01	0.00	-0.00	-0.00	0.01	-0.01	0.01	-0.05	0.04	0.00	0.00	-0.00	0.00	-0.02	-0.00
A_3	0.00	-0.00	0.00	0.02	-0.00	0.00	-0.00	-0.00	0.01	-0.02	0.07	-0.08	-0.00	-0.00	0.01	-0.01	0.02	0.00
A_4	0.01	-0.00	-0.01	-0.05	-0.00	-0.00	-0.00	-0.00	-0.02	0.04	-0.12	0.18	-0.00	0.00	-0.01	0.01	-0.02	-0.01
A_5	0.12	-0.00	0.01	0.15	-0.00	0.01	0.06	-0.06	0.01	-0.10	1.41	-0.32	0.02	-0.02	0.02	-0.02	0.43	-0.03
A_6	-0.03	0.00	0.00	0.01	-0.00	-0.00	-0.04	0.00	0.01	0.00	-0.07	-0.03	-0.01	-0.00	0.00	-0.01	-0.03	0.02

Table B.4: Covariance matrix of scaled residuals, Case 1.

Table B.5: Correlation matrix of scaled residuals, Case 1.

	P_1	P_2	P_3	P_4	P_5	P_6	H_1	H_2	H_3	H_4	H_5	H_6	A_1	A_2	A_3	A_4	A_5	A_6
P_1	1.00	-0.65	-0.10	-0.02	0.01	0.55	-0.23	-0.19	-0.46	-0.00	0.10	0.55	0.02	-0.14	0.01	0.27	0.51	-0.46
P_2	-0.65	1.00	-0.04	-0.00	0.49	-0.44	-0.00	0.26	0.09	-0.07	-0.03	-0.25	0.13	0.39	-0.24	-0.18	-0.30	0.16
P_3	-0.10	-0.04	1.00	0.81	-0.01	0.37	-0.09	0.06	0.52	-0.73	0.16	-0.41	0.11	-0.46	0.72	-0.86	0.28	0.43
P_4	-0.02	-0.00	0.81	1.00	0.11	0.31	0.15	-0.04	0.55	-0.87	0.44	-0.55	0.33	-0.36	0.60	-0.89	0.45	0.15
P_5	0.01	0.49	-0.01	0.11	1.00	0.21	0.05	0.24	-0.05	-0.25	-0.16	-0.08	0.45	0.25	-0.07	-0.11	-0.04	-0.25
P_6	0.55	-0.44	0.37	0.31	0.21	1.00	0.07	0.20	-0.05	-0.45	-0.05	0.01	0.36	-0.21	0.27	-0.21	0.38	-0.33
H_1	-0.23	-0.00	-0.09	0.15	0.05	0.07	1.00	-0.02	0.34	-0.28	0.25	-0.59	0.61	-0.11	-0.00	-0.04	0.15	-0.37
H_2	-0.19	0.26	0.06	-0.04	0.24	0.20	-0.02	1.00	-0.20	-0.17	-0.50	0.09	0.18	0.68	-0.29	-0.09	-0.47	0.02
H_3	-0.46	0.09	0.52	0.55	-0.05	-0.05	0.34	-0.20	1.00	-0.53	0.26	-0.72	0.08	-0.51	0.75	-0.66	0.08	0.24
H_4	-0.00	-0.07	-0.73	-0.87	-0.25	-0.45	-0.28	-0.17	-0.53	1.00	-0.29	0.54	-0.47	0.29	-0.62	0.82	-0.40	0.04
H_5	0.10	-0.03	0.16	0.44	-0.16	-0.05	0.25	-0.50	0.26	-0.29	1.00	-0.48	0.17	-0.28	0.30	-0.35	0.75	-0.16
H_6	0.55	-0.25	-0.41	-0.55	-0.08	0.01	-0.59	0.09	-0.72	0.54	-0.48	1.00	-0.51	0.29	-0.42	0.64	-0.20	-0.09
A_1	0.02	0.13	0.11	0.33	0.45	0.36	0.61	0.18	0.08	-0.47	0.17	-0.51	1.00	0.00	-0.03	-0.25	0.22	-0.31
A_2	-0.14	0.39	-0.46	-0.36	0.25	-0.21	-0.11	0.68	-0.51	0.29	-0.28	0.29	0.00	1.00	-0.72	0.26	-0.54	-0.22
A_3	0.01	-0.24	0.72	0.60	-0.07	0.27	-0.00	-0.29	0.75	-0.62	0.30	-0.42	-0.03	-0.72	1.00	-0.67	0.41	0.28
A_4	0.27	-0.18	-0.86	-0.89	-0.11	-0.21	-0.04	-0.09	-0.66	0.82	-0.35	0.64	-0.25	0.26	-0.67	1.00	-0.21	-0.28
A_5	0.51	-0.30	0.28	0.45	-0.04	0.38	0.15	-0.47	0.08	-0.40	0.75	-0.20	0.22	-0.54	0.41	-0.21	1.00	-0.25
A_6	-0.46	0.16	0.43	0.15	-0.25	-0.33	-0.37	0.02	0.24	0.04	-0.16	-0.09	-0.31	-0.22	0.28	-0.28	-0.25	1.00

	P_1	P_2	P_3	P_4	P_5	P_6	H_1	H_2	H_3	H_4	H_5	H_6	A_1	A_2	A_3	A_4	A_5	A_6
P_1	1.00	0.00	0.68	0.92	0.95	0.01	0.32	0.42	0.03	0.99	0.67	0.01	0.95	0.55	0.95	0.24	0.02	0.04
P_2	0.00	1.00	0.87	0.99	0.02	0.05	0.98	0.26	0.68	0.76	0.89	0.27	0.57	0.08	0.29	0.43	0.18	0.48
P_3	0.68	0.87	1.00	0.00	0.95	0.10	0.70	0.79	0.02	0.00	0.50	0.07	0.63	0.03	0.00	0.00	0.21	0.05
P_4	0.92	0.99	0.00	1.00	0.63	0.17	0.52	0.88	0.01	0.00	0.05	0.01	0.15	0.10	0.00	0.00	0.04	0.52
P_5	0.95	0.02	0.95	0.63	1.00	0.37	0.82	0.30	0.82	0.26	0.49	0.74	0.04	0.27	0.76	0.62	0.86	0.28
P_6	0.01	0.05	0.10	0.17	0.37	1.00	0.78	0.37	0.84	0.04	0.82	0.98	0.11	0.35	0.24	0.37	0.08	0.15
H_1	0.32	0.98	0.70	0.52	0.82	0.78	1.00	0.93	0.13	0.21	0.27	0.00	0.00	0.63	0.99	0.85	0.51	0.09
H_2	0.42	0.26	0.79	0.88	0.30	0.37	0.93	1.00	0.38	0.45	0.02	0.71	0.43	0.00	0.21	0.71	0.03	0.93
H_3	0.03	0.68	0.02	0.01	0.82	0.84	0.13	0.38	1.00	0.01	0.26	0.00	0.72	0.02	0.00	0.00	0.73	0.30
H_4	0.99	0.76	0.00	0.00	0.26	0.04	0.21	0.45	0.01	1.00	0.20	0.01	0.03	0.20	0.00	0.00	0.07	0.86
H_5	0.67	0.89	0.50	0.05	0.49	0.82	0.27	0.02	0.26	0.20	1.00	0.03	0.47	0.22	0.19	0.12	0.00	0.48
H_6	0.01	0.27	0.07	0.01	0.74	0.98	0.00	0.71	0.00	0.01	0.03	1.00	0.02	0.20	0.06	0.00	0.38	0.71
A_1	0.95	0.57	0.63	0.15	0.04	0.11	0.00	0.43	0.72	0.03	0.47	0.02	1.00	1.00	0.91	0.28	0.34	0.17
A_2	0.55	0.08	0.03	0.10	0.27	0.35	0.63	0.00	0.02	0.20	0.22	0.20	1.00	1.00	0.00	0.26	0.01	0.33
A_3	0.95	0.29	0.00	0.00	0.76	0.24	0.99	0.21	0.00	0.00	0.19	0.06	0.91	0.00	1.00	0.00	0.07	0.23
A_4	0.24	0.43	0.00	0.00	0.62	0.37	0.85	0.71	0.00	0.00	0.12	0.00	0.28	0.26	0.00	1.00	0.36	0.22
A_5	0.02	0.18	0.21	0.04	0.86	0.08	0.51	0.03	0.73	0.07	0.00	0.38	0.34	0.01	0.07	0.36	1.00	0.28
A_6	0.04	0.48	0.05	0.52	0.28	0.15	0.09	0.93	0.30	0.86	0.48	0.71	0.17	0.33	0.23	0.22	0.28	1.00

Table B.6: P-value matrix testing the hypothesis that there is some correlation between the residuals of flutter derivatives.

V	$V_{red,z}$	$V_{red,y}$	$V_{red,\phi}$	H_1^*	H_2^*	H_3^*	H_4^*	H_5^*	H_6^*
1.86	1.37	0.75	0.54	-5.58	0.41	0.64	1.04	-5.86	4.87
1.87	1.37	0.75	0.54	-2.45	0.12	0.63	0.68	3.32	1.93
2.80	1.99	1.15	0.84	-4.83	0.65	1.66	-3.34	3.66	1.51
2.83	2.05	1.15	0.84	-2.98	0.63	1.92	-0.67	1.40	-7.45
3.69	2.66	1.50	1.13	-8.40	0.67	2.56	-1.49	2.04	2.50
3.72	2.67	1.51	1.15	-5.78	0.17	3.26	-2.02	1.20	1.17
4.19	3.04	1.70	1.32	-10.76	0.47	3.90	-0.36	12.60	4.00
4.22	3.10	1.72	1.32	-8.67	0.39	3.74	0.62	5.72	-2.32
4.64	3.29	1.89	1.50	-7.75	0.61	5.36	-2.83	6.45	-1.15
4.67	3.45	1.91	1.51	-6.80	0.22	5.48	1.54	7.27	-1.43
5.18	3.64	2.12	1.72	-7.34	0.99	6.76	-3.67	4.05	2.07
5.40	3.80	2.23	1.81	-11.76	0.65	7.13	-1.60	5.56	-0.23
5.47	4.06	2.24	1.86	-11.51	0.18	8.34	3.14	5.96	-0.17
5.49	3.79	2.24	1.86	-6.65	1.39	7.68	-6.50	-1.99	1.45
5.60	4.17	2.31	1.91	-11.93	0.80	8.32	3.91	5.74	0.57
5.64	3.99	2.32	1.96	-12.53	0.73	9.00	-3.79	2.83	2.20
5.66	3.90	2.34	1.96	-11.38	0.84	8.90	-3.65	2.08	-0.03
5.72	4.19	2.35	1.96	-10.82	1.21	8.26	1.36	-2.52	3.49
5.82	4.11	2.41	2.03	-10.76	0.85	9.62	-3.07	4.38	-0.85
5.92	4.26	2.43	2.04	-9.74	0.68	8.88	-1.93	1.61	2.12
5.92	4.69	2.42	2.09	-14.37	1.38	11.23	3.96	2.76	3.42
6.01	4.33	2.48	2.07	-10.13	1.00	8.70	-0.82	3.22	-0.12
6.06	4.29	2.51	2.16	-9.94	1.10	10.97	-4.57	-0.69	0.65
6.10	4.45	2.52	2.14	-9.90	1.28	10.20	0.41	0.41	-0.54
6.10	4.53	2.55	2.20	-11.14	1.51	11.72	-2.95	-2.56	0.34
6.13	4.52	2.52	2.16	-10.71	0.03	10.36	0.47	6.46	1.96
6.25	4.73	2.56	2.27	-15.48	1.51	13.06	2.63	1.65	9.78
6.26	4.70	2.61	2.25	-13.68	0.95	12.01	3.02	-0.13	-0.54

Table B.7: Measurement of flutter derivatives $H_1^* - H_6^*$.

V	$V_{red,z}$	$V_{red,y}$	$V_{red,\phi}$	A_1^*	A_2^*	A_3^*	A_4^*	A_5^*	A_6^*	P_1^*	P_2^*	P_3^*	P_4^*	P_5^*	P_6^*
1.86	1.37	0.75	0.54	-1.35	-0.02	0.20	0.45	-1.34	-0.27	-0.48	-0.02	-0.10	-1.03	-0.25	-0.01
1.87	1.37	0.75	0.54	-0.70	-0.05	0.20	0.62	0.37	-0.60	0.02	-0.04	-0.13	-0.99	-0.27	0.03
2.80	1.99	1.15	0.84	-1.00	-0.05	0.49	-0.67	0.42	-0.82	-0.30	-0.04	-0.14	0.94	-0.20	0.05
2.83	2.05	1.15	0.84	-0.80	-0.06	0.48	-0.40	-1.52	-0.38	-2.09	0.00	-0.18	-0.59	-0.34	-0.29
3.69	2.66	1.50	1.13	-0.70	-0.15	0.80	-0.19	0.74	-0.56	-0.45	-0.06	-0.24	0.02	-0.47	-0.09
3.72	2.67	1.51	1.15	-1.30	-0.25	0.96	-0.44	-0.49	-0.82	-1.00	-0.06	-0.24	0.23	-0.44	-0.44
4.19	3.04	1.70	1.32	-2.40	-0.20	1.27	-1.06	1.17	-0.09	-1.01	-0.04	-0.27	-0.07	-0.83	-0.81
4.22	3.10	1.72	1.32	-1.70	-0.24	1.14	-0.16	1.45	-0.65	-1.25	-0.04	-0.31	-0.16	-0.06	-0.49
4.64	3.29	1.89	1.50	-2.20	-0.30	1.60	-0.64	1.46	-1.39	-0.88	-0.10	-0.33	0.14	-0.93	-0.19
4.67	3.45	1.91	1.51	-2.20	-0.33	1.53	0.02	1.41	-0.43	-1.38	-0.08	-0.39	0.37	-0.86	-0.82
5.18	3.64	2.12	1.72	-1.50	-0.21	2.04	-0.78	0.33	-0.39	-1.20	-0.09	-0.53	0.51	-0.26	-0.88
5.40	3.80	2.23	1.81	-2.40	-0.24	2.16	-2.02	-0.11	-0.89	-1.23	-0.10	-0.51	0.32	-0.83	-1.00
5.47	4.06	2.24	1.86	-2.30	-0.46	2.41	-0.75	0.94	-0.50	-0.69	-0.13	-0.65	0.39	-0.86	-1.23
5.49	3.79	2.24	1.86	-1.30	-0.35	2.40	-0.39	1.22	-1.45	-0.59	-0.12	-0.50	-0.53	-0.58	-0.11
5.60	4.17	2.31	1.91	-3.30	-0.30	2.55	-1.04	0.00	-0.58	-1.06	-0.19	-0.59	0.24	-1.32	-1.03
5.64	3.99	2.32	1.96	-2.70	-0.41	2.80	-0.10	0.78	-0.55	-0.71	-0.12	-0.69	0.48	-0.48	-0.83
5.66	3.90	2.34	1.96	-2.00	-0.30	2.76	-1.88	-0.04	-1.70	-1.20	-0.06	-0.64	-0.16	0.06	-0.24
5.72	4.19	2.35	1.96	-2.18	-0.32	2.55	-0.78	-1.06	-0.63	-1.06	-0.16	-0.50	-0.26	-0.79	-0.72
5.82	4.11	2.41	2.03	-2.83	-0.34	2.92	-0.89	0.58	-1.37	-1.90	-0.08	-0.76	0.03	-0.73	-1.94
5.92	4.26	2.43	2.04	-2.86	-0.46	2.69	-0.10	0.20	0.14	-1.78	-0.13	-0.71	0.26	-1.24	-1.16
5.92	4.69	2.42	2.09	-6.09	-0.68	3.21	2.55	-0.45	1.91	-4.74	-0.01	-0.99	0.47	-1.42	-2.56
6.01	4.33	2.48	2.07	-2.13	-0.26	2.71	-0.78	-0.20	-1.38	-0.93	-0.12	-0.59	-0.40	-0.22	-1.03
6.06	4.29	2.51	2.16	-1.68	-0.27	3.31	0.13	-0.41	-0.54	-1.38	0.06	-0.68	0.69	0.43	0.12
6.10	4.45	2.52	2.14	-2.41	-0.20	3.03	-0.44	-0.82	-1.19	-1.13	-0.10	-0.60	0.01	-0.56	-0.48
6.10	4.53	2.55	2.20	-1.20	-0.11	3.64	1.70	-0.67	-0.78	-1.18	-0.11	-0.71	0.90	-0.61	0.52
6.13	4.52	2.52	2.16	-3.69	-0.64	3.00	0.22	1.04	0.34	-1.24	-0.10	-0.64	0.23	-0.98	-0.79
6.25	4.73	2.56	2.27	-3.36	-0.43	3.94	0.28	-0.74	-1.63	-5.00	-0.13	-0.81	-4.04	-1.38	-3.21
6.26	4.70	2.61	2.25	-3.45	-0.38	3.49	-0.26	-0.67	-0.83	-1.22	-0.07	-0.84	0.93	-0.29	-1.78

Table B.8: Measurement of flutter derivatives $A_1^* - A_6^*$, $P_1^* - P_6^*$.